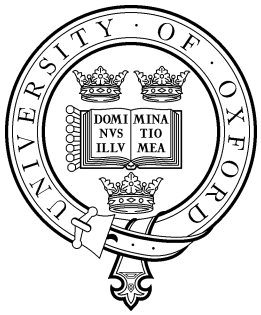
Modelling Normal Tissue Toxicity In Pancreatic Chemoradiotherapy



Alon Witztum

Brasenose College

University of Oxford

A thesis submitted for the degree of

Doctor of Philosophy

Trinity 2018

This thesis is dedicated to
my father, Amos, my mother, Daphna, and my sister, Tamar,
who is most definitely a scamp

Acknowledgements

I am grateful for receiving an MRC/Gray Institute Scholarship which funded my DPhil. For their guidance, support, and encouragement, I would like to thank my supervisors Maria Hawkins, Mike Partridge, Frank Van den Heuvel, Ben George, and Samantha Warren. Outside my official supervision team, I am indebted to Daniel Holyoake, who provided hours of support in contouring and trial data acquisition/sorting, as well as Daniel Warren and Brian Burns. I would also like to thank Tim Solberg for his part in making the transition to the next step in my career so smooth, and for his professional advice.

It is impossible to express the infinite gratitude and love I have for my family (Amos, Daphna, and Tamar) for their enduring and unwavering support, inspiration, and love throughout my life.

There are far too many friends and colleagues to thank without doubling the length of this thesis. Those who kept me sane in Oxford: Matthew Williamson (there are no words), David Hansford, Max Howell, Tom Godleman, Georgia 'Dolph' O'Connor, and Erin Young. Those from across the pond: Divij Damodhar (#divlon), Bianca Datta (#CPP), and Nicholas Schneider. And those who kept me company in the overlapping writing/working period: Vikram Bhargava, Joshua Pak, Jonathan Crawford, Vaibhav Goel, and Jessica Scholey.

Abstract

The relationship between radiation dose and toxicity in pancreatic chemoradiotherapy is not well understood. Clinically, excessive normal tissue toxicity is avoided by placing a constraint on the volume of the organ receiving a dose above a threshold. Dose-volume constraints lack spatial information which may be important in determining normal tissue response.

Spatial dose distribution information can be found in dose-surface maps (DSMs). A dose-surface map is a 2-dimensional virtual unwrapping of the surface dose of on organ. Due to the complex geometry of the duodenum, previous methods for unwrapping tubular organs for spatial toxicity modelling are insufficient. A geometrically robust method for producing dose-surface maps, specifically for the duodenum, was created in order to characterise the spatial dose distribution.

This unwrapping methodology was shown to be generalisable to simple organs such as the stomach, and extendable to more complex organs such as the bronchial tree. A graphical user interface to create dose-surface maps from organs in commercial treatment planning systems was also demonstrated.

Duodenal and stomach dose-surface maps were created for patients from two pancreatic chemoradiotherapy trials, ARCII and SCALOP, treating locally-advanced pancreatic cancer (LAPC). New spatial features were extracted from dose-surface maps and their correlation with upper-gastrointestinal toxicity quantified and compared to traditional dose-volume metrics. The predictive power of some of these new metrics were found to be superior to dose-volume metrics in the stomach, but no significant correlation was found in the duodenum.

Duodenal motion throughout treatment occurs both due to respiratory motion and peristalsis. On board imaging using cone-beam CT (CBCT) during individual treatment fractions shows that interfraction variability is non-systematic and cannot be predicted. While abdominal compression is able to restrict some interfraction motion, it is unable to control peristaltic changes. Accumulated duodenal dose-surface maps from these images were created to investigate the differences between the planned and delivered dose.

Contents

List of Figures **v**

List of Tables **xi**

List of Abbreviations **xiii**

1 Introduction **1**

1.1 Preamble 1
1.2 Pancreatic Cancer 1
1.3 Radiotherapy 4
1.4 Radiotherapy Workflow 6
1.5 Current Toxicity Models 7
1.6 Dose Volume Models for Upper GI Toxicity 10
1.7 Dose Surface Maps 11
1.8 Unwrapping Hollow Organs 14
1.9 Interfraction Variability 16
1.10 Motivation & Purpose of Thesis 19
1.11 Summary of Thesis 19
1.12 Hypotheses 20
1.13 Thesis Structure & Overview 21

2 Unwrapping 3D complex hollow organs **23**

2.1 Introduction 23
2.2 Materials and Methods 26
2.2.1 Patient Cohort 26
2.2.2 Unwrapping 27
2.2.2.1 Image Definition 27
2.2.2.2 Path Selection 28

2.2.2.3 Ray Casting . . . 30
2.2.2.4 Unwrapping . . . 33
2.2.2.5 Generalisability . . . 34
2.2.3 Robustness . . . 34
2.2.3.1 Gamma Analysis . . . 34
2.2.3.2 Slice Selection . . . 35
2.2.3.3 Human Spline Selection . . . 35
2.2.3.4 Overlap Fix . . . 35
2.3 Results . . . 36
2.3.1 Dose Surface Maps . . . 36
2.3.2 Robustness . . . 38
2.3.2.1 Slice Selection . . . 38
2.3.2.2 Spline Selection . . . 39
2.3.2.3 Overlap Fix . . . 39
2.4 Discussion . . . 40
2.4.1 Unsuccessful Attempts . . . 40
2.4.2 Dose Surface Maps . . . 41
2.4.3 Robustness . . . 43
2.5 Conclusion . . . 45

3 Further Applications of Unwrapping Methodology 46
3.1 Introduction . . . 46
3.2 Materials & Methods . . . 50
3.2.1 Stomach . . . 50
3.2.2 Bronchial Tree . . . 50
3.2.3 TPS Integration . . . 52
3.3 Results . . . 54
3.3.1 Stomach . . . 54
3.3.2 Bronchial Tree . . . 55
3.3.3 TPS Integration . . . 57
3.4 Discussion . . . 58
3.5 Conclusion . . . 62

4 Feature Extraction for Toxicity Correlation **64**
4.1 Introduction . . . 64
4.2 Materials & Methods . . . 66
4.2.1 Overview . . . 66
4.2.2 Patient Cohort . . . 66
4.2.3 Organ Unwrapping . . . 67
4.2.4 Traditional Dose Metrics . . . 68
4.2.5 Spatial Dose Metrics . . . 69
4.2.6 Population Dose-Surface Map Analysis . . . 70
4.2.7 Region-of-interest Metrics . . . 71
4.2.7.1 Permutation Test . . . 71
4.2.7.2 Extracting Region-of-interest Metrics . . . 72
4.3 Results . . . 73
4.3.1 Traditional Dose Metrics . . . 73
4.3.1.1 Stomach . . . 74
4.3.1.2 Duodenum . . . 75
4.3.2 Spatial Dose Metrics . . . 76
4.3.3 Population Dose-Surface Map Analysis . . . 77
4.3.4 Region-of-interest Metrics . . . 79
4.4 Discussion . . . 82
4.4.1 Duodenum . . . 83
4.4.2 Stomach . . . 84
4.4.3 Stomach Region-of-interest Metrics . . . 85
4.4.4 Statistical Discussion . . . 86
4.4.5 Clinical Translation . . . 86
4.4.6 Further Limitations . . . 87
4.5 Conclusion . . . 87

5 Interfraction Duodenal Changes **89**
5.1 Introduction . . . 89
5.2 Materials & Methods . . . 91
5.2.1 Patient Cohort . . . 91
5.2.2 Quantifying Interfraction Changes . . . 92
5.2.3 Dose Surface Maps for Dose Accumulation . . . 92

5.3 Results 93
5.3.1 Quantifying Interfraction Changes 93
5.3.2 Dose Surface Maps for Dose Accumulation 96
5.4 Discussion 99
5.5 Conclusion 103

6 Summary & Conclusion **105**
6.1 Summary 105
6.2 Future Directions 112
6.3 Conclusion 115

Publications & Awards **117**

Bibliography **119**

List of Figures

1.1 Cancer incidence in England in 2016 for common cancers. Incidence for women shown in yellow and for men in blue. Reproduced from source: National Cancer Registration and Analysis Service within Public Health England; Office for National Statistics [1] 2

1.2 Cancer survival in the UK for patients diagnosed between 2010-11 with common cancers. [3] 2

1.3 Anatomy showing proximity of healthy organs to the pancreas [5] . . 3

1.4 Dose deposition of a 6 MV photon beam in water. 5

1.5 An example of a pancreas radiotherapy plan using 6 beams to build dose in the target (outlined in blue). The duodenum is shown outlined in black. 5

1.6 Schematic for a patient radiotherapy workflow from planning CT through to the first week of treatment. Day 0 corresponds to the first fraction of radiotherapy delivery. 6

1.7 A dose-volume histogram (DVH) with a blue line showing the dose coverage of the PTV and the other line showing the dose coverage of an organ at risk (OAR). If an organ constraint is given as $V_{10Gy} < 35\%$, meaning no more than 35% of the OAR can receive 10 Gy, the green lines show how you would check this value on the DVH. In this example, the volume of the OAR receiving at most 10 Gy is 35% ($V_{10Gy} = 35\%$) which meets the constraint. 8

1.8 Schematic for unwrapping a rectum. (a) The ground rectum shape is a straight hollow tube. The basic elements are the central axis and the orthogonal slices. (b) The tube may be bent, but under the constraint that the length of the segments is conserved. (c) To adapt to the shape of the rectum, the individual slices can be deformed. In the figure only the diameter of the slices has been varied, but the slices can be deformed such that they completely describe the true rectum shape. Reproduced with permission. [34] 15

2.1 Left: CT axis slices through the duodenum would not represent a physically meaningful spatial dose. Right: A new axis is required for slices in the duodenum to represent a physically meaningful spatial dose. 24

2.2 Left: Using the geometric central axis leads to overlapping slices. Right: A more appropriate path used to angle slices may offer a non-overlapping solution. 25

2.3 The 'racecar' path found between a user-defined start and end point in a duodenum point cloud. 30

2.4 An example of 5 angular slices from the adjusted centre point on the 'racecar' path. The 30 rays cast from the centre to the surface are shown. The surface points are connected in red for visual representation of the resulting polygons. 31

2.5 a) The two central slices overlap. The two non-overlapping slices either side are highlighted in black and set as the fixed start and end slices. b) The 30 vertices of the fixed polygons are connected and the lines between them (in blue) are split into the number of required slices (in this case 2 slices need to be replaced). c) and d) Two views of the resulting non-flat polygons (in red) created between the two flat polygons (in black). 32

2.6 The point on each angular slice closest to the centroid of the PTV is placed on the middle of the dose map. 33

2.7 Dose surface map for 15 unwrapped duodena with different dose distributions. The x and y axis labels are for each individual DSM. In the y-direction, each map comprises of the slices through the duodenum from superior (top) to inferior (bottom). In the x-direction, each map comprises of the surface points at each slice unwrapped from the point distal to the PTV so the centre of each DSM is the point on the circumference most proximal to the PTV. 36
2.8 Dose surface map for an oesophagus unwrapped slice-by-slice (left) and using the method described in this paper (right). The y-direction comprises of the slices through the oesophagus from superior (top) to inferior (bottom). The x-direction comprises of the surface points at each slice unwrapped from the point proximal to the PTV so the centre of each DSM is the point on the circumference most distal to the PTV. 37

3.1 3D point cloud of a bronchial tree (green). Start and end points of each segment in black. Segment 1 = AB (trachea), Segment 2 = CD (right primary bronchus), Segment 3 = CE (left primary bronchus). . 50
3.2 Placement of angular slices in segments 1 and 3 prior to adjustment of start point of segment 3. 52
3.3 Placement of angular slices in segments 1 and 3 after adjustment of start point of segment 3. 53
3.4 Identification of corners of a 30 x 30 bronchial tree segment map that are sampled by the bifurcated segments below it. Dose at the yellow pixels are excluded from the dose-surface map as they are included in the dose-surface map of another segment. 54
3.5 Dose surface map for 15 unwrapped stomachs with different dose distributions. The x and y axis labels are for each individual DSM. In the y-direction, each map comprises of the slices through the stomach from superior (top) to inferior (bottom). In the x-direction, each map comprises of the surface points at each slice unwrapped from the point distal to the PTV so the centre of each DSM is the point on the circumference most proximal to the PTV. 55
3.6 Dose-surface maps for the trachea (top row) and the two main bronchi (second row). The dose is set as the absolute value of the y-coordinate and the dose colour wash (in gray) scale is the same across all maps. . 56

3.7 Top: Position of PTV (red) invading the bronchial tree (blue). Bottom: Dose distribution on the bronchial tree shown with a dose colour wash (0 - 45 gray). 57
3.8 Top row: Dose-surface map for trachea. Second row: DSMs for right and left main bronchi. Third row: DSMs for two branches that split from the right main bronchus. Dose-surface maps have dose scale (0 - 45 gray). 58
3.9 Graphical user interface for dose-surface map production. Example dose-surface map shown is a 30 x 30 duodenal DSM from a clinical trial. Dose colour wash presented in gray. 59
3.10 Panels A shows an axial image of a central tumor in the right lower lobe of the lung obtained at presentation with computed tomography, with overlaid treatment plans for stereotactic ablative radiation therapy (SABR). Target dose is as indicated in the colour key, with blue indicating 50% of the prescribed dose and red 100%. Endobronchial ultrasound-guided bronchoscopy, performed 8 months after treatment, shows a plaque-like area of mucosal necrosis in the right mainstem bronchus (Panel C). The necrotic area extended from the midright mainstem bronchus to the right bronchus intermedius and right hilum along the posterolateral aspect of the airway. The necrotic area (N) is outlined and is adjacent to normal mucosa (M) and the lumen (L) of the right mainstem bronchus. Reproduced with permission from [79], Copyright Massachusetts Medical Society. 61

4.1 Spatial features such as the length of an organ where at least Y% of the circumference receives less than X Gy can be found from the dose-surface maps. In this example figure, 33% of the length of the duodenum receives less than 45 Gy to at least 10% of the circumference of the organ. 70
4.2 Four 5 x 5 DSMs with their associated toxicities labelled in red. Circled pixel illustrates that a statistical test is applied to the same pixel in each DSM. 71

4.3 Left: True Kendall's tau-b correlation coefficient for the true dose-toxicity association. Right: The position of the true tau-b (red line) within the distribution of permuted tau-b (histogram bars) defined the p-value for a single pixel. 72
4.4 Duodenal population dose-surface maps. ARCII data is shown on the left, with corresponding SCALOP data on the right. Top row: Mean dose-surface map. Second row: Mean DSM for patients with grade $\geqslant$ 2 and grade $\geqslant$ 3 toxicity. Third row: Mean DSM for patients with grade $<$ 2 and grade $<$ 3 toxicity. Final row: Dose difference maps showing the difference in maps with and without toxicity. Dose colour wash scale in Gy. 78
4.5 Stomach population dose-surface maps. ARCII data is shown on the left, with corresponding SCALOP data on the right. Top row: Mean dose-surface map. Second row: Mean DSM for patients with grade $\geqslant$ 2 and grade $\geqslant$ 3 toxicity. Third row: Mean DSM for patients with grade $<$ 2 and grade $<$ 3 toxicity. Final row: Dose difference maps showing the difference in maps with and without toxicity. Dose colour wash scale in Gy. 79
4.6 Heat map showing p-values in the stomach dose-surface map. ARCII shown on left and SCALOP on right. 80
4.7 Map showing pixels in the stomach dose-surface map with a p-value (calculated using a permutation test) $<$ 0.2 in yellow. ARCII shown on left and SCALOP on right. 80
4.8 Area under the ROC curve for region-of-interest metric ($D_{mean,ROI}$), dose-surface metrics ($D_{mean,SA}$ and SA_{45}), and dose-volume metrics (V_{15} and V_{35}). Top left: Predicting grade $\geqslant$ 2 toxicity in ARCII patients. Top right: Predicting grade $\geqslant$ 3 toxicity in ARCII patients. Bottom left: Predicting grade $\geqslant$ 2 toxicity in SCALOP patients. Bottom right: Predicting grade $\geqslant$ 3 toxicity in SCALOP patients. . . . 81

5.1 Volume of duodenum in cm^3 on planning CT marked in solid black diamond and the range of volumes from CBCTs marked as a box for each abdominal compression (left) and non-compressed (right) patient. 94

5.2 Average (and range) of Euclidean distances between the centre-of-mass displacement between the planning CT duodenum and the CBCT duodena for each abdominal compression (left) and non-compressed (right) patient. 95
5.3 Average (and range) of Modified Hausdorff Distances between the planning CT duodenum and the CBCT duodena for each abdominal compression (left) and non-compressed (right) patient. 96
5.4 Maximum variation in volume receiving at least 25, 35, 45, and 50 Gy between the duodenum contoured on CBCTs compared to the planning CT for each abdominal compression (left) and non-compressed (right) patient. 97
5.5 For abdominal compression patients: Accumulated dose-surface map by scaling the duodenal dose from the planning CT to 5 fractions (top) and by adding 5 single fraction duodenum doses from the CBCTs (middle). Dose-difference maps for each patient calculated by subtracting the accumulated plan DSM from the accumulated CBCT DSM. Dose shown in gray. 98
5.6 For non-compressed patients: Accumulated dose-surface map by scaling the duodenal dose from the planning CT to 4 fractions (top) and by adding 5 single fraction duodenum doses from the CBCTs (middle). Dose-difference maps for each patient calculated by subtracting the accumulated plan DSM from the accumulated CBCT DSM. Dose shown in gray. 98

List of Tables

1.1 Table showing grading guidance for grade 2 and 3 for some common gastrointestinal adverse events according to version 5 of the Common Terminology Criteria for Adverse Events (CTCAE). ADL: Activities of daily living, TPN: Total parenteral nutrition. 9

2.1 Slice selection robustness. 3%/3px gamma results comparing a reference selection (every 6 points from 14-188 with no overlap) for 3 patients to shift 1 (every 6 from 10-184 with no overlap), shift 2 (every 6 from 18-192 with no overlap) and overlap (every 6 from 14-188 with overlap). 39

2.2 Robustness (gamma 3%/3px) of replacing 3 (3) or 5 (5) planes with 30 sided polygons in two straight sections of the duodenum (S1, S2) and one bend (B) for 2 datasets (Duodenum 1, Duodenum 3). 40

4.1 Summary of dose-volume and dose-surface metrics extracted for patients in both clinical trials (ARCII and SCALOP). The V_X and SA_X metrics were extracted in absolute (mm^3/mm^2) and relative (%) terms. These metrics were extracted for the stomach and duodenum. 69

4.2 Summary of stomach dose-volume and dose-surface metrics (mean and range) that are extracted from the ARCII and SCALOP datasets. . . 74

4.3 Summary of duodenum dose-volume and dose-surface metrics (mean and range) that are extracted from the ARCII and SCALOP datasets. 75

4.4 Summary of stomach dose-volume and dose-surface metrics that are significant in predicting grade $\geqslant$ 2 UGIT in ARCII patients. The mean value for each metric for patients who had grade $\geqslant$ 2 UGIT (T), and those who didn't (NT) are presented together with the p-value calculated with a Wilcoxon rank-sum test (p) and the area under the ROC curve (ROC). 76

4.5 Area under the ROC curve (AUC) of duodenal spatial metrics that are significant in predicting grade $\geqslant$ 3 UGIT in ARCII patients. This AUC represents an inverse relationship. 77
4.6 Area under the ROC curve (AUC) of stomach spatial metrics that are significant in predicting grade $\geqslant$ 2 UGIT in ARCII patients. 77
4.7 Area under the ROC curve (AUC) of stomach spatial metrics that are significant in predicting grade $\geqslant$ 3 UGIT in SCALOP patients. 77
4.8 Comparison of the best (highest AUC) stomach dose-volume and dose-surface metrics that are significant in predicting grade $\geqslant$ 2 UGIT in ARCII patients to the predictive power of new region-of-interest metrics. 81

5.1 Summary of prescription and fractionation schedule for the five abdominal compression patients chosen. 91
5.2 Volume of duodenum receiving at least 25, 35, 45, and 50 Gy according to the planning CT for both abdominal compression and non-compressed patients. Dose is in gray (EQD2). 97
5.3 The percent of the plan and accumulated DSM that receives at least 10% (SM_{10}), 30%, 50%, 70%, and 90% of the maximum dose of that DSM and the difference between each metric for the five abdominal compression patients. 99
5.4 The percent of the plan and accumulated DSM that receives at least 10% (SM_{10}), 30%, 50%, 70%, and 90% of the maximum dose of that DSM and the difference between each metric for the three non-compressed patients. 100

List of Abbreviations

$4DCT$	Four-dimensional computed tomography
AUC	Area under the ROC curve
CAS	Central axis spline
$CBCT$	Cone-beam computed tomography
CC	Craniocaudal
COM	Centre of mass
CT	Computed tomography
$CTCAE$	Common Terminology Criteria for Adverse Events
D_{max}	Maximum dose
D_{mean}	Mean dose
DSH	Dose-surface histogram
DSM	Dose-surface map
DVH	Dose-volume histogram
DWH	Dose-wall histogram
GI	Gastrointestinal
GTV	Gross tumour volume
GUI	Graphical user interface
Gy	Unit of dose - gray

$LAPC$	Locally-advanced pancreatic cancer
MHD	Modified Hausdorff distance
MR	Magnetic resonance
MRI	Magentic resonance imaging
$NSCLC$	Non-small-cell lung cancer
OAR	Organ at risk
PBT	Proximal bronchial tree
PTV	Planning target volume
$QUANTEC$	Quantitative Analyses of Normal Tissue Effects in the Clinic
ROC	Receiver operating characteristic
ROI	Region of interest
$RTOG$	Radiation therapy oncology group
SA_X	Surface area receiving more than X Gy
$SABR$	Stereotactic ablative radiotherapy - also known as SBRT (stereotactic body radiation therapy)
SM_X	Percentage of DSM pixels receiving more than X% of the maximum dose
$UGIT$	Upper gastrointestinal toxicity
V_X	Volume receiving more than X Gy

Chapter 1

Introduction

1.1 Preamble

Radiotherapy delivers dose to healthy tissue as well as the tumour and this can lead to normal tissue toxicity. To reduce toxicity, the volume of a healthy organ receiving a threshold dose is restricted. This thesis questions whether this is as important as restricting the dose to the surface of an organ such as the duodenum, which is hollow. Furthermore, this thesis investigates whether or not the way the dose is distributed on the surface of a hollow organ is useful in helping to predict toxicity.

1.2 Pancreatic Cancer

Pancreatic cancer is the eighth most common cancer (2016, Figure 1.1, [1]) in England but the fifth most common cause of cancer death (2014, [2]). While pancreatic cancer incidence has increased, survival rates have not improved. In fact, the ten-year survival rate was 1% in the 1970s, and it remains at this same low rate today (Figure 1.2).

At diagnosis, pancreatic cancer patients can be split into three groups. 20% of patients present with a resectable tumour, 30% with locally-advanced pancreatic cancer

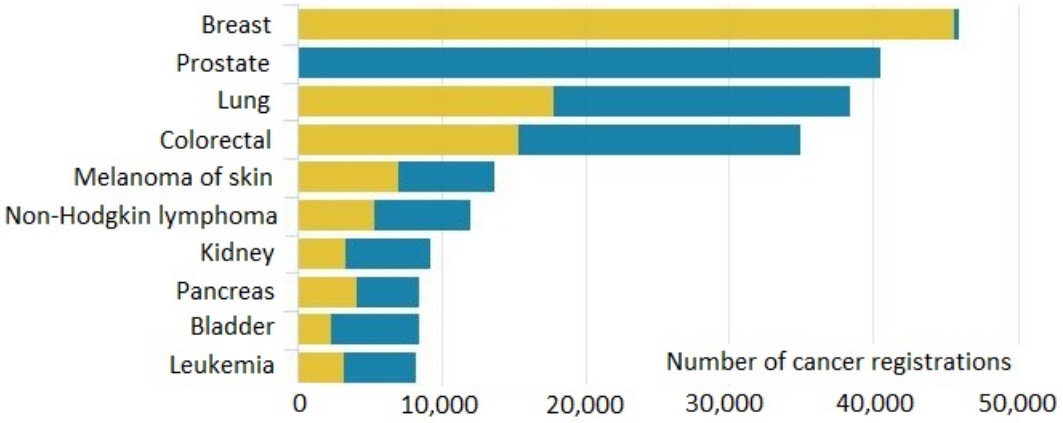


Figure 1.1: Cancer incidence in England in 2016 for common cancers. Incidence for women shown in yellow and for men in blue. Reproduced from source: National Cancer Registration and Analysis Service within Public Health England; Office for National Statistics [1]

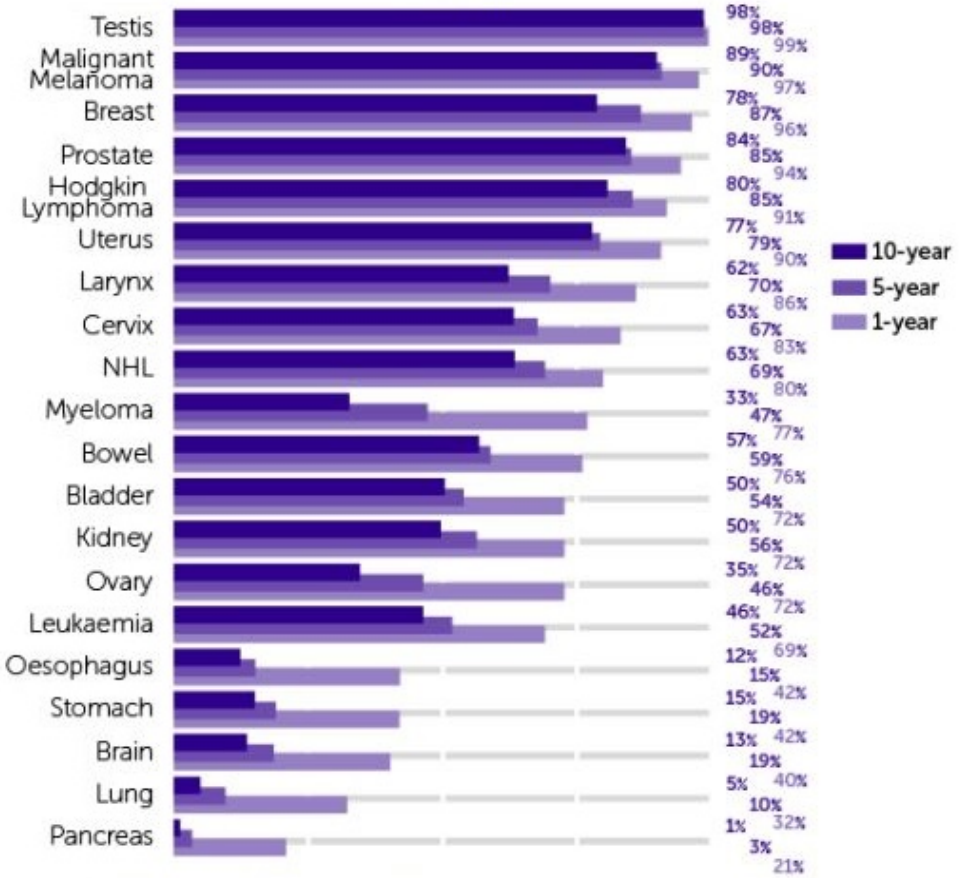


Figure 1.2: Cancer survival in the UK for patients diagnosed between 2010-11 with common cancers. [3]

(LAPC) but no distant metastases and the remaining 50% have metastatic disease [4]. Locally-advanced pancreatic cancer describes a non-metastatic tumour that cannot be surgically removed, usually due to proximity to critical healthy organs. For patients where surgery is not an option, such as those diagnosed with LAPC, definitive treatment options include chemotherapy alone or some combination of chemotherapy and radiotherapy (chemoradiotherapy).

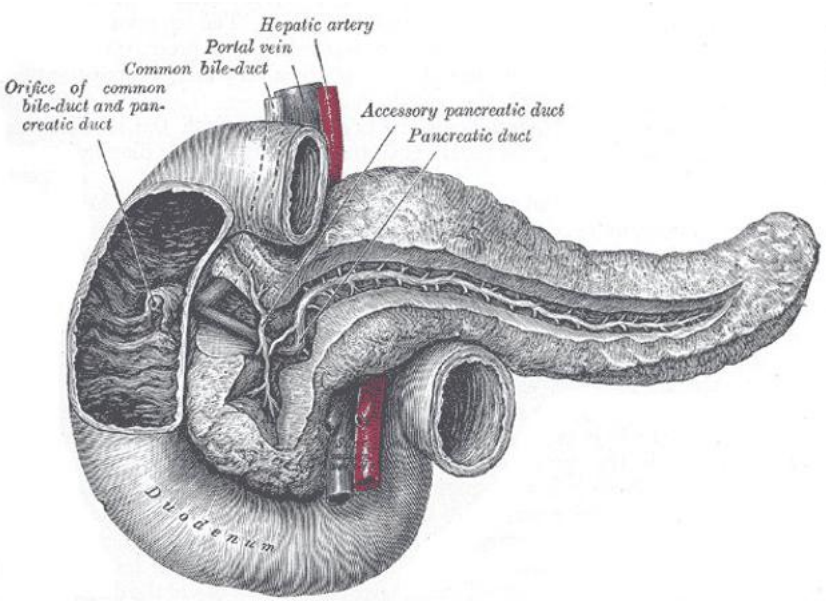


Figure 1.3: Anatomy showing proximity of healthy organs to the pancreas [5]

The proximity of healthy organs around the pancreas makes it challenging to deliver the high doses of radiotherapy required to achieve local tumour control without unacceptable levels of dose to the organs around it (Figure 1.3). Patients who present with locally-advanced pancreatic cancer (∼30%) suffer both high rates of distant metastatic failure and local progression [6], with local tumour progression reported in 25% to 62% of patients [7, 8, 9, 10]. In fact, it has been reported that between a quarter to a third of patients die from locally destructive disease [7, 11, 12, 13] which

has led to numerous studies attempting to improve local control of the tumour with dose escalation [7, 12, 14, 15, 16, 17]. While many of these studies report a successful increase in the prescription dose, these increases are ultimately limited by normal tissue toxicity.

This thesis focuses on predicting radiation-induced toxicity in patients who are treated with chemoradiotherapy for locally-advanced pancreatic cancer. Some of the acute toxicities typically observed include anorexia, abdominal pain, nausea, and vomiting. In this work these are considered together and collectively referred to as upper-gastrointestinal toxicity. These can vary in severity and a brief discussion regarding this classification can be found in Section 1.5.

1.3 Radiotherapy

In external beam photon radiotherapy, photons are directed towards the tumour in an effort to destroy cancer cells. Figure 1.4 shows the amount of dose deposited by a photon as it travels through water with energies of 6 MV (megavolts) - an energy commonly used for treatment. As illustrated by the initial gradual increase in dose over the first 1.5 cm of depth, photons deposit dose in all tissue from the skin to the tumour, and they also deposit dose on the way out of the body. In radiotherapy, the amount of radiation delivered to healthy tissue is minimised in order to reduce radiation-induced toxicity.

One way a more favourable dose distribution is achieved is by delivering photons from multiple angles. By aiming each beam from a different angle, as shown in Figure 1.5, less radiation can be delivered by each individual beam to reduce the dose

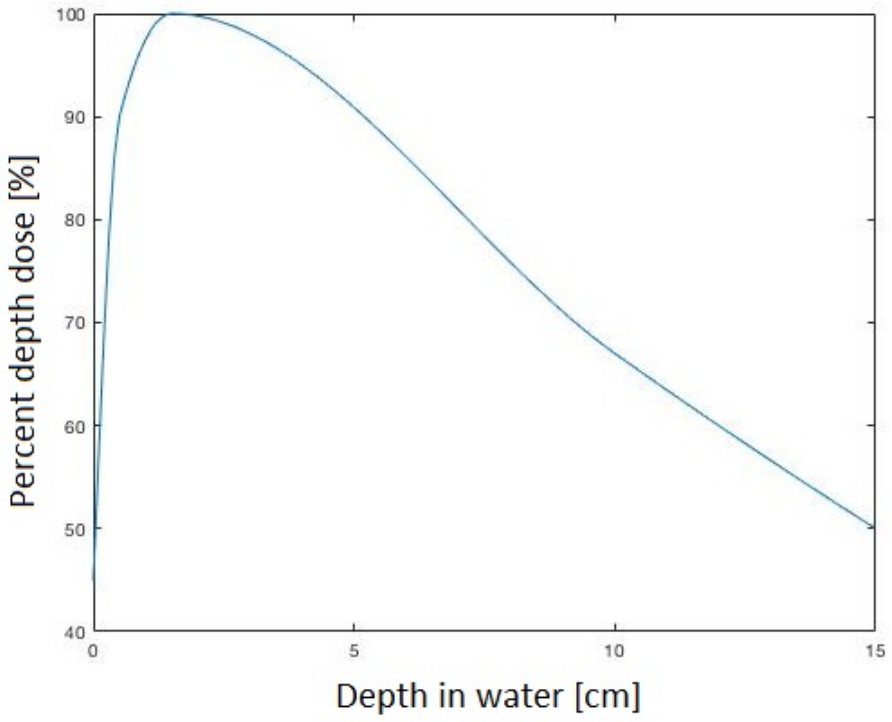


Figure 1.4: Dose deposition of a 6 MV photon beam in water.

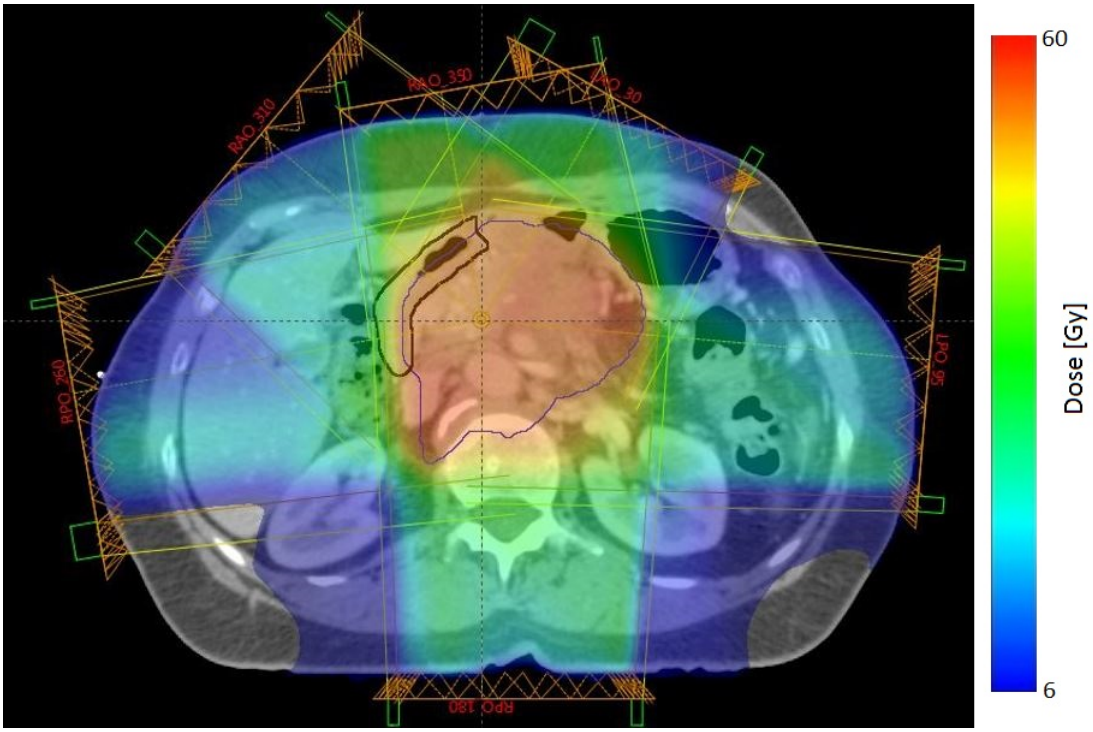


Figure 1.5: An example of a pancreas radiotherapy plan using 6 beams to build dose in the target (outlined in blue). The duodenum is shown outlined in black.

to healthy tissues while building up the dose at the tumour.

1.4 Radiotherapy Workflow

Radiotherapy treatments are designed in treatment planning systems (TPSs) which calculate the dose delivered to the patient based on the image acquired from a computed tomography (CT) scan. This CT, called the planning CT, is taken approximately a week before radiotherapy treatment starts, as illustrated in Figure 1.6. Because the treatment plan is based on this CT, the patient is imaged daily on the treatment machine using the on-board imaging in order to check for and minimise variation due to gross anatomical changes or patient positioning errors. The smaller and most common variations due to patient positioning can be addressed by realigning the patient. However, the more complex issue of anatomical changes between treatment fractions is addressed in more detail in Section 1.9.

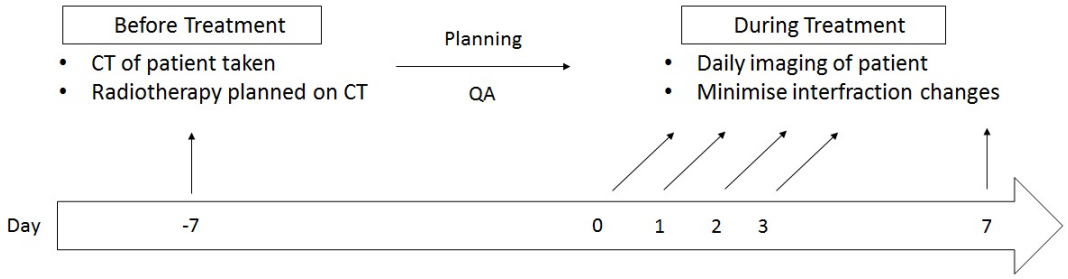


Figure 1.6: Schematic for a patient radiotherapy workflow from planning CT through to the first week of treatment. Day 0 corresponds to the first fraction of radiotherapy delivery.

A radiation oncologist delineates the gross tumour volume (GTV) and healthy organs (organs at risk) around the tumour on the CT. The GTV is then expanded to a planning target volume (PTV) which ensures complete irradiation of the diseased

area. The PTV incorporates the GTV, any subclinical microscopic malignant disease which must be treated, and any internal tumour changes (size, shape, and position) and set-up uncertainty (patient positioning and beam alignment). An organ at risk (OAR) is defined as normal tissue whose radiation sensitivity may significantly influence treatment planning or prescribed dose. In practice this refers to any healthy organ in or near the beam path. Delineation of organs is required so that the dose delivered to the volume of each structure can be calculated. Dose-volume histograms, which show what fraction of an organ receives at least a threshold dose, are displayed in the treatment planning system (Figure 1.7).

Dose-volume histograms (DVHs) are a standard tool in radiotherapy treatment planning to measure target coverage and normal tissue sparing. Dose-volume constraints on OARs limit the mean or maximum dose, or the volume of an organ receiving a threshold dose. For example, an OAR constraint can be written as $V_{10Gy} < 35\%$ which means that at most 35% of the OAR can get more than 10 Gy. An example of this is shown in Figure 1.7. These dose-volume metrics are used in the clinic to achieve a minimum standard which treatment plans should meet in order to avoid toxicity. The recommended dose limits of these organs are found by analysing clinical trials and building dose-toxicity models by correlating dose metrics with toxicity.

1.5 Current Toxicity Models

To better understand normal tissue toxicity it is important to model the relationship between the dose delivered to the organ and the resulting adverse event. This can be done by following patients through treatment, analysing their treatment plan and

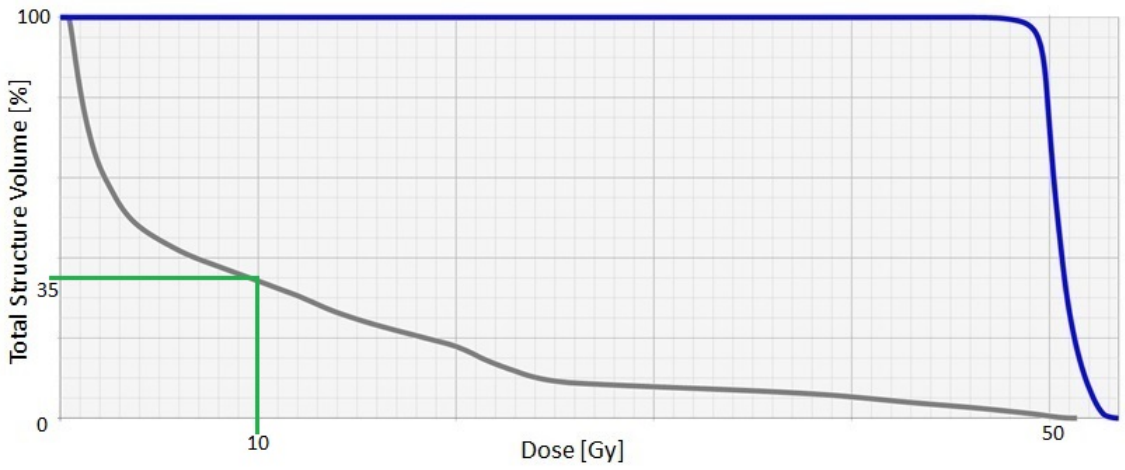


Figure 1.7: A dose-volume histogram (DVH) with a blue line showing the dose coverage of the PTV and the other line showing the dose coverage of an organ at risk (OAR). If an organ constraint is given as $V_{10Gy} < 35\%$, meaning no more than 35% of the OAR can receive 10 Gy, the green lines show how you would check this value on the DVH. In this example, the volume of the OAR receiving at most 10 Gy is 35% ($V_{10Gy} = 35\%$) which meets the constraint.

tracking any toxicity that may occur post-treatment. Since the reporting of toxicity can be subjective when, for example, assigning a quantitative number to a degree of nausea, the National Cancer Institute release a Common Terminology Criteria for Adverse Events (CTCAE) which defines toxicity (adverse events) and severity according to grade. According to the guidelines, currently on version 5, toxicity can be graded from 0 (no adverse event) to 5 (death due to adverse event). Examples of some gastrointestinal adverse event definitions for grades 2 and 3 are given in Table 1.1.

In this thesis, upper-gastrointestinal toxicity was defined as the maximal grade of any of the Radiation Therapy Oncology Group (RTOG) defined acute upper-gastrointestinal toxicities (anorexia (with or without weight loss), abdominal pain, nausea, vomiting, gastrointestinal bleeding/perforation, and bowel obstruction).

CTCAE Term	Grade 2	Grade 3
Abdominal pain	Moderate pain; limiting instrumental ADL	Severe pain; limiting self care ADL
Diarrhea	Increase of 4 - 6 stools per day over baseline; moderate increase in ostomy output compared to baseline; limiting instrumental ADL	Increase of $\geqslant$7 stools per day over baseline; hospitalisation indicated; severe increase in ostomy output compared to baseline; limiting self care ADL
Duodenal perforation	Invasive intervention not indicated	Invasive intervention indicated
Duodenal ulcer	Symptomatic; medical intervention indicated; limiting instrumental ADL	Severely altered GI function; TPN indicated; elective invasive intervention indicated; limiting self care ADL
Nausea	Oral intake decreased without significant weight loss, dehydration or malnutrition	Inadequate oral caloric or fluid intake; tube feeding, TPN, or hospitalisation indicated
Vomiting	Outpatient IV hydration; medical intervention indicated	Tube feeding, TPN, or hospitalisation indicated

Table 1.1: Table showing grading guidance for grade 2 and 3 for some common gastrointestinal adverse events according to version 5 of the Common Terminology Criteria for Adverse Events (CTCAE). ADL: Activities of daily living, TPN: Total parenteral nutrition.

The dose-response of each organ is modelled to determine what threshold dose to an organ volume will reduce toxicity by correlating different dose metrics with toxicity. For example, if the treatment plan of every pancreatic cancer patient was analysed and it was found that all patients with duodenal $V_{50Gy} > 40\%$ also ended up with duodenal ulcers, a duodenal constraint would be established so that treatments would be planned accordingly. There have been two recent attempts at publishing a compendium of clinically established normal tissue constraints. The first was by Emami et al in 1991 [18] which was largely based on clinical experience rather than

driven by dose-response models. This was followed in 2010 by a larger review called Quantitative Analyses of Normal Tissue Effects in the Clinic (QUANTEC) [19] which separated toxicity analysis by body site. While there is no specific report in QUANTEC for the duodenum (similarly to Emami et al [18]), the most relevant analysis is in the stomach and small bowel section [20].

1.6 Dose Volume Models for Upper GI Toxicity

QUANTEC [20] notes in 2010 that there have been few published studies that allowed the separation of effects on the stomach alone from effects on the stomach and small bowel (including the duodenum) combined. QUANTEC also recommends keeping the maximum dose to the whole stomach below 45 Gy ($D_{max} < 45$ Gy) and the absolute volume of the small bowel receiving more than 15 Gy to less than 120 cc ($V_{15Gy} <$ 120 cc) if the individual bowel loops are being delineated as small bowel. If the entire peritoneal space is delineated, the constraint should be $V_{45Gy} < 195$ cc. However, the study also notes that the body of literature relating dose to risk of stomach/small bowel toxicity is small compared to other body sites and anticipates that further studies should be able to expand on their recommendations.

Clinically, the duodenum is usually delineated separately from the small bowel and is thought to have separate dose limits. Since the QUANTEC publication in 2010 there have been a few studies into the individual tolerance of the duodenum, specifically in treatment for locally-advanced pancreatic cancer. Huang et at [21] found that $V_{25Gy} < 45\%$ reduces grade $\geqslant 3$ gastrointestinal (GI) toxicity; Nakamura et al [22] found that $D_{mean} < 46.1$ Gy and $D_{2cc} < 55.5$ Gy reduces grade $\geqslant 2$ GI

toxicity; Cattaneo et al [23] found that $V_{40Gy} < 16\%$ and $V_{45Gy} < 2.6\%$ reduces grade $\geqslant 2$ GI toxicity; and Kelly et al [7] found that $V_{55Gy} < 1$ cc reduces grade $\geqslant 2$ GI toxicity. Each of these studies had a different concurrent chemotherapy agent or agents.

From the literature, there does not appear to be any real consensus for a duodenal dose constraint in the clinic and this may be due to the wide variety of delivery techniques, fractionation schedules, and chemotherapy agents that make up all the individual studies.

While the methodology of building dose-response models by correlating dose to an organ volume to toxicity through a dose-volume histogram may be useful for solid organs, it may not be the best approach for hollow organs. In these cases it may be more important to consider dose to the surface of the organ, rather than the entire volume.

1.7 Dose Surface Maps

In the same way that a dose-volume histogram (DVH) quantifies the fractional volume of a specific organ that receives a threshold dose, a dose-surface histogram (DSH) is the analog for quantifying the dose to a fractional surface area of an organ. Another similar concept is the dose-wall histogram (DWH) which quantifies dose to a fractional volume of the organ wall. While a DSH considers dose to just the voxel on the surface of a 3D organ, the DWH will consider dose to at least two voxels of depth. The precise definition of DWH is defined by each group using it and is less popular than the DSH.

Dose-surface histograms and dose-wall histograms have been studied since the late

1990s for various hollow organs such as the rectum [24, 25, 26, 27], bladder [24, 28], and oesophagus [29]. However, clinically DVHs are still universally used for all organs at risk.

While DSHs capture information about dose to the surface, both DVHs and DSHs are still, crucially, missing spatial information about the dose distribution. It may be beneficial to not only record the dose at the surface, but to also keep information about how that dose is distribution on the organ surface. The QUANTEC recommendations, which relied extensively on dose-volume information, explicitly noted that a limitation of their predictive models is that DVHs are not the ideal representations of 3D doses as they discard all organ-specific spatial information and therefore assumes all regions are of equal functional importance. This information can be preserved in hollow organs by building 2D dose surface maps (DSMs).

Even while creating dose-surface histograms, Maguire et al [29] attempted to include some spatial information in the oesophagus by extracting features from the DSH at each axial level and found some of these new spatial features to be predictive of toxicity. Zhou et al [30] also incorporated spatial information by creating dose-circumference histograms for the oesophagus and rectum and similarly analysing these at each axial level. Both studies extracted a similar spatial feature which was a measure of the length of an organ over which a threshold percentage of the circumference was receiving a threshold dose.

Dose-surface maps (DSMs) allow visualisation and quantitative descriptions of the spatial distribution of the dose on an organ surface. Dose-surface maps have been created for various hollow organs including, in approximate popularity order,

the rectum [31, 32, 33, 34, 35, 36, 37], bladder [28, 38, 39, 40], anal canal [41, 37], and oesophagus [42]. It should be noted that not all of these cited studies are from individual research groups and therefore do not all represent original methods of DSM creation.

These dose-surface maps have been used to extract spatial dose-surface metrics such as lateral/longitudinal extent [33, 41, 39, 36]. Palorini et al [39] relate lateral extent to the percentage of circumference of the organ receiving more than a specified dose threshold at specified distances from the base of the organ, which is a similar measure to what Zhou et al [30] and Maguire et al [29] extracted from dose-circumference and dose-surface histograms respectively. Another use of these DSMs has been by Buettner et al [32] as inputs for classification methods based on neural networks. A few groups, in some of the more recent studies, have analysed dose-surface maps using a pixel-based approach which identified regions that were more predictive of toxicity [39, 37, 40].

Most of these studies conclude that spatial dose features are useful in predicting normal tissue toxicity in the rectum [31, 32, 37], bladder [39, 40], and anal canal [41, 37]. However, Buettner et al [33] found that for the rectum some toxicity endpoints are better predicted by spatial metrics, and some by dose-surface histograms. Dankers et al [42] also concluded that dose-surface maps did not improve their predictive models for acute oesophageal toxicity.

This thesis will extract similar spatial features to those discussed in this section, but first a dose-surface map needs to be created.

1.8 Unwrapping Hollow Organs

In order to build a 2D dose-surface map from a 3D tubular organ it is necessary to virtually 'unwrap' the 3D structure. This has been demonstrated successfully on hollow organs such as the rectum, bladder, anal canal, and oesophagus.

Munbodh et al [31] unwrap the rectum using a conformal mapping procedure [43] originally used for virtual colonography. Hoogeman et al [34] find the central axis of the rectum using an approximate minimum distance field approach and then create orthogonal cross sections to unwrap (Figure 1.8). The simplest method, and the one implemented by Buettner et al for the rectum [32, 33] and anal canal [41] takes each axial CT slice individually from the most superior to most inferior plane and the circumference point with associated dose is unwrapped. This method was also preferred for the rectum by Scaife et al [35] and Shelley et al [36], and for the oesophagus by Dankers et al [42]. Another popular and similar technique is used for the bladder by Palorini et al [38, 39] and Yahya et al [40] which involves anteriorly cutting the bladder at the points intersecting the sagittal plane passing through the centre of mass of the bladder. This method is employed in the commercial software, VODCA (Visualisation and Organisation of Data for Cancer Analysis, MSS Medical Software Solutions, Hagendorn, Switzerland), which is able to produce dose-surface map for hollow organs of certain geometries.

The techniques described above for the unwrapping of organs such as the rectum, bladder, anal canal, and oesophagus are not generalisable to the duodenum due to its more complex and tortuous geometry. In this thesis, 'simple' geometry will be

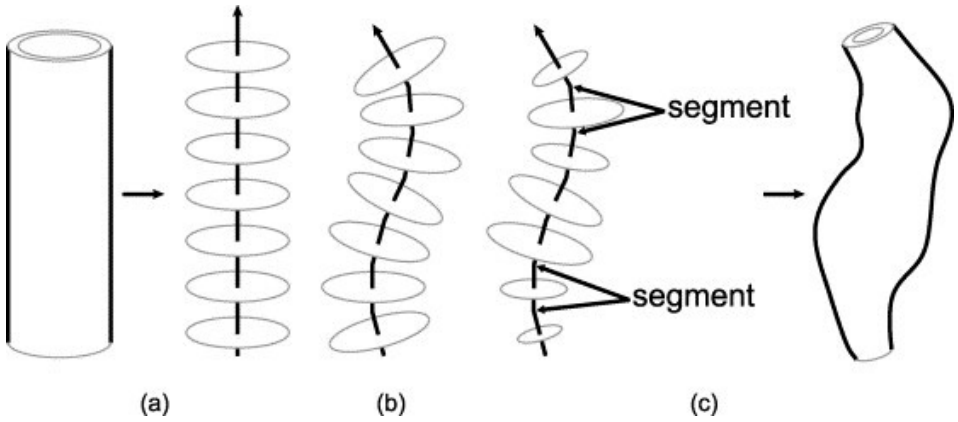


Figure 1.8: Schematic for unwrapping a rectum. (a) The ground rectum shape is a straight hollow tube. The basic elements are the central axis and the orthogonal slices. (b) The tube may be bent, but under the constraint that the length of the segments is conserved. (c) To adapt to the shape of the rectum, the individual slices can be deformed. In the figure only the diameter of the slices has been varied, but the slices can be deformed such that they completely describe the true rectum shape. Reproduced with permission. [34]

used to mean where it is possible to move through the organ from the most superior slice to the most inferior slice without reversing direction. The differences between 'simple' and 'complex' geometries will be discussed in more detail in Chapter 2 and the methodology described by Hoogeman et al [34], illustrated in Figure 1.8, will be used as a conceptual starting point for the unwrapping of complex hollow organs.

Since dose-surface maps appear to provide useful spatial information for toxicity modelling for the few hollow organs that have been unwrapped, it may be important to investigate other hollow organs, such as the poorly modelled duodenum. In an effort to preserve the spatial distribution of the dose in an organ with the complex geometry of the duodenum, a method needs to be developed to meaningfully unwrap the 3D surface dose to a 2D dose surface map. The addition of spatial dose information may help to better model the dose-response relationship of the duodenum and play a crucial role in future escalation studies and lead to improved local control in locally-

advanced pancreatic cancer radiotherapy treatments.

1.9 Interfraction Variability

When building dose-toxicity models it is important to model the delivered dose to the organ. But since radiotherapy treatment plans are based on the anatomy as seen on the day of the planning CT (Section 1.4) and there are constant anatomical changes occurring in the body, the plan created using the planning CT is not always an accurate representation of the plan delivered to the patient. There have been numerous protocols, studies and technologies developed which attempt to minimise the differences between planned dose and delivered dose. Accumulated dose (delivered dose) to organs at risk, usually found by registering daily on board images to the planning CT and calculating the daily dose to the organs, are often studied to quantify the dosimetric effect of interfraction variability. In the clinic, changes due to daily patient positioning on the treatment table are minimised by imaging the patient while on the table and aligning them to their position on the day of the planning CT as a standard of care. Unfortunately, in some parts of the body, internal anatomical changes are a lot harder to minimise.

Abdominal radiotherapy is one of the more complicated sites to treat due to anatomic positional changes in the tumour and organs at risk. These changes occur for a variety of reasons including weight loss, tumour growth/shrinkage, time since last meal, respiration, peristalsis and distension. Changes due to weight loss are often noticed during routine patient positioning and in some cases will lead to re-planning a treatment based on a new CT. Internal changes can be broadly separated into

interfraction and intrafraction differences. Interfraction changes include changes in weight, tumour changes, digestive organ filling, and patient positioning. Intrafraction changes, which naturally also cause interfraction changes, are usually due to respiration, peristalsis, and distension. To account for some of these changes influenced by digestion, patients undergoing abdominal radiotherapy are usually advised to follow a specific eating schedule prior to their radiotherapy appointments. To reduce motion due to respiration an abdominal compression technique can be employed, which uses a physical device to press down on the abdomen. The effect of this technique on duodenal surface dose will be investigated in this thesis.

Pancreatic and pancreatic tumour motion have been investigated extensively over the years. It has generally been shown that this motion occurs maximally in the craniocaudal (CC) direction (from patient head to patient toe) by using ultrasound [44, 45], MRI [46, 47], and 4DCT [48, 49, 50]

While there have been many studies into pancreatic motion and tumour motion, there have been very few investigations of changes in the duodenum. The duodenum is fixed to the pancreas and the gall bladder via the pancreatic and common bile ducts respectively. Additionally, near the level of the pancreas, the duodenum is fixed by the ligament of Treitz, a suspensory muscle arising from the stems of celiac and superior mesenteric arteries and inserting into the third and fourth portions of the duodenum [51]. These attachments mean that the motion experienced in the duodenum is different to the rest of the digestive tract.

Hallman et al [50] describes the motion of a number of organs including the duodenum which is found to have a CC centre of mass motion of approximately 8 mm,

agreeing with the 9 mm value reported by Jung et al [52].Hashimoto et al [53] tracked a marker in the duodenum of three patients and found the range of motion of the duodenum to be 22.2 mm in the CC direction. The authors note, however, the limited number of patients and that one marker cannot adequately describe the motion of a geometrically complex organ such as the duodenum. Basu et al [54] go a step further by evaluating the motion of the first (D1), second (D2), and third and fourth (D3) parts of the duodenum individually. They found that while the duodenum as a whole moved maximally in the CC direction, the relatively fixed D1 (closest to stomach) moved maximally in the anteroposterior direction, while the more mobile D2 and D3 moved maximally in the CC direction. Singh et al [51] confirm the uniqueness of duodenal motion by showing that the dosimetric effect of motion on the duodenum is different to the effect on the rest of the small bowel. Mittauer et al [55] used a new MR-Linac system (where the MRI image and radiation delivery occurs on one machine) to show that the shape of the duodenum changes daily and suggest that adapting plans based on the daily images could yield improved dosimetric results. This is in keeping with Liu et al [56] who found that adapting plans based on daily anatomy (using daily CT) resulted in dosimetrically superior plans being delivered.

Dose-surface maps provide more (spatial) information than dose-volume metrics currently being used for adaptive therapy. For new technologies such as the MR-Linac that have on-board high quality imaging, the potential use of daily spatial dose distribution information for adaptive planning is highly valuable.

1.10 Motivation & Purpose of Thesis

Clinical decisions regarding radiotherapy treatment planning are made using dose-volume metrics. This places equal importance on the dose received at every voxel within a structure. It also reduces the 3D dose distribution to a single value. For hollow organs, such as the duodenum and stomach, dose to the surface may be of more importance than dose to the inside of the hollow tube. Additionally, the spatial distribution of the dose on the surface may play an important role in tissue repair and toxicity outcomes. Current toxicity prediction models built for the duodenum and stomach using dose-volume information are poor. The purpose of this thesis is to add spatial surface dose distribution information to toxicity prediction models. This thesis aims to develop a method to extract this information and find features that correlate to treatment toxicity.

Organ changes during treatment are also important when making recommendations based on information from a planning CT. Dose information from the planning CT alone may not accurately represent the final delivered dose to the duodenum and this must be considered when building toxicity models. This thesis also aims to create daily and accumulated duodenal dose-surface maps which may be used to escalate dose using adaptive radiotherapy.

1.11 Summary of Thesis

This thesis sets forth a methodology to unwrap geometrically-complex 3D hollow organs that overcomes the barriers that prevent current unwrapping techniques from

being applied. This allows for the visualisation of the spatial surface dose distribution of the duodenum in the form of 2D dose-surface maps (DSMs). This methodology is generalisable to other organs and this is demonstrated by unwrapping a neighbouring organ to the duodenum: the stomach. These duodenal and stomach DSMs which, to our knowledge, have not been produced before are analysed to extract spatial features which are tested for correlation with toxicity data from two clinical trials, ARCII [57] and SCALOP [58]. The predictive power of the spatial features are also compared to clinically-used dose-volume metrics.

As a proof of principle, the unwrapping methodology is extended to the bronchial tree and a protocol to overcome the bifurcation in the organ is presented. A graphical user interface (GUI) is also shown and can be used to make dose-surface maps more readily available. This will increase the amount of DSM data available to researchers which will improve spatial dose-response models and make it feasible to analyse DSMs in a clinical setting.

Dose-response models developed for abdominal tumours must consider the effect of interfraction motion. The interfraction changes in the duodenum are quantified for patients treated with and without abdominal compression. For both groups of patients, accumulated dose-surface maps are created from CBCT images and compared to the planning dose-surface maps.

1.12 Hypotheses

The overarching question this thesis sets out to answer is whether the predictive power of previously inaccessible spatial dose distribution information is greater than that of

current dose-volume metrics in predicting upper gastrointestinal toxicity (UGIT) in pancreatic chemoradiotherapy.

The following hypotheses were tested during the investigation of this question:

1. The duodenum can be 'unwrapped' in a robust and spatially meaningful way.
2. The unwrapping methodology is generalisable and extendable with minimal changes to other hollow organs.
3. Spatial features that can be extracted from dose-surface maps are better predictors of upper gastrointestinal toxicity than existing dose-volume metrics.
4. Abdominal compression reduces the magnitude of physical and dosimetric changes in the duodenum.

1.13 Thesis Structure & Overview

In Chapter 2 the first hypothesis, that the duodenum can be unwrapped, is confirmed. This chapter provides the foundation methodology for work in the rest of the thesis by defining the method for dose-surface map creation. This chapter focuses on creating DSMs for the duodenum.

Chapter 3 shows that the methodology is generalisable to organs with simple geometries by successfully unwrapping the stomach, and that the methodology is extendable to other complex organs by presenting a framework for unwrapping the bifurcating bronchial tree. With these results, this chapter confirms the second hypothesis. This chapter also presents a graphical user interface which applies the unwrapping methodology described in Chapter 2.

The third hypothesis, that spatial features are better predictors of UGIT than existing metrics, is investigated in Chapter 4. This chapter extracts various spatial metrics from both stomach and duodenal dose-surface maps and correlates them to UGIT. Dose-volume and dose-surface metrics are also extracted and correlated, and their predictive power compared.

By using various metrics to show that interfraction duodenal changes are reduced with the use of abdominal compression, Chapter 5 confirms the fourth hypothesis. These metrics quantify changes in shape, position, and dosimetry. In testing this hypothesis, this chapter also presents accumulated dose-surface maps for the duodenum.

A final chapter (Chapter 6) summarises key results from Chapters 2 - 5, discusses ideas about further avenues of research for this work, and ends with some concluding remarks about the thesis.

Chapter 2

Unwrapping 3D complex hollow organs

Existing methods that produce dose-surface maps for some hollow organs are not sufficient for the duodenum. In this chapter a novel methodology to create dose-surface maps for the duodenum is presented. Work in all future chapters utilises either this methodology on other organs, or analyses the information contained in the dose-surface maps produced.

2.1 Introduction

Due to the proximity of the duodenum to the pancreas, dose to the duodenum is often considered the dose limiting factor in pancreatic chemoradiotherapy [59, 14, 60, 61, 8, 62]. Efforts made to understand the correlation between dose to the duodenum and toxicity have all been volume based [23, 7, 21, 22, 6]. Because the duodenum is hollow, it may benefit from undergoing similar surface and spatial based analyses as seen in organs such as the bladder and rectum which is described in Section 1.7.

In order to extract spatial surface dose information, the 3D dose distribution calculated in a treatment planning system is reduced to a 2D dose-surface map. This

is done by virtually 'unwrapping' the surface of the organ. Section 1.8 describes various approaches used to unwrap organs such as the oesophagus, bladder, anal canal, and rectum. However, these methods cannot be applied to the duodenum due to the tortuous geometry of the organ.

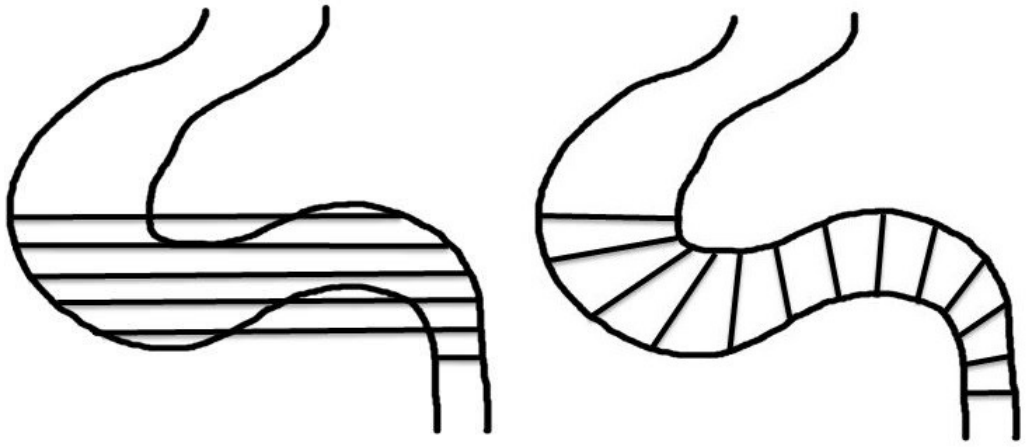


Figure 2.1: Left: CT axis slices through the duodenum would not represent a physically meaningful spatial dose. Right: A new axis is required for slices in the duodenum to represent a physically meaningful spatial dose.

The consequence of the duodenum having a 'complex' geometry, as introduced in Section 1.8, is that methods applied to unwrap 'simple' organs (oesophagus, rectum, etc) do not work. For example, we cannot move through the duodenum using a slice-by-slice approach as illustrated in Figure 2.1 because a single transaxial slice can contain segments from two different parts of the duodenum. This would lead to a physically meaningless spatial description of the surface dose. Another unwrapping method for 'simple' organs uses a geometric central axis with slices orientated normal to the axis. Once again, at high curvature this method will fail because slices may overlap (Figure 2.2). This figure also shows that a way to get a physically meaningful

dose distribution in an organ with high curvature would be to use an alternative axis which better orientates the slices. The definition of such an axis is investigated as a solution in this chapter.

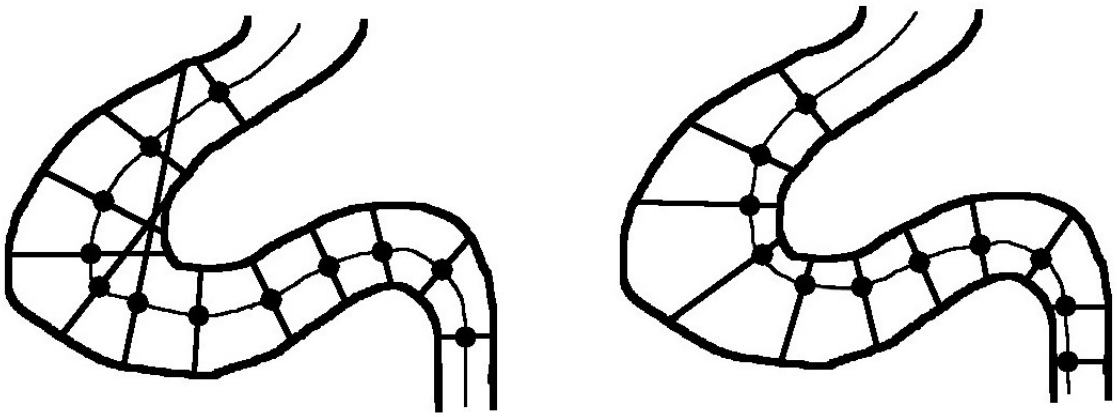


Figure 2.2: Left: Using the geometric central axis leads to overlapping slices. Right: A more appropriate path used to angle slices may offer a non-overlapping solution.

While the problem of sampling a surface with high curvature and the resulting overlapping slices is new in the field of dose surface map creation, it has been studied for virtual colonography. Virtual colonography aims to visualise the surface of the colon and provides the ability to virtually navigate the colon in order to help with polyp detection. The methodologies developed with these goals of capturing high resolution surface details may not best suit the requirements of creating dose-surface maps. One method developed for virtual colonography was to cast non-linear rays from the centre line [63, 64]. The methods used to curve the rays, such as using electric fields in Wang et al. [64], give a high resolution of the surface but are computationally expensive and such surface detail is not required when the dose to a single surface point is desired.

In this chapter, we hypothesise that the addition of spatial dose information to dose-volume toxicity models will improve the understanding of the relationship between physical dose and duodenal toxicity. Therefore, a new method is presented to conveniently and meaningfully unwrap the 3D surface dose to a 2D dose surface map in an effort to preserve the spatial distribution of the dose. This method is also generalisable to other hollow organs.

2.2 Materials and Methods

2.2.1 Patient Cohort

Eighty one patients from two clinical trials treating locally-advanced pancreatic cancer with chemoradiotherapy, ARCII [57] (n=19; EudraCT: 2008-006302-42) and SCALOP [58] (n=62; EudraCT: 2008-001394-15), were considered in this chapter.

Patients in the ARCII study received concurrent chemoradiotherapy with gemcitabine, cisplatin, and nelfinavir (a hypoxia modifier). Radiotherapy was delivered in two parts. First, 50.4 Gy in 28 fractions was prescribed to the primary tumour and elective lymph nodes, followed by an additional 9 Gy in 5 fractions as a sequential boost to the primary tumour [57].

Patients in the SCALOP study received 12 weeks of induction chemotherapy (gemcitabine and capecitabine) and those with stable or responding disease were randomised to receive either gemictabine or capecitabine concurrently with 50.4 Gy in 28 fractions [58].

In both trials, the duodenum was contoured retrospectively according the Radiation Therapy Oncology Group (RTOG) atlas and guidance [65].

2.2.2 Unwrapping

The methodology to meaningfully unwrap the duodenum requires the definition of a new axis, a set of non-overlapping slices which sample the organ, determination of the dose at the perimeter of these slices, and the ability to extract spatial information from the dose surface maps in terms of absolute area (cm^2).

Figure 2.1 illustrates the failings of using a geometric central axis which leads to overlapping slices. Overlapping slices, which are often found in areas of high curvature, should be avoided as their unwrapping result in a spatially meaningless dose distribution. Also shown in Figure 2.1 is how the use of a new axis, which considers the curvature of the duodenum, can greatly reduce the problem of overlapping planes.

The method described in this section defines this new axis, and in order to completely remove any overlap, a further automated step to create non-overlapping slices is described.

The complete methodology can be summarily split into 4 sections, as follows.

2.2.2.1 Image Definition

The contours of the duodenum and associated dose distribution were imported into MATLAB (The MathWorks, Inc., Natick, MA) using the Computational Environment for Radiotherapy Research (CERR) [66]. The organ surface is defined by a set of points in 3D space. The shape formed by these points can be described by an alpha shape. An alpha shape is a mathematically described concept by Edelsbrunner & Mücke [67], but it will suffice to use the authors' original analogy. Imagining 3D space to be made of ice cream and each point on the organ surface to be immovable

chocolate chips, the ice cream can be removed with a spherical scoop as long as it does not hit a chocolate chip (even carving out holes on the inside). Naturally, if the radius of the scoop is infinitely small, all the ice cream will be removed and there will be no 'shape', just the original point set. If the radius of the scoop is infinitely large, the holes on the inside will not be carved, and the alpha shape will be the convex hull. The radius of the alpha shape in this thesis was set to the size of the largest grid separation in the CT so that it would appropriately define the organ.

2.2.2.2 Path Selection

In order to ensure the slices through the duodenum are appropriately orientated, the definition of a path through the organ is an important step. Intuitively, in order to avoid overlapping slices in areas of high curvature the path should move closer to the inside edge of the bend. This was shown in Figure 2.2. The human brain can identify the general shape of an ideal path through the organ with relative ease, but a solution that relies too heavily on human intervention is more susceptible to inter- and intra-user variation and also less likely to be incorporated for clinical use due to the large demand on the user.

The path selection problem was first solved by incorporating a minimal amount of human intervention into the path definition. In this approach a user would select control points at multiple locations through the organ which would help define the path. However, further work on optimising this process resulted in a new approach which eliminated the need for control points and only required the user selection of a start and end point in the duodenum. Both approaches are described below.

2.2.2.2.1 Human Intervention The alpha shape of the organ is used as a mask to define a voxelised binary image with a grid of 0.085 cm $\times$ 0.085 cm $\times$ 0.085 cm. This is created by setting each voxel to 1 or 0 depending on whether it is inside or outside the mask. The binary image is then eroded by finding the regional maxima of the Euclidean distance transform of the complement of the image using a 6-connected neighbourhood. The erosion process results in a series of points that are approximately in the centre of the organ.

A selection of the points created by the image erosion process are manually chosen by the user and a spline is fit to these control points using Hobby's algorithm [68]. The human selection of control points is to ensure the spline moves close to the edges of high curvature to avoid overlapping slices.

The spline is discretised to 200 equally spaced points which defines the central axis spline (CAS). It is important to note that this central axis spline is not the geometric centre line.

2.2.2.2.2 Racecar Path The amount of human intervention in the creation of the central axis spline, as described above, was reduced to improve the chances of this method being clinically implementable. The desired path which moves close to the edges of high curvature is similar to the path favoured by a racecar through a track but in three dimensions.

In this automated approach, a user selects a start and end point in the organ and a path between these points is found algorithmically considering both length and curvature based on the method described in [69], which demonstrates the possibility of

incorporating higher-order regularisation such as curvature to shortest path problems. There are many ways to get from the start to the end point and each of these paths has a length and curvature. This automated approach minimises the function that contains both length, curvature, and a scalar weighting factor for each. Through initial testing of various duodenal geometries, a length weighting of 1 and a curvature weighting of 10 were selected to produce the desired racecar path.

As in the previous approach with human intervention, a spline is fit to the points on this racecar path using Hobby's algorithm [68], discretised to 30 points, and this defines the new central axis spline (CAS). An example CAS for a duodenum from a clinical plan is seen in Figure 2.3.

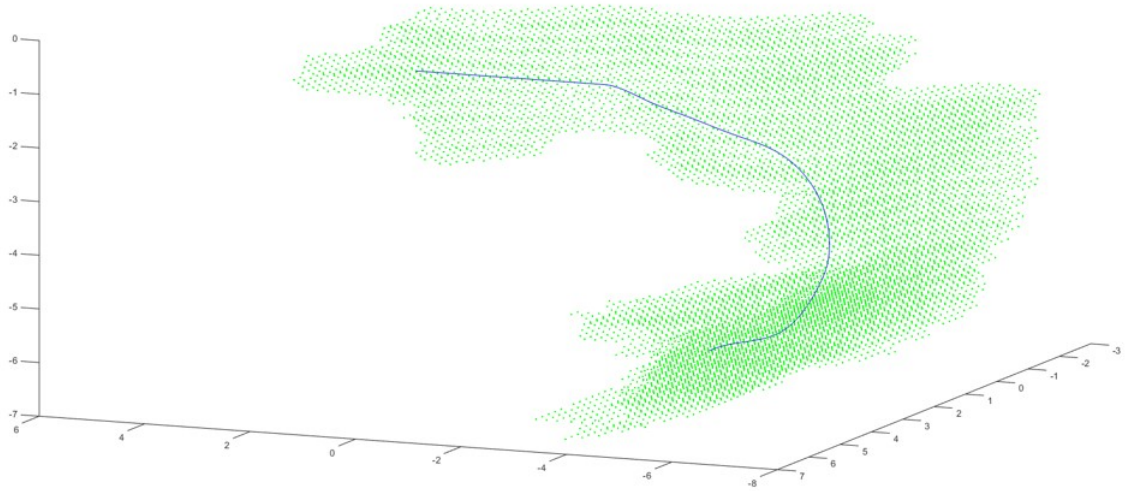


Figure 2.3: The 'racecar' path found between a user-defined start and end point in a duodenum point cloud.

2.2.2.3 Ray Casting

Orthogonal slices are created at each CAS point with a normal defined as the vector between the previous and the next CAS point. The surface dose at the perimeter of

each plane is found using a two step process.

First, 8 rays (45° apart) are cast radially outward on these orthogonal slices from the CAS point towards the surface. The centroid of these surface points approximates the centre of the organ in each plane and are set as the new centres. This is done in order to more uniformly sample the surface points in the second step.

Next, moving radially outwards from the new centre on each plane, 30 rays (12° apart) are cast towards the surface. Once the ray reaches the surface, the dose at that point is recorded. The final position and associated dose of the 30 rays together make up an angular slice for each CAS point. An example is shown in Figure 2.4 with 5 CAS points used to create angular slices.

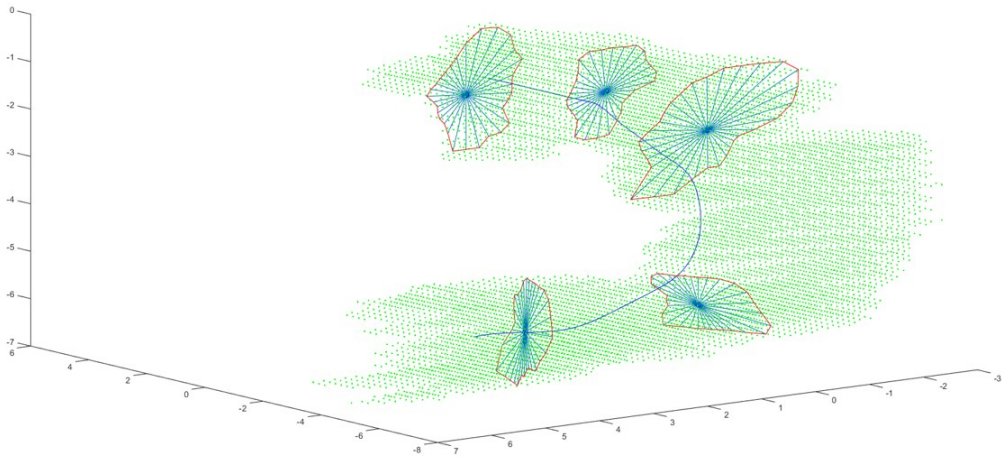


Figure 2.4: An example of 5 angular slices from the adjusted centre point on the 'racecar' path. The 30 rays cast from the centre to the surface are shown. The surface points are connected in red for visual representation of the resulting polygons.

If there are overlapping slices, the two slices (*start* and *end*) either side of the overlapping planes are defined (highlighted in black in Figure 2.5a), as is the number of slices that overlap in between them (n=2 in Figure 2.5). Each slice is a 30 edged

polygon (triacontagon) on a plane and the vertices of the two polygons (*start* and *end*) are connected (shown in Figure 2.5b). These connecting lines are split into the number of slices required between the start and end slices (n=2 in Figure 2.5) and the resulting triacontagons represent the non-overlapping polygons (shown in red in Figure 2.5c and 2.5d) which replace the overlapping slices from the original selection. These non-overlapping polygons may not lie on a single plane like the other polygons but they do meaningfully represent the surface between the two fixed slices.

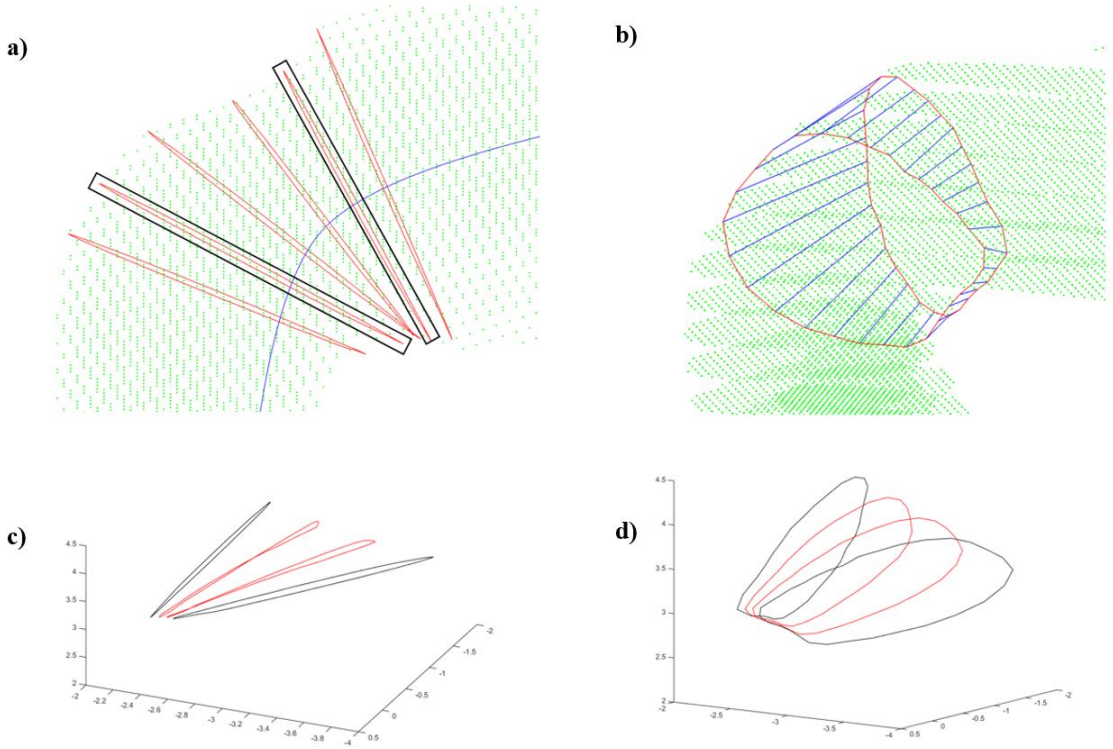


Figure 2.5: a) The two central slices overlap. The two non-overlapping slices either side are highlighted in black and set as the fixed start and end slices. b) The 30 vertices of the fixed polygons are connected and the lines between them (in blue) are split into the number of required slices (in this case 2 slices need to be replaced). c) and d) Two views of the resulting non-flat polygons (in red) created between the two flat polygons (in black).

2.2.2.4 Unwrapping

In the case of the duodenum, an unwrapping marker is defined as the centroid of the planning target volume (PTV). The perimeter point on each angular slice that is closest to the centroid is placed in the middle of the dose-surface map, ensuring the 'cutting' of the duodenum takes place on the side distal to the pancreas and the tumour (Figure 2.6). This is done in an attempt to place regions of higher dose in the centre of the map.

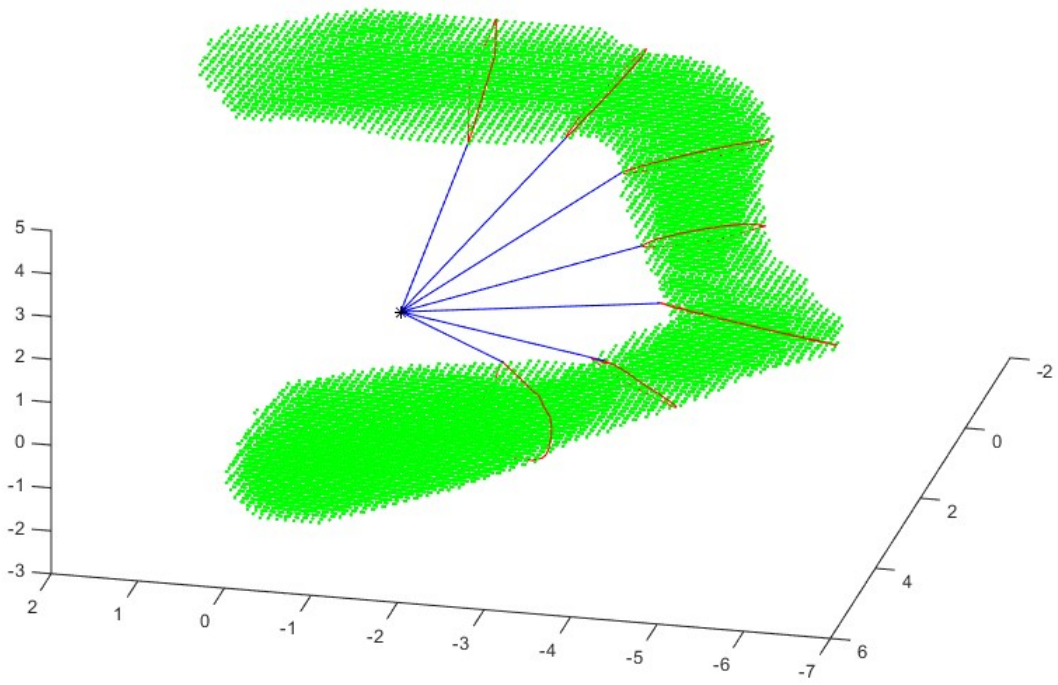


Figure 2.6: The point on each angular slice closest to the centroid of the PTV is placed on the middle of the dose map.

Since the angular slices sample the inner and outer edges differently, each pixel on the dose map is a different size. To preserve the ability to extract information in

absolute terms, a lookup grid is also saved defining the size of each pixel on the 2D DSM. The size of the pixel is calculated as the sum of half the distance to each point either side of the pixel in both the x and y direction.

2.2.2.5 Generalisability

An oesophagus from a lung cancer treatment was also unwrapped using the same methodology. The resulting dose-surface map was compared to one produced using a slice-by-slice approach as described for simple organs in the literature.

2.2.3 Robustness

2.2.3.1 Gamma Analysis

Gamma analysis [70] was selected as the quantitative metric used when comparing dose-surface maps. Dose-difference maps can identify regions where two dose-surface maps disagree. However, in areas of high dose gradient a small spatial error or shift results in a large dose-difference. For example if a dose-surface map is shifted by a pixel or two in the map x-direction with circular boundary conditions, even though the unwrapping was similar and the features that will be extracted from the map will be the same, the dose-difference map may be unimportant. The distance-to-agreement criteria, which is incorporated along with a dose tolerance into the gamma index, recognises that a small spatial error should be allowed when comparing dose maps. For this reason, when comparing dose-surface maps in this chapter, a gamma index is used with a 3%/3 pixel threshold. This means that for each pixel in a DSM, if there is a pixel in the comparison map within a 3 pixel radius that has a dose within 3% of the reference map pixel, that pixel will have a passing gamma index. The total

number of passing pixels is then expressed as a percentage of total pixels (900).

2.2.3.2 Slice Selection

Only 30 slices are used to describe the final DSM from the discretised central axis spline points. The CAS formed from the user-defined control points is discretised to 200 points and the process for selecting these 30 slices, including whether or not this process results in slice overlap, was studied and the effect on the resultant dose surface map quantified.

2.2.3.3 Human Spline Selection

When the central axis spline is created from control points that required human intervention, a different central axis spline may be created for the same dataset if a different user selects the control points, or if the same user selects control points on different days. Four DSMs were compared from splines created on four separate days on the same dataset by the same user. Additionally, two further users picked splines for the same dataset and the inter-user robustness was checked.

2.2.3.4 Overlap Fix

This method has a built in step which removes any overlapping slices that remain after selecting a central axis spline (Figure 2.5). Each slice is a planar (flat) 30 sided polygon and this method replaces overlapping slices with 30 sided non-planar polygons which uniformly sample the space previously sampled by these overlapping slices. The effect on the dose-surface map of using 30 sided non-planar polygons instead of planar polygons was studied.

2.3 Results

2.3.1 Dose Surface Maps

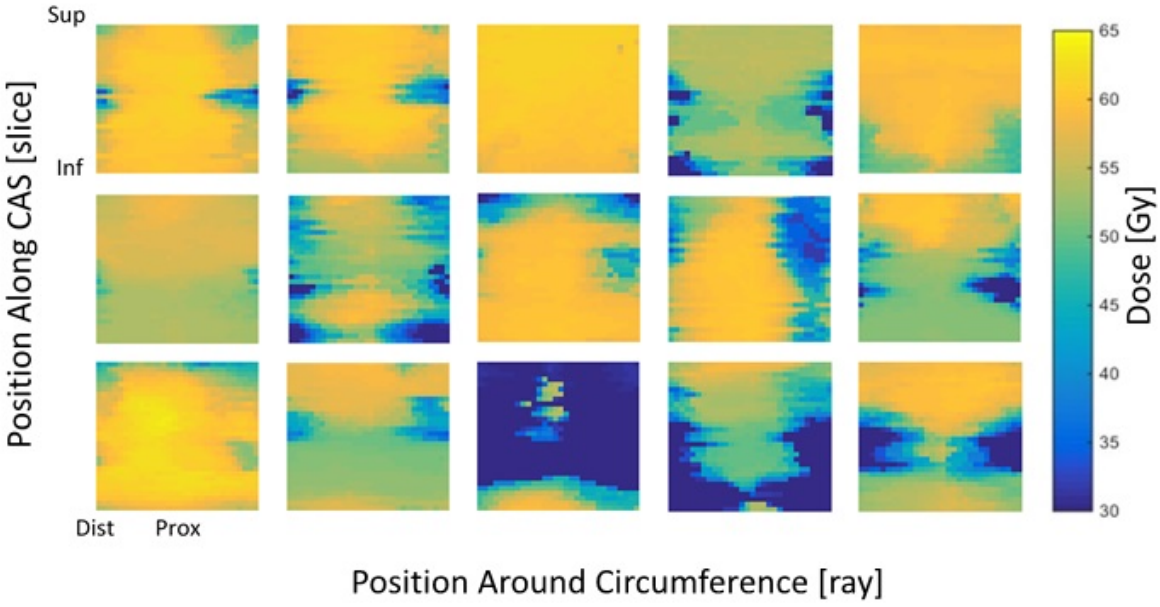


Figure 2.7: Dose surface map for 15 unwrapped duodena with different dose distributions. The x and y axis labels are for each individual DSM. In the y-direction, each map comprises of the slices through the duodenum from superior (top) to inferior (bottom). In the x-direction, each map comprises of the surface points at each slice unwrapped from the point distal to the PTV so the centre of each DSM is the point on the circumference most proximal to the PTV.

The method described in this chapter was successfully implemented to unwrap 81 duodena from the ARCII [57] and SCALOP [58] clinical trials. Further details regarding these datasets can be found in Section 2.2.1. Figure 2.7 shows 15 of these duodena from the ARCII dataset. Each panel in Figure 2.7 represents the DSM for a duodenum of a specific patient. The duodenum was contoured according to RTOG guidelines and reviewed by a radiologist. An oesophagus from a lung cancer treatment (with a prescription of 60 Gy in 30 fractions to the planning target volume) was also unwrapped to show the generalisability of this method (Figure 2.8). The oesophagus

travels from the neck to the stomach relatively centrally down the thorax. Since most cancer treatments, including lung, utilise multiple beam angles, the oesophagus can be considered an organ at risk for both left and right lung tumours. However, the oesophagus is most at risk with centrally located lung tumours. The oesophagus is also useful to consider in this thesis as it is tubular (like the duodenum) but not as tortuous, meaning that other unwrapping methods can be applied to it. Figure 2.8 shows a comparison between a DSM produced using a slice by slice unwrapping technique and a DSM produced using the method developed in this chapter. A gamma comparison at 3%/3px shows a 96% agreement. Visual comparisons of dose maps with various dimensions show a 30 $\times$ 30 pixel dose map provides a sufficient resolution to view features of interest.

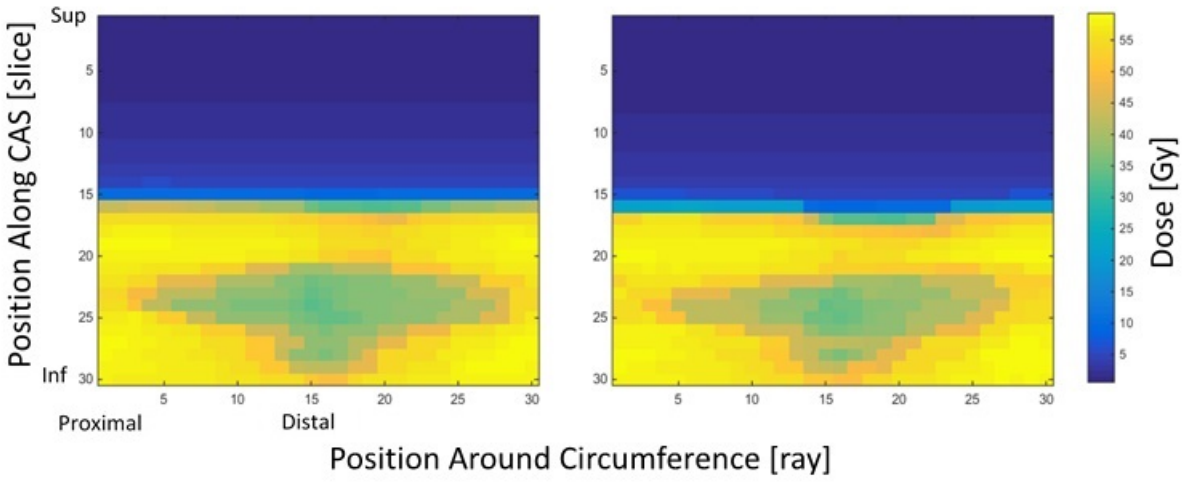


Figure 2.8: Dose surface map for an oesophagus unwrapped slice-by-slice (left) and using the method described in this paper (right). The y-direction comprises of the slices through the oesophagus from superior (top) to inferior (bottom). The x-direction comprises of the surface points at each slice unwrapped from the point proximal to the PTV so the centre of each DSM is the point on the circumference most distal to the PTV.

Lookup tables were created to provide dimensions of each pixel by calculating the

distances to the next circumferential point and to the circumferential point in the next slice in order to extract absolute feature size. The lookup table is specific to each duodenum, and is in the form of a 30 × 30 matrix where each cell contains the x and y dimensions of the corresponding pixel on the dose surface map. Averages, instead of individual pixel size calculations, were found to be unsuitable due to the range of variations (up to 6 mm in one dataset) between pixels. These variation are seen due to the orientation of slices around areas of high curvature.

2.3.2 Robustness

2.3.2.1 Slice Selection

Different ways of uniformly sampling the 200 central axis spline points were compared and the gamma analysis results show very similar dose-surface maps (Table 2.1). First, a reference DSM was chosen where every 6 points between CAS points 14 and 188 were selected (i.e. 14, 20, 26, ..., 182, 188). There was no overlap in this selection. A shift was introduced and two further slice selections with no overlap were created using every 6 slices between 10-184 (Shift 1) and 18-192 (Shift 2). The 3%/3px gamma results showed there is nearly no difference in dose-surface maps based on starting slice.

The selection of the reference dose-surface map is arbitrary and is not supposed to represent a gold standard. Since the unwrapping of the duodenum has never been done before there is no gold standard with which to compare this method. The comparison to a reference DSM, however, still shows the robustness of the method to variations in slice selection.

Additionally, the reference DSM (14-188 every 6 points) with no overlap was compared to a DSM with the same slice selection (14-188 every 6) but with overlapping slices (Overlap). This was done for the three patients by creating an additional central axis spline for testing purposes which resulted in overlap. In these cases the gamma is reduced to below the accepted threshold of 95% in 2 out of the 3 duodena (91%, 100%, 52%).

	Shift 1	Shift 2	Overlap
Duodenum 1	99%	99%	91%
Duodenum 2	100%	100%	100%
Duodenum 3	100%	100%	52%

Table 2.1: Slice selection robustness. 3%/3px gamma results comparing a reference selection (every 6 points from 14-188 with no overlap) for 3 patients to shift 1 (every 6 from 10-184 with no overlap), shift 2 (every 6 from 18-192 with no overlap) and overlap (every 6 from 14-188 with overlap).

2.3.2.2 Spline Selection

The four dose-surface maps created from four separate spline selections for the same dataset by the same user were comparable with 3%/3px = 98% (95-100). Two further users were asked to select a central axis spline for one dataset. The DSMs produced by these users were compared to the DSM produced by the experienced user. Both users' DSMs were close to the accepted gamma with 3%/3px = 96% and 94%. This shows that the unwrapping method is robust to the human selection element of the process.

2.3.2.3 Overlap Fix

In some cases with overlap, 30 sided planar polygons are replaced by 30 sided non-planar polygons. The validity of using non-planar polygons instead of flat polygons

in areas of overlap was tested by replacing flat polygons with non-planar polygons in 2 duodena that had no overlap. Planes were replaced in two straight edges of the duodenum (S1, S2) and one bend (B). The DSMs produced by replacing 3 and 5 slices were compared to the original non overlapping plane DSMs and were found to be very similar (Table 2.2).

	Duodenum 1	Duodenum 3
S1(3)	100%	100%
S2(3)	100%	100%
B(3)	100%	100%
S1(5)	99%	100%
S2(5)	100%	100%
B(5)	100%	100%

Table 2.2: Robustness (gamma 3%/3px) of replacing 3 (3) or 5 (5) planes with 30 sided polygons in two straight sections of the duodenum (S1, S2) and one bend (B) for 2 datasets (Duodenum 1, Duodenum 3).

2.4 Discussion

2.4.1 Unsuccessful Attempts

Before discovering that the best solution to get the correctly orientated slices was using a new axis, two other methods were attempted. The first method used a spline which was fit to the most distal and proximal points to the tumour and discretised. The points on these splines were connected and the normal defined as the orthogonal bisector from the midpoint of the following distal-proximal line. The orientation of these planes were meaningful at the superior portion of the duodenum, but not once the curvature increased. In the second attempt an ellipse with the smallest circumference was fit to a slice of the duodenum. As the ellipse was moved (in the direction of the normal to the plane) through the duodenum it was perturbed to find

the smallest perimeter once again. The smallest perimeter was also not a good proxy for correct plane orientation and this method was also computationally intensive.

2.4.2 Dose Surface Maps

Dose-surface maps can be used to improve planning constraints, toxicity models, and daily maps to check the delivered dose matches the planned dose. To our knowledge, this thesis is the first to present 2D dose surface maps of the duodenum and this method is applied to clinical trial data. This is the first description of a new methodology for creating DSMs which generates a new coordinate system, defined as the position along the central axis spline, which overcomes the problems of the simple transaxial CT slice approach. This method has been successfully demonstrated, is robust, requires minimal human interaction, and has been shown to be generalisable.

The panel of DSMs in Figure 2.7 show a large variation in dose distribution for the 15 duodena. Even though each patient was on the same clinical trial and was treated to the same prescription, the different tumour locations and patient anatomy resulted in very different dose distributions.

In the more complex cases where overlap cannot be completely overcome using just the central axis spline, non-planar polygons between fixed planar polygons are used to evenly and meaningfully sample the entire organ. The robustness of using non-planar polygons instead of flat polygons has been shown to have very little effect on the resulting dose surface map when there is no overlap in the slices. Therefore, the DSMs produced using the overlap fix method described when the overlap is not overcome through the initial central axis spline selection provide a valid description

of the surface dose.

The problem of overlapping planes when unwrapping organs was acknowledged in work unwrapping the rectum [34] where this was avoided but not quantified. In other work it has been ignored. In virtual colonography overlapping planes are avoided by bending the rays cast from the centre line. In this method we present an alternative solution which keeps the rays linear but moves the central axis. We have also quantified the effect of overlapping planes on dose-surface maps for the first time.

Due to the complex shape of the duodenal surface the DSMs present a relative space that can be converted to absolute size. The curvature of the organ is such that the distances between pixels on the dose map vary. For this reason a pixel specific lookup table was created to convert from pixels to surface area. Therefore, extracted features from the DSM can either be described in absolute size or in relative position along the organ.

Compared to previous methods applied to other organs [30, 34, 35], which can only be used when the CT transaxial slices can be unwrapped individually, this approach allows for the unwrapping of any tubular organ and also provides a mechanism for checking and fixing overlapping planes. However, this thorough approach to a generalisable non-overlapping tubular unwrapping technique also leads to an element of human interaction in the selection of start and end points.

Validation of this method is a multi-faceted problem. There may be a need to validate the unwrapping geometry but also, and we believe more importantly, there will be a need to validate the predictive model that can now be built using spatial information from the DSMs against clinical toxicity data. There is currently no

commercial software or alternative method which can produce DSMs of the duodenum against which we could validate our approach. The methodology described in this chapter was, however, validated against a slice-by-slice approach to the oesophagus. The 96% gamma agreement was reassuring but perhaps more organs should have been tested. However, since there is only qualitatively described theory and no publicly available code detailing other unwrapping methods, this would still not be a true independent validation.

In Chapter 6 other means of validation of the unwrapping geometry will be discussed such as using a custom phantom or a post-operative pathological sample which can be physically cut open and unwrapped.

2.4.3 Robustness

Although dose surface maps have been produced for other organs, their robustness has not been quantified. A preliminary study was undertaken to investigate the effect of different sampling techniques, overlap, different central axis definitions (intra- and inter-user variation), and different length and curvature penalties on the dose map.

The most spatially meaningful sampling of the organ requires uniform slice selection throughout the duodenum and that the angular slices do not overlap. The robustness of the dose surface maps to where these slices start and end shows that there are only very small differences (gamma 3%/3px $>$ 99%). These differences increase when looking at the effect of overlapping planes where gamma (3%/3px) can be reduced to as low as 52% compared to non-overlapping planes, highlighting the need for a solution to the plane overlap problem. Since there is very little difference

in dose-surface maps based on how the slices were selected, as long as there was no overlap, when the central axis spline is automatically created with the racecar path, it is only discretised to the 30 points needed for the dose-surface map.

The method was also found to be robust to the human selection process, testing both inter- and intra- user differences resulting in gamma 3%/3px between 94-100%. The control points selected for each instance were not necessarily the same and still returned very similar maps. This suggests that the overlap problem causes the most change to the DSMs and needs to be considered when creating dose-surface maps.

The effect of overlapping planes on the dose surface map was expected because each overlapping plane results in a spatially meaningless row on the dose surface map. The effect of overlap varied for the three duodena studied. On one duodenum overlap had almost no effect whereas on another the gamma 3%/3px between the non-overlap DSM and the overlap DSM was 52%. This range is also expected as overlap can mean just the edge of two planes overlapping, as seen in Figure 2.5, or it can mean a few planes overlapping in areas of high curvature, as illustrated in Figure 2.2 which can lead to sampling from an area of the surface that is very distant to the area intended.

In areas of high curvature or complex geometry, the 'racecar' algorithm requires a minimum of one voxel separation between two outside surfaces to ensure that the anatomy of the organ is honoured and the path does not 'jump' between two areas. However in reality such curvature does not occur in the duodenum. Additionally, such curvature would present a greater obstacle at the contouring stage. If such a case would need to be solved, an increase in grid resolution using interpolation could be added to solve such edge cases.

2.5 Conclusion

Dose-surface maps produced provide previously unexamined information on the spatial dose distribution in the duodenum which can now be explored to create models that may improve duodenal toxicity predictions. When unwrapping 3D hollow organs to a 2D dose-surface map care must be taken to ensure slices don't overlap. Spatial dose metrics can now be extracted from the DSMs and the best predictors for duodenal toxicity can be identified. The method developed in this chapter can also be generalised and extended to other hollow organs

Chapter 3

Further Applications of Unwrapping Methodology

In this chapter, the methodology presented in chapter 2 will be extended to other organs: the stomach and the bronchial tree. A graphical user interface which connects to commercial treatment planning systems is developed in order to translate the work from chapter 2 into a clinically-accessible format.

3.1 Introduction

Prior to this thesis, hollow organs such as the oesophagus, anal canal, rectum, and bladder had been unwrapped to produce dose-surface maps in order to access information about the spatial distribution of dose on the organ surface (Section 1.7). In Chapter 2, dose-surface maps were produced for the duodenum for the first time. In this chapter, we investigate the generalisability of our novel method in other hollow organs that have not been unwrapped.

Since the primary focus of this thesis is related to pancreatic chemoradiotherapy, the next hollow organ we turned our attention to after the duodenum was the stomach. Recommendations from the seminal QUANTEC review limits conventionally

fractionated (1.8 - 2 Gy per fraction) dose to the whole stomach to less than 45 Gy [19]. Similarly to the duodenum and in line with the QUANTEC review, previous efforts to correlate toxicity and dose to the stomach have been volume based [22, 23, 71, 72]. As introduced in Section 1.6, there is little consensus on which stomach dose-volume metrics are important in predicting toxicity. There are a number of studies [73, 71, 74, 72] that use endoscopy techniques to try to locate gastric ulcers, bleeding or even perforation. Creating dose-surface maps for the stomach will enable the exploration of correlation between toxicity and the spatial distribution of dose on the stomach surface.

The stomach is geometrically simpler than the duodenum and therefore extending our unwrapping methodology is not mathematically challenging. An organ which does add geometric complexity to the unwrapping process is the bronchial tree. Extending our methodology to handle the bifurcations of the bronchial tree added another level of complexity.

Investigation of dose received by the bronchial tree may be crucial for research into stereotactic ablative radiotherapy (SABR) treatment for inoperable early-stage non-small-cell lung cancer (NSCLC). While surgical resection is the standard of care for early-stage NSCLC, some patients present with inoperable disease. For these patients, SABR treatment has been shown to provide high-quality outcomes [75, 76]. However, due to the proximity of centrally located organs at risk such as the bronchial tree, excessive toxicity has been reported in various studies.

Timmerman et al [77] warned about toxicity as early as 2006 and recommended their regime of 60 - 66 Gy in 3 fractions should not be used in patients with central

tumours. This study found that patients with perihilar/central tumours have an 11 fold increased risk of experiencing toxicity compared with more peripheral locations. A zone considered as up to 2 cm away from the proximal bronchial tree (PBT) was described and incorporated into Radiation Therapy Oncology Group (RTOG) protocols as a 'no treatment zone' for future trials. RTOG 0236 [76] also investigated SABR treatment for inoperable early-stage NSCLC but excluded patients with central tumours. This trial reported no SABR-related patient deaths which is in contrast to the 2006 Timmerman et al study [77]. Haseltine et al [78] investigated the dependence of toxicity on tumour proximity to the PBT and reported fatal complications after SABR treatment for central lung tumours as recently as 2016. They found that the risk of SABR-related death was significantly higher for tumours abutting the PBT. Another report using a different fractionation schedule discusses fatal central-airway necrosis presented more than 8 months after a treatment of 50 Gy in 5 fractions [79]. Yet another fractionation schedule of 70 Gy in 10 reports similar clinical outcomes in central and peripheral lung tumours without an increase in toxicity [80]. LungTech [81], a prospective multicentre study into SABR for central lung tumours was opened in 2015 treating to 60 Gy in 8 fractions in an attempt to find a consensus on maximum tolerated doses.

With over a decade of reports on toxicity due to dose to the bronchial tree, the only metrics ever studied were dose to the volume of the bronchial tree and distance of tumour from the bronchial tree. By extending the unwrapping methodology we developed in chapter 2 to provide dose-surface maps of the bronchial tree, we allow the investigation of the spatial dose distribution on the bronchial tree surface to better

understand toxicity, especially in treatment of central lung tumours. However, the use of the bronchial tree dose-surface maps is outside the scope of this thesis and therefore the bronchial tree unwrapping process is left as a demonstration of broader applicability of this unwrapping methodology.

In some organs, dose-surface maps (DSMs) have been investigated for toxicity prediction for over a decade (Section 1.7). Spatial dose distribution information has for too long been limited to research and separated from clinical decisions. This is most likely because unwrapping techniques have remained mostly in non-clinical systems such as MATLAB (The MathWorks, Inc., Natick, MA) or standalone commercialised software such as VODCA (MSS Medical Software Solutions GmbH, Hagendorn, Switzerland). Some of the shortcomings of VODCA as a tool for unwrapping include cost and an inability to handle more geometrically complex organs such as the duodenum and even some rectum geometries. An implementation of our unwrapping technique described in chapter 2 within a software package that directly interfaces with supported treatment planning systems is presented in this chapter to improve integration with the clinical workflow. Currently supported TPSs are RayStation (RaySearch Laboratories AB, Stockholm, Sweden) and Eclipse (Varian Medical Systems, Inc., Palo Alto, California). This software package will allow any hollow organ (without bifurcation) to be unwrapped.

3.2 Materials & Methods

3.2.1 Stomach

The same patient dataset described in Section 2.2.1 was used consisting of 81 patients from two clinical trials, ARCII (n=19) and SCALOP (n=62). As for the duodenum, in both trials the stomach was contoured retrospectively according to the Radiation Therapy Oncology Group (RTOG) atlas and guidance [65].

The methodology described in chapter 2 is used to unwrap the stomach.

3.2.2 Bronchial Tree

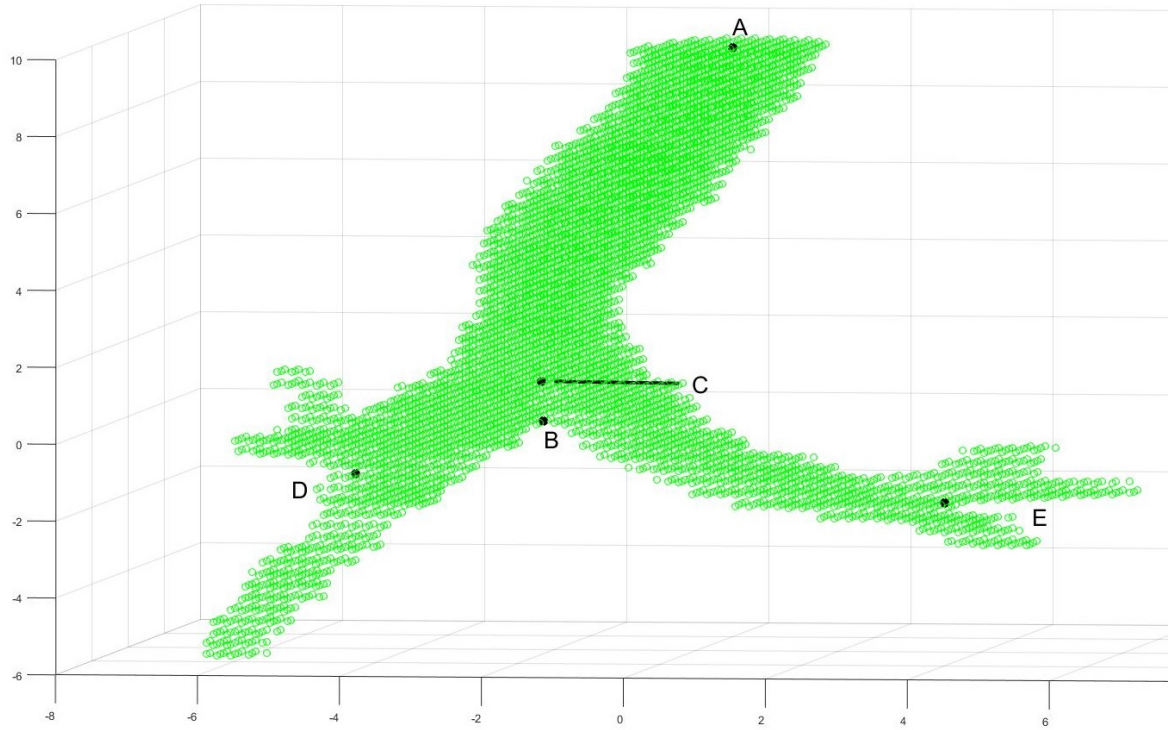


Figure 3.1: 3D point cloud of a bronchial tree (green). Start and end points of each segment in black. Segment 1 = AB (trachea), Segment 2 = CD (right primary bronchus), Segment 3 = CE (left primary bronchus).

In order to deal with the bifurcation of the bronchial tree, each segment (branch)

will be unwrapped individually using the unwrapping methodology described in chapter 2.

While only one start and end point is needed to unwrap organs without bifurcation, for the bronchial tree a user defined start and end point is required for each segment. With reference to Figure 3.1, the first segment to be unwrapped, the trachea, was between points A (start) and B (end). The bronchial tree then bifurcates into two segments; the right primary bronchus between points C (start) and D (end), and the left primary bronchus between points C (start) and E (end).

As shown in Figure 3.2, when creating angular slices for a bifurcated segment (segment 3), the most superior few slices may sample points from the opposite bifurcated segment (segment 2). In order to fix this, the start point of the segment is moved so that the first angular slice is only sampling points from the correct segment (Figure 3.3). This is done by creating a line that passes through points C and B and then finding the first slice in the segment that is not intersected by that line.

At this stage there is still a natural overlap where one segment and the bifurcated segments below it sample the same space twice. These areas are identified and those locations on the superior segments' dose-surface map are set to zero (Figure 3.4). An unwrapping marker is set as a point 5 cm anterior to the most anterior point on the bronchial tree.

This method is applied first using a bronchial tree contour with a dummy dose at each contour point equal to the absolute value of the y-coordinate. Then the bronchial tree of a patient treated according to the LungTech constraints to 60 Gy in 8 fractions is unwrapped. The planning constraint to the trachea/main bronchus

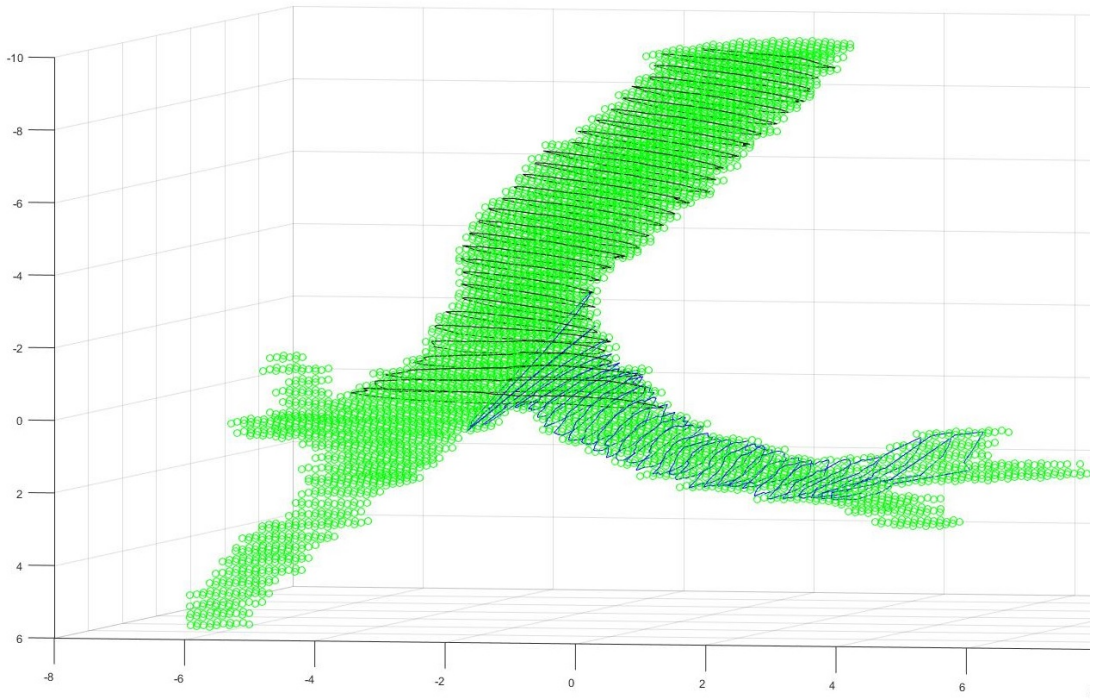


Figure 3.2: Placement of angular slices in segments 1 and 3 prior to adjustment of start point of segment 3.

is to limit the maximum dose to 44 Gy. This patient was chosen because they had a central tumour in a similar position to the patient with reported fatal central-airway necrosis [79].

3.2.3 TPS Integration

By compiling the MATLAB code for the unwrapping methodology described in chapter 2, we were able to interface with a treatment planning system using IronPython.

A graphical user interface (GUI) was set up to allow a user to select the following information from their TPS;

1. Patient Name

2. Plan Name

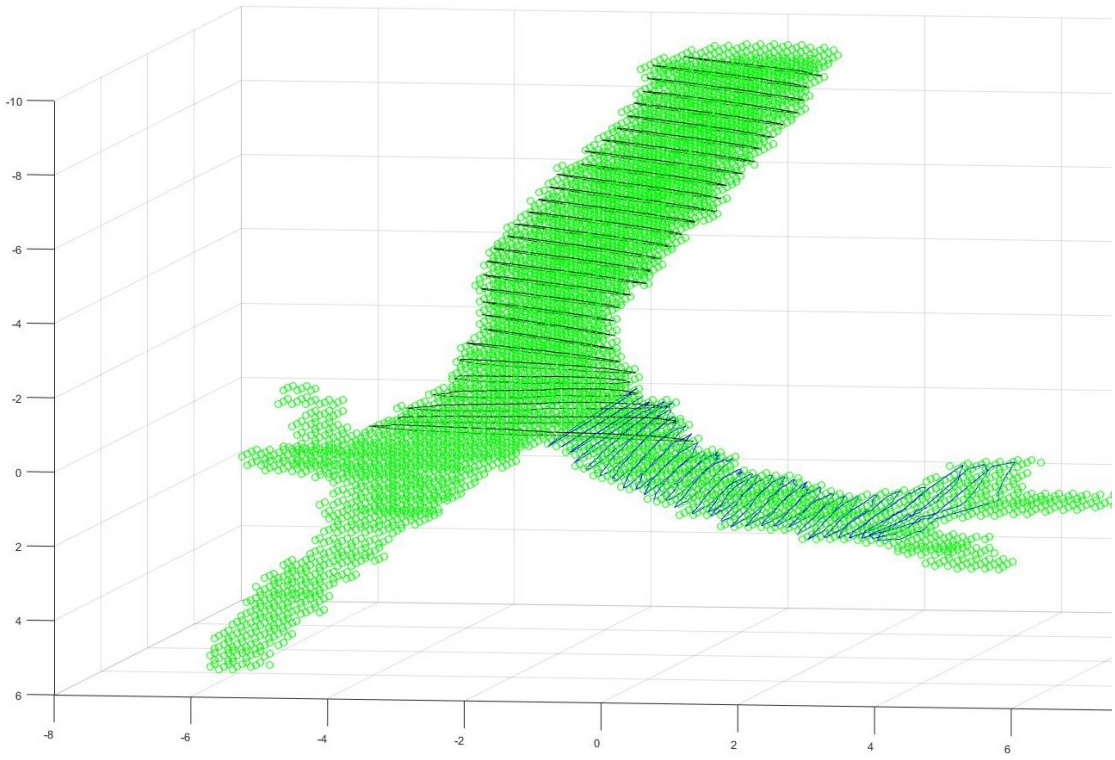


Figure 3.3: Placement of angular slices in segments 1 and 3 after adjustment of start point of segment 3.

3. Structure Name

4. Start Point

5. End Point

This information was passed to the MATLAB compiled code that processed the unwrapping. The resulting dose-surface map is then displayed in the graphical user interface.

For each organ the software package can be configured to select appropriate dose-surface map dimensions (30 x 30 by default) and to set an unwrapping marker (isocentre by default).

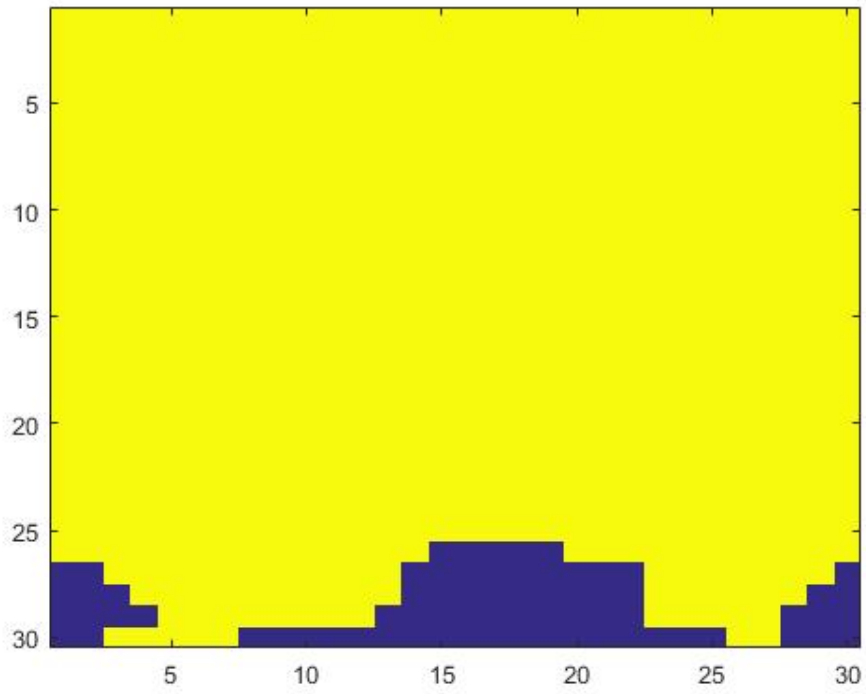


Figure 3.4: Identification of corners of a 30 x 30 bronchial tree segment map that are sampled by the bifurcated segments below it. Dose at the yellow pixels are excluded from the dose-surface map as they are included in the dose-surface map of another segment.

3.3 Results

3.3.1 Stomach

The unwrapping methodology described in chapter 2 was successfully used to unwrap stomachs from the 81 patients in the ARCII and SCALOP clinical trials. Figure 3.5 shows 15 of these stomachs from the ARCII dataset. Each panel in Figure 3.5 represents the DSM for a stomach for a specific patient. The stomach was contoured according to RTOG guidelines and reviewed by a radiologist.

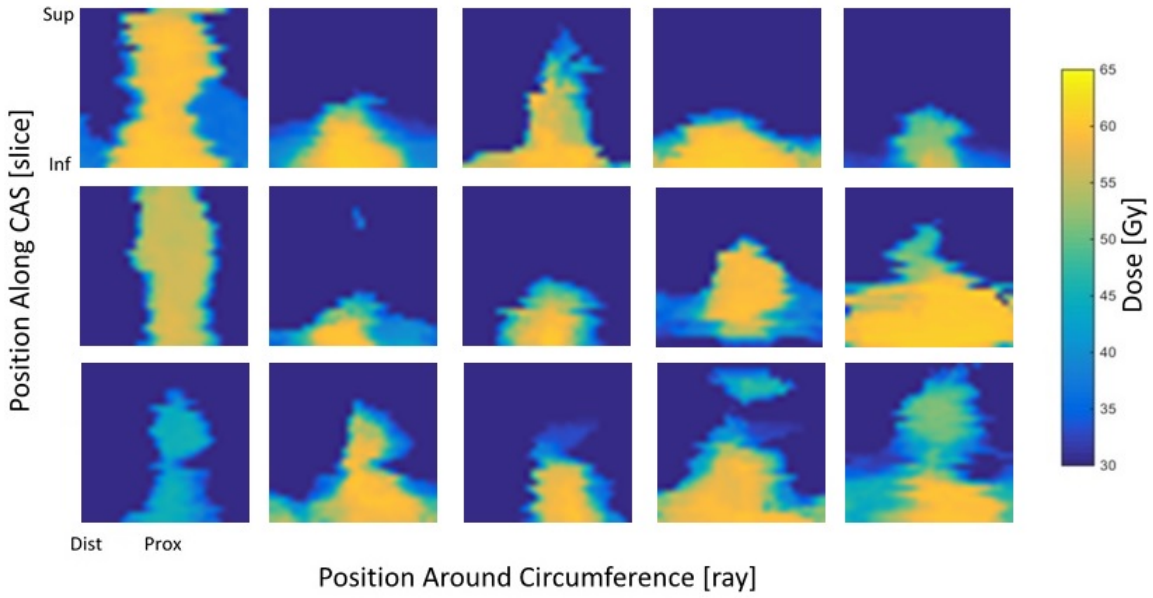


Figure 3.5: Dose surface map for 15 unwrapped stomachs with different dose distributions. The x and y axis labels are for each individual DSM. In the y-direction, each map comprises of the slices through the stomach from superior (top) to inferior (bottom). In the x-direction, each map comprises of the surface points at each slice unwrapped from the point distal to the PTV so the centre of each DSM is the point on the circumference most proximal to the PTV.

3.3.2 Bronchial Tree

A bronchial tree was successfully unwrapped using a modified version of the unwrapping methodology described in chapter 2. A dose-surface map was created for each segment individually, and points that were sampled in two segments' dose-surface maps were removed from the DSM of the more superior segment and set to white. Figure 3.6 shows the three dose-surface maps for the three segments labelled 1 (trachea), 2 (right primary bronchus), and 3 (left primary bronchus) in Figure 3.1. The dose at each point on the bronchial tree is set as the absolute value of the y-coordinate in gray for method development.

The anatomy of the bronchial tree and location of the PTV in a LungTech patient

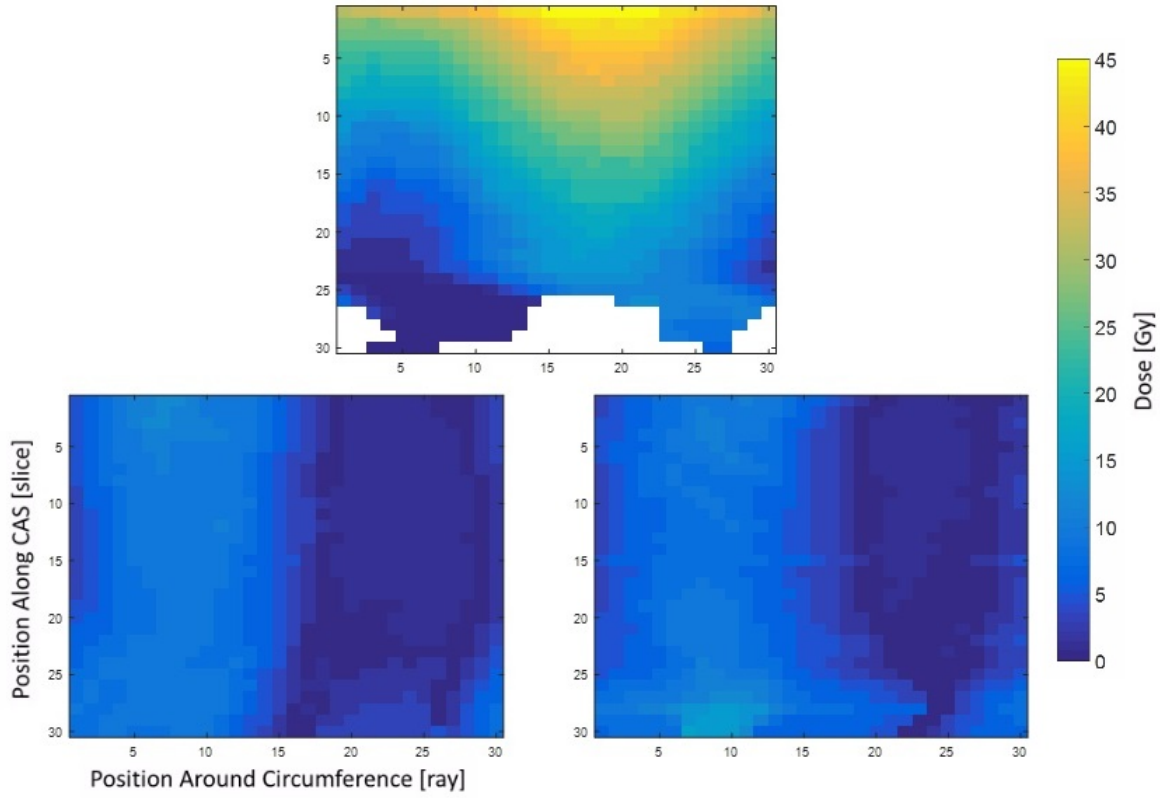


Figure 3.6: Dose-surface maps for the trachea (top row) and the two main bronchi (second row). The dose is set as the absolute value of the y-coordinate and the dose colour wash (in gray) scale is the same across all maps.

is shown on the top in Figure 3.7 and the dose distribution on the bronchial tree is shown on the bottom.

Unwrapping this dose distribution on the bronchial tree results in the dose-surface maps shown in Figure 3.8. The top DSM is the trachea and the pixels represented at the top of the main bronchi DSMs on the second row have been removed. The left main bronchus DSM is shown on the right hand side of the second row and has low dose as it is contralateral to the PTV. The right main bronchus DSM is on the left hand side of the second row and has had the pixels removed that are represented in the DSMs on the row below. The third row contains the DSMs of the two branches

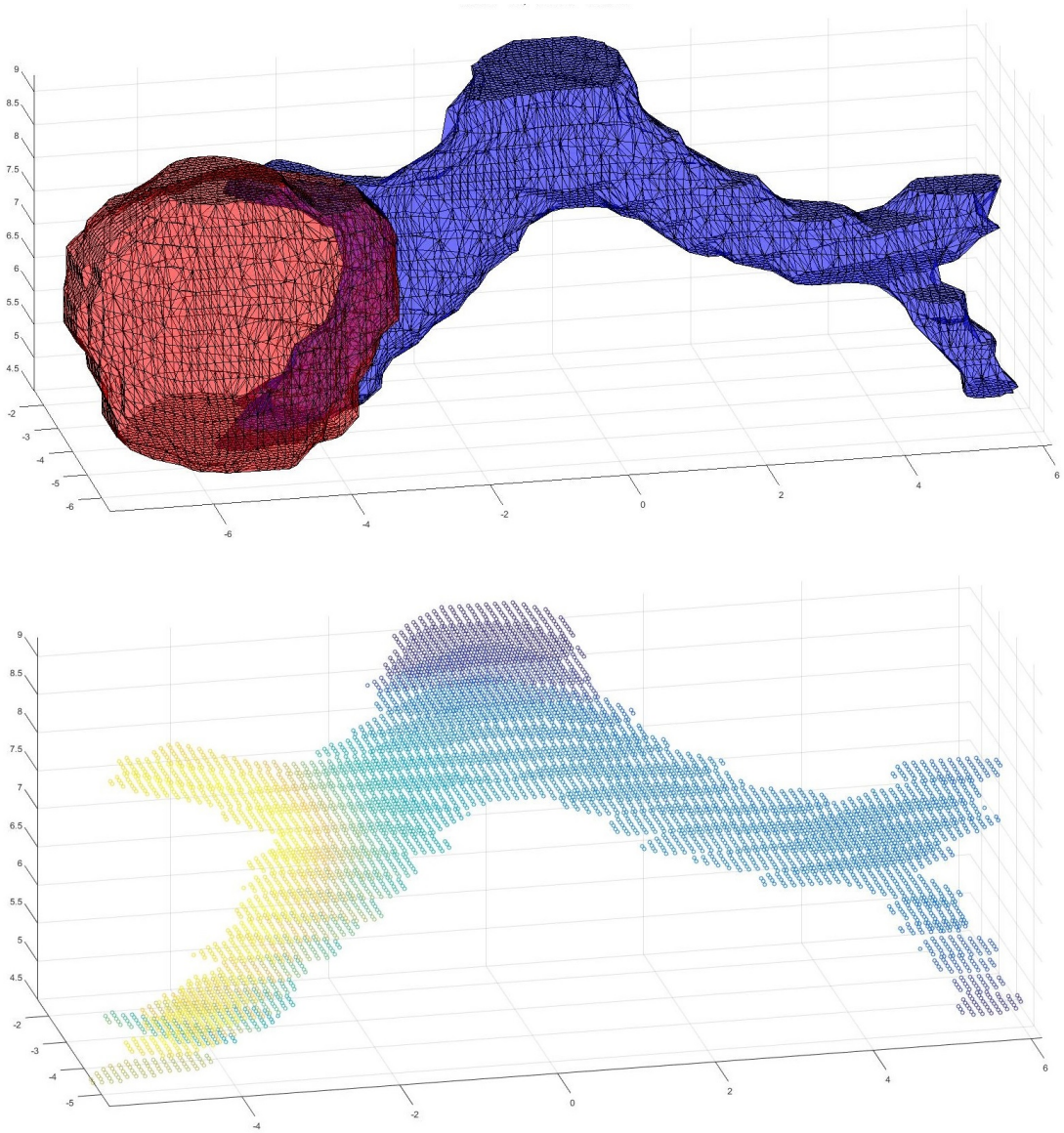


Figure 3.7: Top: Position of PTV (red) invading the bronchial tree (blue). Bottom: Dose distribution on the bronchial tree shown with a dose colour wash (0 - 45 gray).

of the bronchial tree that split from the right main bronchus. The dose scale for all the DSMs is the same (0 - 45 Gy).

3.3.3 TPS Integration

A graphical user interface shown in Figure 3.9 was created to allow the user to select a patient and a plan from a treatment planning system. The user was then able to

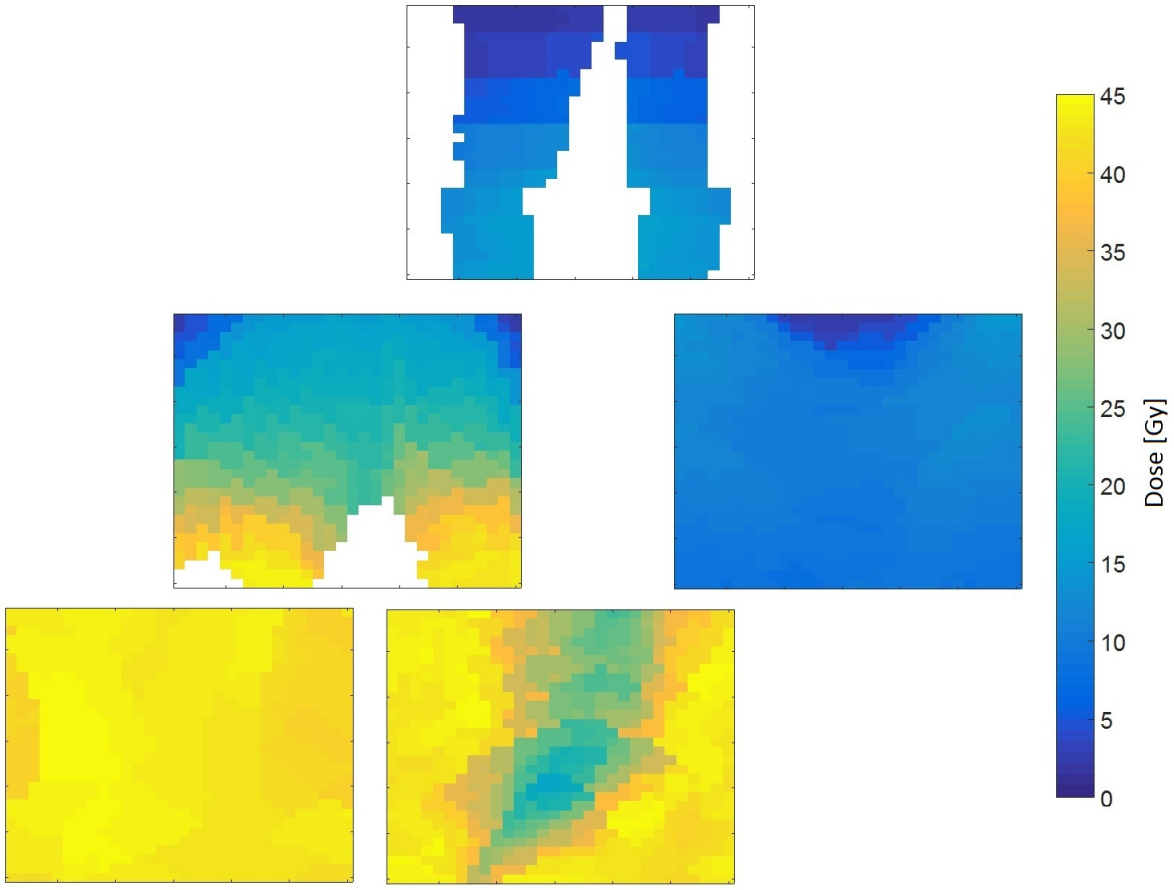


Figure 3.8: Top row: Dose-surface map for trachea. Second row: DSMs for right and left main bronchi. Third row: DSMs for two branches that split from the right main bronchus. Dose-surface maps have dose scale (0 - 45 gray).

select any structure to unwrap, along with a start and end point for that organ. The software package then utilised the unwrapping methodology described in chapter 2 to return a dose-surface map.

3.4 Discussion

The unwrapping methodology described in chapter 2 was successfully used to unwrap the stomach without modification. Even though the stomach could be unwrapped using methods in existence before this thesis, to our knowledge these are the first

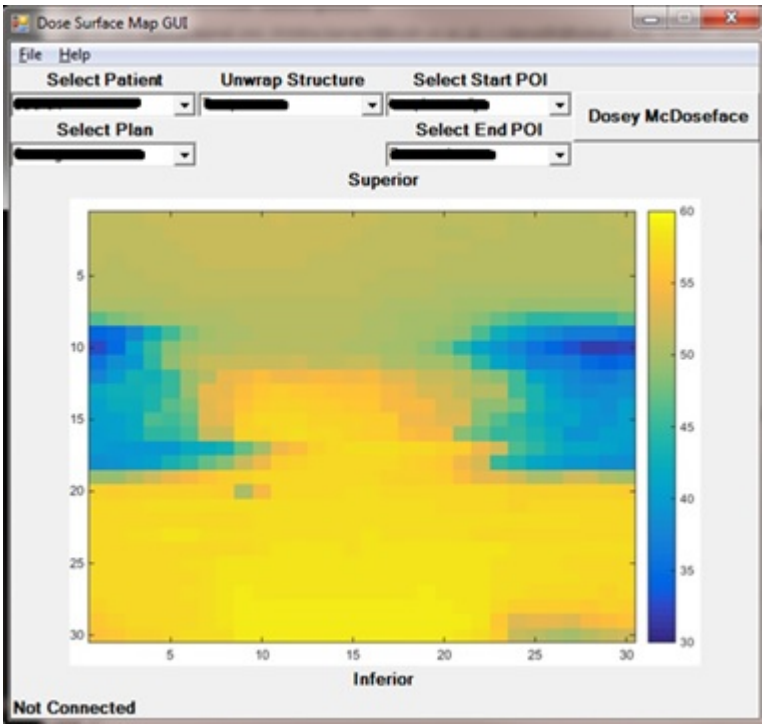


Figure 3.9: Graphical user interface for dose-surface map production. Example dose-surface map shown is a 30 x 30 duodenal DSM from a clinical trial. Dose colour wash presented in gray.

stomach dose-surface maps produced. The stomach DSMs produced (some seen in Figure 3.5) have more dose in the lower (inferior) half because this region is closer to the PTV.

As discussed in Section 1.6, current understanding of upper gastrointestinal toxicity in based on dose-volume information. Some studies have used endoscopy to identify ulcers in the stomach and duodenum [73, 71, 74, 72]. Shinoto et al [72] specifically found gastric ulcers and in those cases it would have been useful to consider the spatial distribution of dose on the surface of the stomach. This would have been possible with stomach dose-surface maps as produced in this chapter.

The bifurcation of the bronchial tree presented a new challenge in the unwrapping process. By treating each branch of the bronchial tree as a separate segment that

needed unwrapping, the problem was simplified to finding which areas of each segment were sampled twice. Similar code that was used to identify overlapping slices in chapter 2 was used to find these locations and they could be excluded from the dose-surface map. We have shown that dose-surface maps can be produced for each branch on the bronchial tree as a proof of concept. This will be useful in datasets which report toxicity in central lung tumours, as the effect on toxicity of the spatial distribution of dose on the bronchial tree surface can be studied and new constraints can be investigated. Toxicity in various non-small cell lung cancer SABR trials can be excessive or even fatal, especially when treating tumours located close to the proximal bronchial tree [77, 78]. A patient treated with the same prescription and constraints as the LungTech clinical trial [81] had a central lung tumour in a similar position to the patient reported to have developed fatal central-airway necrosis [79] shown in Figure 3.10. Unwrapping the bronchial tree allows the visualisation of the spatial dose distribution which could be useful in predicting necrosis. Future SABR studies for central and peripheral lung tumours may benefit from investigating bronchial tree dose-surface maps and correlating these with toxicity.

Institutions utilising the software package described in this chapter will be able to create dose-surface maps for any hollow organ (without bifurcation). This has advantages for both clinical and research teams. Clinically, this will allow visualisation of the spatial surface dose distribution, and will help incorporate the use of spatial metrics already reported in the literature for toxicity reduction. Research teams will be able to study the spatial features that correlate with toxicity for multiple organs using a much larger dataset now that dose-surface maps can be easily created from

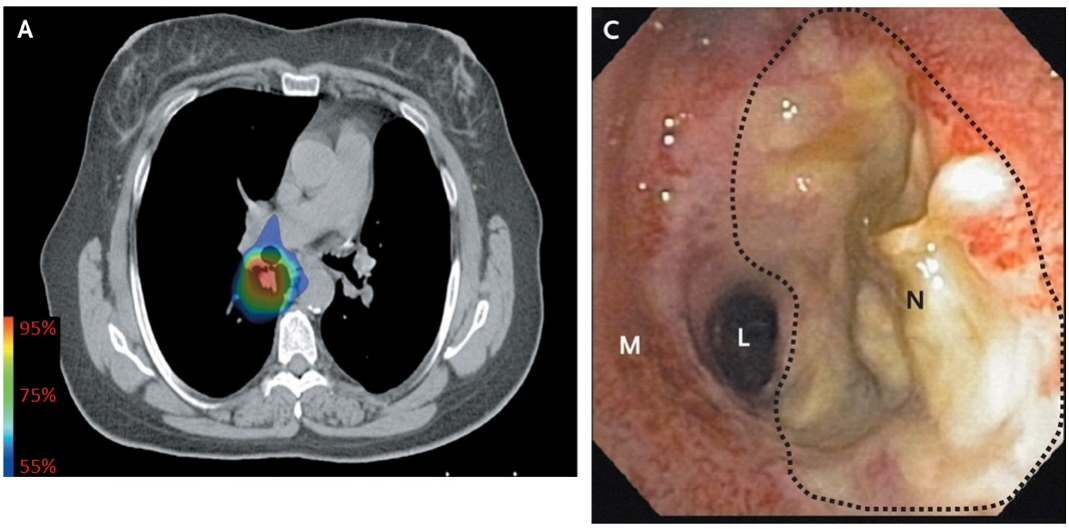


Figure 3.10: Panels A shows an axial image of a central tumor in the right lower lobe of the lung obtained at presentation with computed tomography, with overlaid treatment plans for stereotactic ablative radiation therapy (SABR). Target dose is as indicated in the colour key, with blue indicating 50% of the prescribed dose and red 100%. Endobronchial ultrasound-guided bronchoscopy, performed 8 months after treatment, shows a plaque-like area of mucosal necrosis in the right mainstem bronchus (Panel C). The necrotic area extended from the midright mainstem bronchus to the right bronchus intermedius and right hilum along the posterolateral aspect of the airway. The necrotic area (N) is outlined and is adjacent to normal mucosa (M) and the lumen (L) of the right mainstem bronchus. Reproduced with permission from [79], Copyright Massachusetts Medical Society.

patients in the clinical treatment planning systems. As more spatial features are found, the clinic can implement these constraints faster as dose-surface maps are already easily producible.

Dose-surface maps are especially useful for research when coupled with follow up information, making this software package also appealing for use on clinical trials. When toxicity information is available, specific spatial locations that are more discriminative of toxicity outcome can be further studied to improve radiotherapy planning and pathological knowledge.

3.5 Conclusion

In this chapter, the method developed in chapter 2 for the duodenum is extended to other organs, and made accessible within the clinical workflow.

In pancreatic chemoradiotherapy, upper gastrointestinal toxicity is not well understood. Ulcers are sometimes found in the stomach, as well as duodenum. Therefore, similarly to the duodenum, the new dose-surface maps produced for the stomach in this chapter can be used to correlate toxicity with the spatial surface dose distribution on the stomach using the two clinical trials available for this thesis.

This chapter also presents a working method to unwrap the bronchial tree. This method is developed from work in Chapter 2 and includes consideration for the bifurcation seen in the bronchial tree. Toxicity has been a major problem when treating central tumours in inoperable early-stage NSCLC with SABR. Our proposed solution to create bronchial tree dose-surface maps will allow for their examination and correlation to toxicity. However, this toxicity correlation in the bronchial tree will not be completed as part of this thesis.

Research often has a tortuous process of reaching clinical implementation, as has been the case in dose-surface map studies for organs such as the bladder and rectum. This has not been helped by the fact that the treatment planning system is separate to the research tools used such as MATLAB and VODCA. The software package described in this chapter brings dose-surface map production into a simple and clinically-connected workflow that provides institutions the opportunity to consider spatial information in treatment planning. This package will also increase the

amount of data available to researchers to investigate spatial parameters that are linked to toxicity.

Chapter 4

Feature Extraction for Toxicity Correlation

In this chapter the dose-surface maps produced in chapters 2 and 3 for the duodenum and stomach will be utilised. Traditional dose-volume and dose-surface metrics will be extracted and compared to new spatial metrics derived from these DSMs. The ability of these metrics to correctly classify patients according to toxicity will be compared. A new metric derived from the stomach DSM will be presented as the best classifier for upper-GI toxicity within these datasets.

4.1 Introduction

In external beam radiotherapy, dose to the tumour in pancreatic cancer is often limited by the proximity of healthy organs in the gastrointestinal (GI) tract such as stomach and duodenum. During treatment planning, constraints are placed on the volume of these organs receiving a threshold dose in attempts to avoid toxicity. These constraints are evaluated in clinical practice using a dose-volume histogram (DVH) as explained in Section 1.5. Recommendations from the QUANTEC review limits dose to the whole stomach to less than 45 Gy and the absolute volume of small bowel

receiving more than 15 Gy to 120 cm^3 if delineating individual bowel loops [19].

Section 1.7 discusses the hypothesis that in hollow organs it may be more useful to consider the dose given to the organ surface rather than dose to the entire organ volume. The first step towards this was using dose-surface histograms (DSHs) instead of dose-volume histograms. A few studies have shown the advantages of using DSHs in organs such as the rectum [24, 25, 26, 27], bladder [24, 28], and oesophagus [29] but this has not resulted in DSHs being used clinically. While the DSH is a step in the right direction for hollow organs, it still discards all spatial information about the dose distribution. In order to preserve this potentially useful information the dose-surface map is used.

Dose-surface maps (DSMs) allow for the visualisation of the spatial distribution of the dose on the surface of an organ. A review of various studies of the dose-surface map in organs such as the rectum, bladder, anal canal, and oesophagus is provided in Section 1.7. The methods by which the spatial information contained in these maps was utilised to build toxicity prediction models for these normal tissues was also discussed.

In Chapter 2, a method was presented to create duodenal dose-surface maps for the first time. In chapter 3 the same method was used to create stomach DSMs, again for the first time. In this chapter, the spatial information available in these dose-surface maps is explored and new dose metrics are created which incorporate spatial dose distribution information. The correlation of these new metrics with upper gastrointestinal toxicity (UGIT) are compared to that of traditional dose-volume and dose-surface metrics.

4.2 Materials & Methods

4.2.1 Overview

Traditional dose-volume metrics were extracted from the duodenum and stomach along with their equivalent dose-surface metrics and new spatial metrics, which describe the length of the organ over which a threshold circumference is spared a threshold dose. By using a permutation test to find a region of interest (ROI) within the dose-surface map, ROI metrics are also extracted. The predictive power of each of these metrics is compared by analysing the area under the ROC curve (AUC).

4.2.2 Patient Cohort

The same eighty-one patients, described in Section 2.2.1, from two clinical trials treating locally-advanced pancreatic cancer with chemoradiotherapy, ARCII (n=19, [57]) and SCALOP (n=62, [58]), were used in this analysis.

Each trial had different definitions for the planning target volume (PTV). In ARCII the PTV receiving the initial 50.4 Gy was defined as the primary tumour and elective lymph nodes, and the sequential 9 Gy boost was delivered just to the primary tumour (defined as the gross tumour volume (GTV) plus margins of 2 cm in the craniocaudal direction and 1.5 cm in other directions). In SCALOP the GTV was defined as the tumour visualised on the CT with lymph nodes greater than 1 cm diameter. The PTV included this GTV with the same margins as defined in the ARCII boost.

Due to the different prescription target definition and doses in these two trials the data was not pooled for analysis.

Neither trial specified any specific duodenal or stomach constraints for treatment planning and in both trials adverse events (toxicity) were prospectively recorded and graded according to the Common Terminology Criteria of Adverse Events (CTCAE) version 4.0 (ARCII) and version 3.0 (SCALOP).

In ARCII clinical assessments were performed weekly during chemoradiotherapy, 6-8 weeks post-treatment, and every three months thereafter until one year after trial entry. In SCALOP assessments were monthly during induction chemotherapy, weekly during chemoradiotherapy, two weeks post-chemoradiotherapy, and three and six months later.

For this chapter a sinlge toxicity endpoint of upper-gastrointestinal toxicity (UGIT) was defined as symptoms included in the Radiation Therapy Oncology Group (RTOG) definition of acute UGIT (nausea, vomiting, abdominal pain, GI bleeding/perforation, bowel obstruction, anorexia $\pm$ weight loss) [82]. The maximal grade of any of these symptoms recorded for a patient during a period of three months from the start of chemoradiotherapy was identified and recorded as the UGIT grade.

4.2.3 Organ Unwrapping

The stomach and duodenum for each patient was unwrapped using the methodologies described in Chapters 2 and 3 to produce a 30 x 30 dose-surface map for each organ for each patient. As explained in Chapter 2, in order to meaningfully unwrap the organ, slices that sample the organ surface must be non-overlapping and appropriately orientated. To find these slices, a path is required which regulates both length and curvature. This path is found, and rays are cast towards the surface on a plane

normal to the vector between the previous and next point on the path, creating angular perimeter slices. The angular slices are unwrapped from the point distal to the centre of mass of the PTV to provide a common unwrapping point for all patients. This has the effect of placing hotspots centrally on the dose-surface maps.

4.2.4 Traditional Dose Metrics

For both the stomach and duodenum, traditional dose metrics were extracted. Clinically-accessible dose-volume metrics such as mean dose ($D_{mean,V}$), maximum dose ($D_{max,V}$), volume receiving at least 5 (V_5), 15, 25, 35, 45, and 55 Gy were extracted for each organ. Furthermore, less commonly used dose-surface metrics such as mean surface dose ($D_{mean,SA}$), maximum surface dose ($D_{max,SA}$), surface area receiving at least 5 (SA_5), 15, 25, 35, 45, and 55 Gy were extracted from the dose-surface maps. These metrics are summarised in Table 4.1. Both the dose-volume and dose-surface metrics were extracted in absolute (mm^3/mm^2) and relative (%) terms. Absolute metrics in mm^2 were extracted from the dose-surface map by taking into account the size of each pixel in the map. Both dose-volume and dose-surface absolute metrics will be referred to in the results as, for example 'V_5 (abs)', whereas the relative term will remain simply as 'V_5'.

Univariate analysis using the Wilcoxon rank-sum test was used to find significant parameters in predicting grade $\geqslant 2$ and grade $\geqslant 3$ UGIT. The Wilcoxon rank-sum test (also known as the Mann-Whitney U test or the Mann-Whitney-Wilcoxon) is a non-parametric (does not assume specific distribution of data) test to determine whether two independent samples were selected from populations having the same

Volume-based metrics	Surface-based metrics
Max Dose ($D_{max,V}$)	Max Dose ($D_{max,SA}$)
Mean Dose ($D_{mean,V}$)	Mean Dose ($D_{mean,SA}$)
V_5	SA_5
V_{15}	SA_{15}
V_{25}	SA_{25}
V_{35}	SA_{35}
V_{45}	SA_{45}
V_{55}	SA_{55}

Table 4.1: Summary of dose-volume and dose-surface metrics extracted for patients in both clinical trials (ARCII and SCALOP). The V_X and SA_X metrics were extracted in absolute (mm^3/mm^2) and relative (%) terms. These metrics were extracted for the stomach and duodenum.

distribution. Receiver-operating characteristic (ROC) curves were plotted to find the area under the ROC curve (AUC) in order to quantify the predictive power of each significant metric. An ROC curve plots the true positive rate for different metric thresholds (or cut-off points) against the false positive rate. An AUC closer to the maximum value of 1 indicates the metric can classify patients by toxicity with greater accuracy.

4.2.5 Spatial Dose Metrics

A new spatial feature was extracted from the dose-surface maps. This metric is the percentage of the length of the organ that receives less than a certain threshold dose to at least a certain threshold circumference of the organ. An example of this is seen in Figure 4.1 where the dose and circumference thresholds are set to 45 Gy and 10% respectively. With this example the length of the organ over which at least 10% of the circumference receives less than 45 Gy is recorded (33%).

For both the duodenum and stomach dose-surface maps, the length over which at least 10, 20, 30, 40, 50, 60, 70, 80, and 90% of the circumference of the organ receives

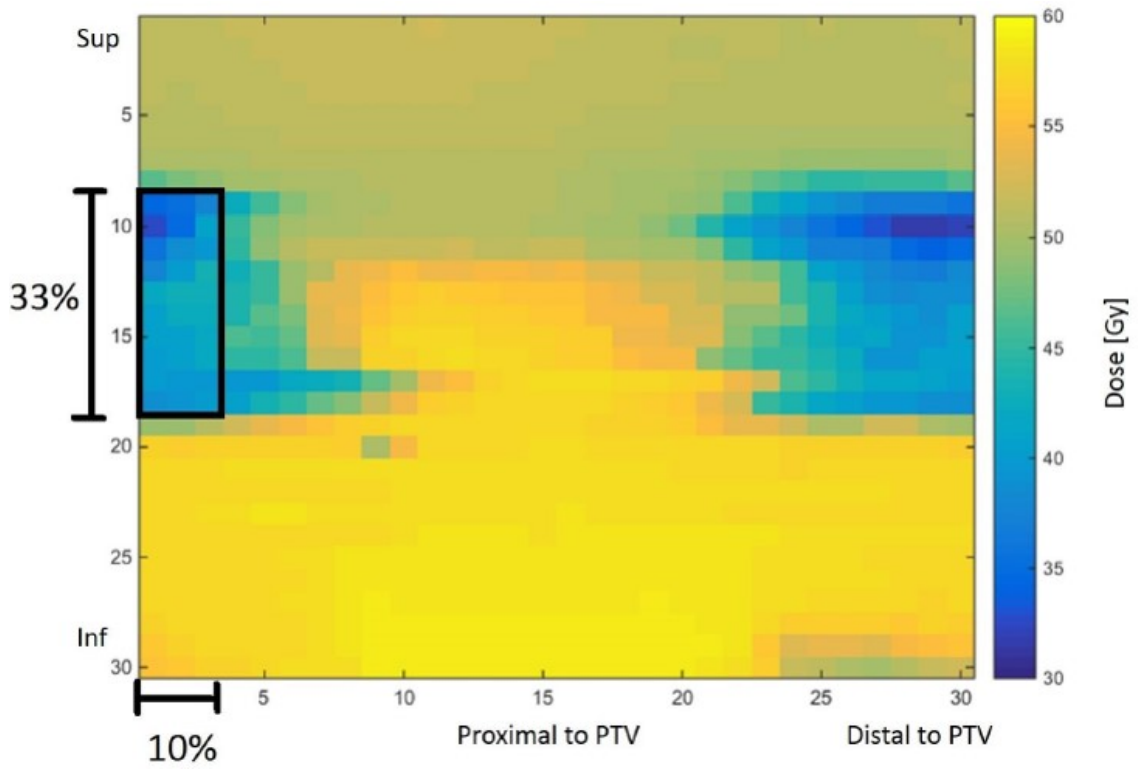


Figure 4.1: Spatial features such as the length of an organ where at least Y% of the circumference receives less than X Gy can be found from the dose-surface maps. In this example figure, 33% of the length of the duodenum receives less than 45 Gy to at least 10% of the circumference of the organ.

less than 5, 15, 25, 35, 45, 55 Gy is recorded. Once again, univariate analysis using the Wilcoxon rank-sum test was used to find significant parameters in predicting grade $\geqslant 2$ and grade $\geqslant 3$ UGIT. ROC curves were plotted to find the area under the ROC curve (AUC) to quantify the predictive power of each significant metric.

4.2.6 Population Dose-Surface Map Analysis

The mean dose at each pixel in the dose-surface maps was calculated for the duodenum and stomach. The patients in each trial were then split into those with and without grade $\geqslant 2$ and grade $\geqslant 3$ toxicity and the mean dose at each pixel was recalculated for the different groups. These grades were chosen because at these stages toxicity can

begin to impact treatment. A dose difference map was also produced by subtracting the mean dose-surface map for the group without toxicity from that of the group with toxicity.

4.2.7 Region-of-interest Metrics

4.2.7.1 Permutation Test

Each dose-surface map has an associated upper GI toxicity grade in the range [0, 5] as determined in follow up. As an illustrative example, four 5 x 5 DSMs (as a simplification of the 30 x 30 DSMs produced from real data) are shown in Figure 4.2 with associated toxicity.

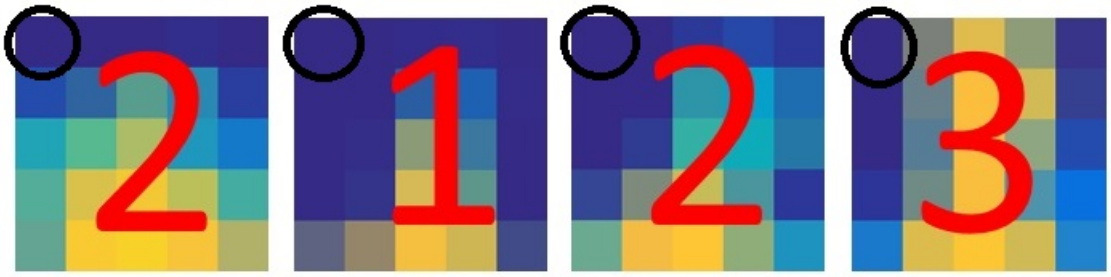


Figure 4.2: Four 5 x 5 DSMs with their associated toxicities labelled in red. Circled pixel illustrates that a statistical test is applied to the same pixel in each DSM.

For each of the 900 pixels (30 x 30) in the duodenal and stomach DSMs, the true Kendall's tau-b correlation coefficient was computed using dose at that pixel and the true toxicity grade (Figure 4.3, left panel). Kendall's tau-b is a non-parametric measure of the strength of association between two variables measured on at least an ordinal scale (dose is continuous, toxicity is ordinal). Kendall's tau-b was chosen over a Spearman rank-order correlation coefficient due to the small sample size in the clinical trials.

The toxicity labels were then permuted 10,000 times and each time a permuted tau-b coefficient is calculated. The position of the true tau-b coefficient within the distribution of permuted coefficients is used to calculate an uncorrected p-value for each pixel, as illustrated in Figure 4.3.

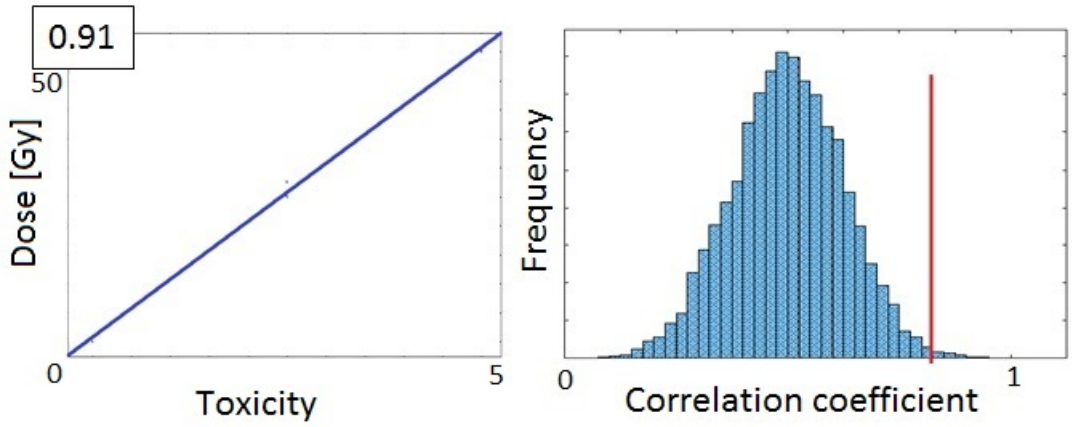


Figure 4.3: Left: True Kendall's tau-b correlation coefficient for the true dose-toxicity association. Right: The position of the true tau-b (red line) within the distribution of permuted tau-b (histogram bars) defined the p-value for a single pixel.

This p-value is considered uncorrected due to the multiple comparison problem of simultaneously testing multiple pixels to one outcome. The decision not to correct for multiple comparisons was taken because significance of the single pixel was not as important as the significance of the metric extracted from the region described by multiple pixels. While there are various methods to account for multiple comparisons, there is also no agreed approach for the best method for correction for this type of analysis [40].

4.2.7.2 Extracting Region-of-interest Metrics

Pixels with uncorrected p-values lower than 0.2 were selected as regions of interest (ROIs) and the mean ($D_{mean,ROI}$) and maximum dose ($D_{max,ROI}$) at those pixels

were recorded for each patient. The value of 0.2 is an arbitrary choice which simply helps identify more predictive regions rather than identify individual pixels which are statistically significant. The metrics extracted from these regions will be referred to as region-of-interest (ROI) metrics. To quantify the predictive power of these metrics, the area under the ROC curve (AUC) was calculated based on the ability to correctly predict toxicity in each patient. Univariate analysis using the Wilcoxon rank-sum test was also performed on the ROI metrics.

The number of pixels in the ROI from which the mean and maximum dose are calculated represent a subset of pixels from the whole dose-surface map. To ensure that any improvement in predictive power is not an artefact of the smaller number of pixels, 100 random combinations of the same number of pixels were also produced and the same metrics calculated. The predictive power of these random combinations was compared to metrics calculated on the pixels in the region-of-interest.

4.3 Results

The reported incidence of grade $\geqslant 2$ toxicity in each trial is 10/19 (53%) for ARCII and 24/62 (39%) for SCALOP. ARCII had 3/19 (16%) patients with grade $\geqslant 3$ toxicity and SCALOP had 7/62 (11%).

4.3.1 Traditional Dose Metrics

The mean (and range) dose-volume and dose-surface metrics that were extracted from the stomach and duodenum are shown in Table 4.2 and Table 4.3 respectively. No volume or surface metric from the duodenum or stomach was significant in differen-

Volume Metrics		
Metric	ARCII	SCALOP
$D_{max,V}$	59.2 (45.7-62.6)	58.3 (5.7-54.3)
$D_{mean,V}$	20.2 (9.2-42.1)	13.3 (0.6-37.3)
V_5	65 (25-100)	47 (0-99)
V_{15}	49 (20-97)	36 (0-93)
V_{25}	36 (15-89)	28 (0-87)
V_{35}	24 (8-73)	12 (0-55)
V_{45}	15 (1-42)	8 (0-44)
V_{55}	7 (0-29)	0 (0-0)
Surface Metrics		
Metric	ARCII	SCALOP
$D_{max,SA}$	58.9 (45.6-62.1)	46.8 (5.5-53.7)
$D_{mean,SA}$	25.6 (9.4-41.3)	16.8 (1.4-39.8)
SA_5	75 (32-97)	57 (0-99)
SA_{15}	61 (21-92)	47 (0-97)
SA_{25}	49 (10-90)	40 (0-95)
SA_{35}	37 (5-83)	22 (0-69)
SA_{45}	25 (2-59)	15 (0-63)
SA_{55}	15 (0-40)	-

Table 4.2: Summary of stomach dose-volume and dose-surface metrics (mean and range) that are extracted from the ARCII and SCALOP datasets.

tiating SCALOP patients for either grade $\geqslant 2$ or grade $\geqslant 3$ toxicity. None of the stomach or duodenum surface metrics were significant in ARCII when considering grade $\geqslant 3$ toxicity. Note that both V_{55} and SA_{55} were not analysed for SCALOP patients as this was above the prescription dose and therefore had no variation among patients.

4.3.1.1 Stomach

Mean dose to the volume of the stomach ($D_{mean,V}$), absolute stomach volume receiving at least 25 and 35 Gy, and the percentage of the stomach volume receiving at least 5, 15, 25, 35, and 45 Gy were all significantly different (Wilcoxon rank-sum, $p < 0.05$) in groups with and without grade $\geqslant 2$ toxicity in ARCII patients. The stomach mean

Volume Metrics		
Metric	ARCII	SCALOP
$D_{max,V}$	59.7 (45.5-63.5)	51.3 (39.7-53.8)
$D_{mean,V}$	49.7 (29.2-57.0)	34.9 (8.5-50.1)
V_5	99 (92-100)	86 (15-100)
V_{15}	98 (84-100)	80 (8-100)
V_{25}	96 (77-100)	74 (6-100)
V_{35}	88 (17-100)	60 (3-100)
V_{45}	75 (2-96)	48 (0-100)
V_{55}	39 (0-75)	
Surface Metrics		
Metric	ARCII	SCALOP
$D_{max,SA}$	59.3 (45.3-63.5)	49.3 (34.9-53.4)
$D_{mean,SA}$	51.6 (27.0-60.4)	38.1 (7.3-50.7)
SA_5	99 (84-100)	89 (28-100)
SA_{15}	97 (65-100)	85 (19-100)
SA_{25}	96 (56-100)	81 (10-100)
SA_{35}	91 (29-100)	67 (0-100)
SA_{45}	80 (2-100)	43 (0-100)
SA_{55}	48 (0-98)	-

Table 4.3: Summary of duodenum dose-volume and dose-surface metrics (mean and range) that are extracted from the ARCII and SCALOP datasets.

surface dose ($D_{mean,SA}$), SA_{45} (abs), SA_{15}, SA_{25}, SA_{35}, and SA_{45} were the significant surface metrics in differentiating between these patients (grade $\geqslant$ 2, ARCII). The mean value of the statistically significant stomach metrics for the groups with and without toxicity are reported with their p-values in Table 4.4 along with the area under the ROC curve (AUC).

4.3.1.2 Duodenum

The percentage of the duodenum volume receiving at least 45 Gy was significant (p=0.05) in differentiating grade $\geqslant$ 3 toxicity in ARCII patients. The area under the ROC curve was 0.88 but this represented an inverse relationship between V45 and toxicity. This was the only duodenal volume or surface metric that was significant in

Stomach Metrics Predictive of Grade $\geqslant$ 2 UGIT									
Volume					Surface				
Metric	T	NT	p	AUC	Metric	T	NT	p	AUC
$D_{mean,V}$	23.4	15.7	0.02	0.82	$D_{mean,SA}$	29.4	20.5	<0.01	0.90
V_{25} (abs)	145.0	85.6	0.04	0.78	SA_{45} (abs)	115.5	67.0	0.02	0.82
V_{35} (abs)	102.1	46.6	0.02	0.81	SA_{15}	68	52	0.04	0.78
V_5	71	58	0.04	0.78	SA_{25}	57	38	0.03	0.80
V_{15}	57	38	0.01	0.85	SA_{35}	46	25	0.01	0.86
V_{25}	44	26	0.02	0.81	SA_{45}	31	17	<0.01	0.88
V_{35}	31	15	0.01	0.85					
V_{45}	18	10	0.04	0.78					

Table 4.4: Summary of stomach dose-volume and dose-surface metrics that are significant in predicting grade $\geqslant$ 2 UGIT in ARCII patients. The mean value for each metric for patients who had grade $\geqslant$ 2 UGIT (T), and those who didn't (NT) are presented together with the p-value calculated with a Wilcoxon rank-sum test (p) and the area under the ROC curve (ROC).

either of the datasets.

4.3.2 Spatial Dose Metrics

The 54 different combinations of dose and circumference thresholds (described in Section 4.2.5) were extracted from the stomach and duodenal dose-surface maps. The dose threshold of 55 Gy was not analysed for SCALOP patients as this was above the prescription and therefore had no variation among patients. This left 45 metrics in the SCALOP analysis. For all metrics that had a p-value of less than 0.05 in univariate analysis, the area under the ROC curve was calculated. The AUC for the duodenal metrics predicting grade $\geqslant$ 3 UGIT in ARCII patients is shown in Table 4.5, and again this represents an inverse relationship. The stomach metrics predicting grade $\geqslant$ 2 UGIT in ARCII patients is shown in Table 4.6 and those predicting grade $\geqslant$ 3 UGIT in SCALOP patients in Table 4.7.

		Percentage of circumference spared [%]								
		10	20	30	40	50	60	70	80	90
Dose [Gy]	5	-	-	-	-	-	-	-	-	-
	15	-	-	-	-	-	-	-	-	-
	25	-	-	-	-	-	-	-	-	-
	35	-	-	-	-	-	-	-	-	-
	45	-	-	-	-	-	-	-	0.81	0.82
	55	-	-	-	-	-	-	-	-	-

Table 4.5: Area under the ROC curve (AUC) of duodenal spatial metrics that are significant in predicting grade $\geqslant 3$ UGIT in ARCII patients. This AUC represents an inverse relationship.

		Percentage of circumference spared [%]								
		10	20	30	40	50	60	70	80	90
Dose [Gy]	5	-	-	-	-	0.84	0.80	-	-	
	15	-	-	-	0.78	0.78	0.88	0.87	0.89	0.81
	25	-	-	-	-	0.77	0.79	0.86	0.86	0.86
	35	-	0.79	0.78		0.83	0.84	0.91	0.89	0.89
	45	-	-	-	-	-	0.80	0.83	0.87	0.87
	55	-	-	-	-	-	0.77	0.83	0.78	0.79

Table 4.6: Area under the ROC curve (AUC) of stomach spatial metrics that are significant in predicting grade $\geqslant 2$ UGIT in ARCII patients.

		Percentage of circumference spared [%]								
		10	20	30	40	50	60	70	80	90
Dose [Gy]	5	-	-	-	-	-	-	-	-	-
	15	-	-	-	-	-	-	-	-	-
	25	-	-	-	-	-	-	-	-	-
	35	-	0.71	0.71	-	-	-	-	-	-
	45	0.65	0.65	0.70	-	-	-	-	-	-

Table 4.7: Area under the ROC curve (AUC) of stomach spatial metrics that are significant in predicting grade $\geqslant 3$ UGIT in SCALOP patients.

4.3.3 Population Dose-Surface Map Analysis

The mean dose-surface map for both ARCII and SCALOP patients is shown for the duodenum and stomach in the first row of Figures 4.4 and 4.5 respectively. The mean DSMs for patients with and without grade $\geqslant 2$ and grade $\geqslant 3$ toxicity are also shown, along with a dose difference map.

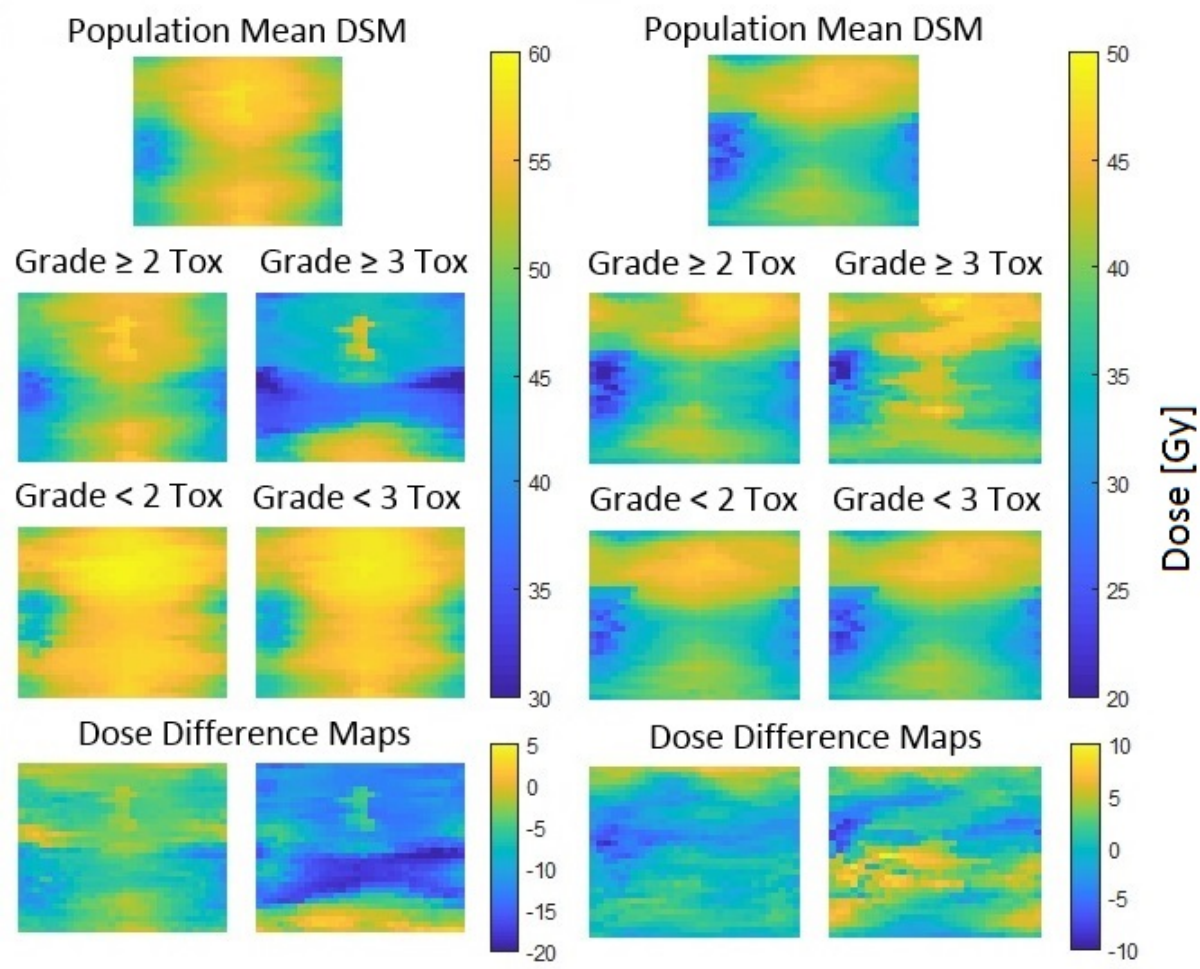


Figure 4.4: Duodenal population dose-surface maps. ARCII data is shown on the left, with corresponding SCALOP data on the right. Top row: Mean dose-surface map. Second row: Mean DSM for patients with grade $\geqslant 2$ and grade $\geqslant 3$ toxicity. Third row: Mean DSM for patients with grade < 2 and grade < 3 toxicity. Final row: Dose difference maps showing the difference in maps with and without toxicity. Dose colour wash scale in Gy.

Both duodenal and stomach mean dose in the DSMs are higher for ARCII patients than SCALOP patients. In the duodenum, the dose difference maps indicate smaller differences between DSMs of patients with and without toxicity than in the stomach for both grade $\geqslant 2$ and grade $\geqslant 3$.

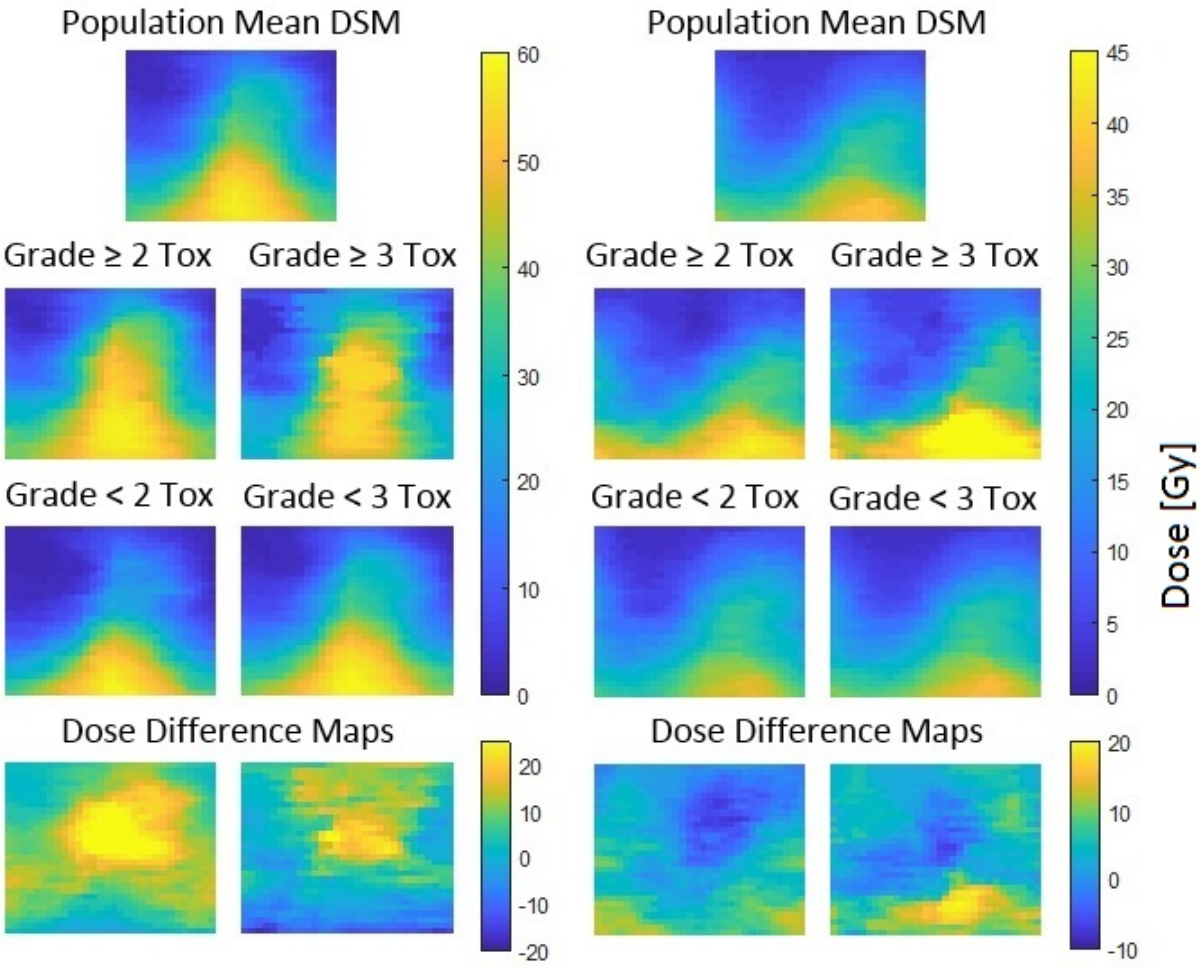


Figure 4.5: Stomach population dose-surface maps. ARCII data is shown on the left, with corresponding SCALOP data on the right. Top row: Mean dose-surface map. Second row: Mean DSM for patients with grade $\geqslant 2$ and grade $\geqslant 3$ toxicity. Third row: Mean DSM for patients with grade < 2 and grade < 3 toxicity. Final row: Dose difference maps showing the difference in maps with and without toxicity. Dose colour wash scale in Gy.

4.3.4 Region-of-interest Metrics

The dose at each pixel of the dose-surface map was tested for correlation to toxicity using the permutation test and the uncorrected p-values for each pixel were found.

There were no pixels with $p < 0.2$ in the ARCII or SCALOP duodenal maps. For the stomach, the p-value map is shown in Figure 4.6 and pixels with $p < 0.2$ are

highlighted in Figure 4.7.

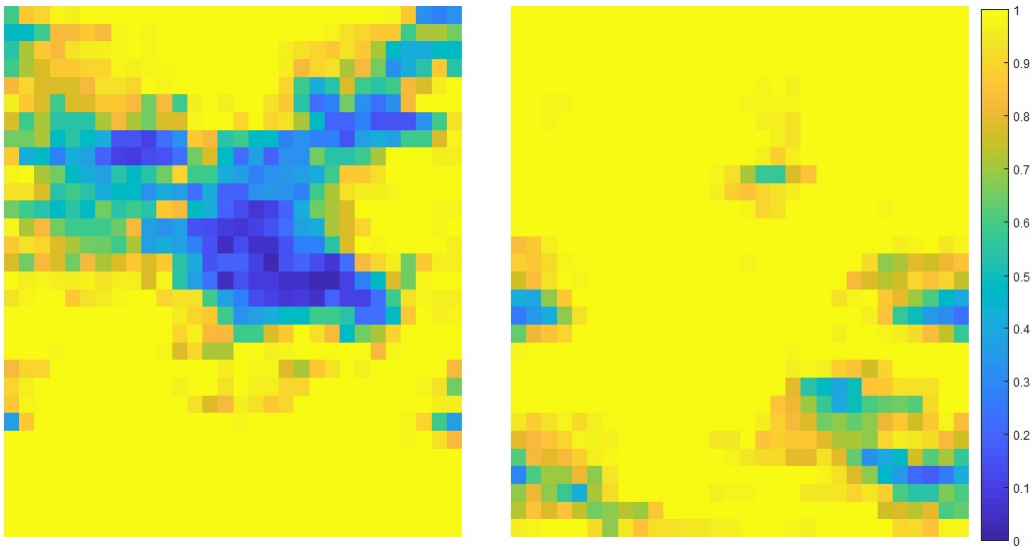


Figure 4.6: Heat map showing p-values in the stomach dose-surface map. ARCII shown on left and SCALOP on right.

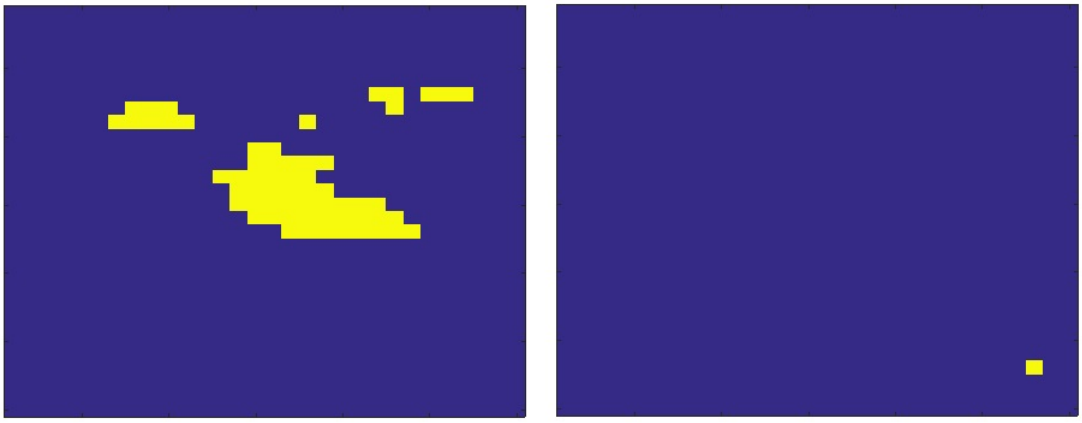


Figure 4.7: Map showing pixels in the stomach dose-surface map with a p-value (calculated using a permutation test) < 0.2 in yellow. ARCII shown on left and SCALOP on right.

The AUC and Wilcoxon rank-sum test p-values for V_{15}, V_{35}, $D_{mean,SA}$, and SA_{45} which had the largest AUC reported in Table 4.4 out of the metrics significant in differentiating patients with and without toxicity grade $\geqslant 2$ for ARCII patients, are also listed in Table 4.8 as a comparison with the new region-of interest metrics. The

AUCs for each metric are plotted in Figure 4.8.

		Stomach			
		Grade $\geqslant$ 2		Grade $\geqslant$ 3	
		AUC	p	AUC	p
ARCII	$\mathbf{D}_{mean,ROI}$	**0.97**	**<0.01**	0.83	0.08
	$\mathbf{D}_{mean,SA}$	**0.90**	**<0.01**	0.63	0.56
	$\mathbf{SA}_{45}$	**0.88**	**<0.01**	0.54	0.88
	$\mathbf{V}_{15}$	**0.85**	**0.01**	0.48	0.96
	$\mathbf{V}_{35}$	**0.85**	**0.01**	0.54	0.85
SCALOP	$\mathbf{D}_{mean,ROI}$	**0.71**	**<0.01**	**0.74**	**0.04**
	$\mathbf{D}_{mean,SA}$	0.56	0.41	0.61	0.34
	$\mathbf{SA}_{45}$	0.58	0.27	0.72	0.06
	$\mathbf{V}_{15}$	0.50	0.99	0.60	0.41
	$\mathbf{V}_{35}$	0.60	0.19	0.71	0.07

Table 4.8: Comparison of the best (highest AUC) stomach dose-volume and dose-surface metrics that are significant in predicting grade $\geqslant$ 2 UGIT in ARCII patients to the predictive power of new region-of-interest metrics.

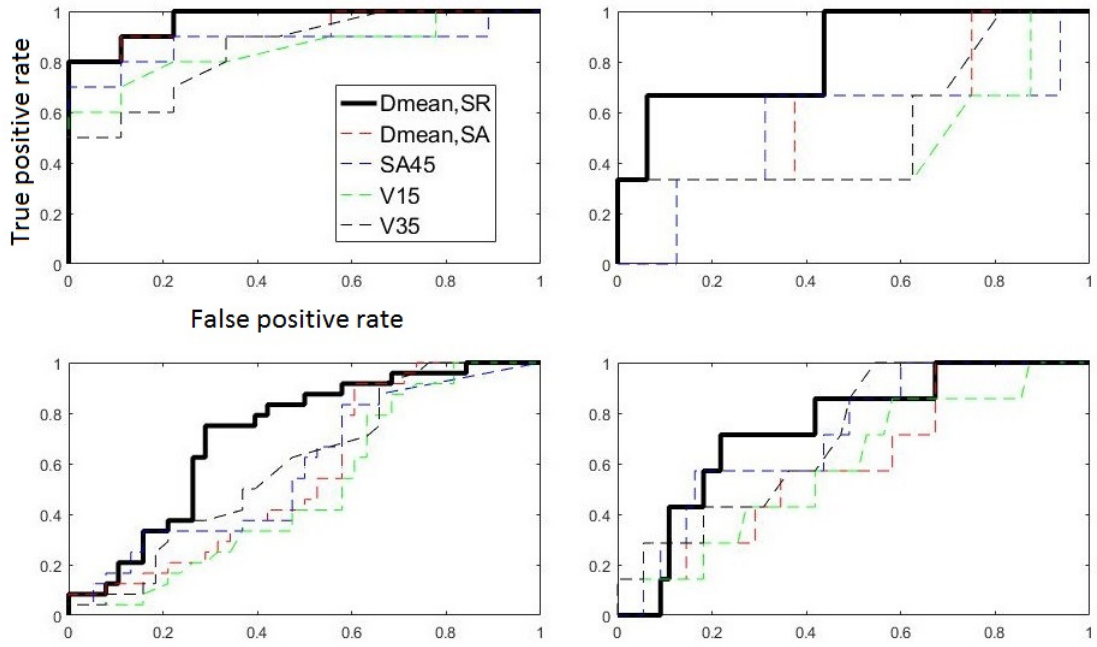


Figure 4.8: Area under the ROC curve for region-of-interest metric ($D_{mean,ROI}$), dose-surface metrics ($D_{mean,SA}$ and SA_{45}), and dose-volume metrics (V_{15} and V_{35}). Top left: Predicting grade $\geqslant$ 2 toxicity in ARCII patients. Top right: Predicting grade $\geqslant$ 3 toxicity in ARCII patients. Bottom left: Predicting grade $\geqslant$ 2 toxicity in SCALOP patients. Bottom right: Predicting grade $\geqslant$ 3 toxicity in SCALOP patients.

The AUC for the mean dose in the region-of-interest ($D_{mean,ROI}$) is 0.97 and 0.83 for predicting grade $\geqslant 2$ and grade $\geqslant 3$ respectively in ARCII patients. For SCALOP it is 0.71 for grade $\geqslant 2$ and grade $\geqslant 3$. $D_{mean,ROI}$ is the only metric that is significant (Wilcoxon rank-sum, $p < 0.05$) in predicting both grade $\geqslant 2$ and grade $\geqslant 3$ toxicity in SCALOP patients. All metrics are significant in predicting grade $\geqslant 2$ toxicity in ARCII patients and none are significant in predicting grade $\geqslant 3$ toxicity. In all cases, the AUC for $D_{mean,ROI}$ is higher than for all other metrics.

For ARCII patients, the number of pixels in the region-of-interest was 60, and for SCALOP this number was 1. These same number of pixels were selected randomly 100 times and the mean dose in those pixels calculated. The average AUC for these random selections for grade $\geqslant 2$ is 0.88 and 0.53 for ARCII and SCALOP, and 0.60 and 0.57 for grade $\geqslant 3$. These AUCs are all much lower than the AUC for the pixels in the region-of-interest.

4.4 Discussion

The QUANTEC [19] review released in 2009 aimed to summarise the available dose-response data in the field and to update the clinical recommendations made in the Emami paper in 1991 [18]. QUANTEC directly addresses limitations of current predictive models by stating that 'DVHs are not ideal representations of the 3D doses as they discard all organ-specific spatial information (and hence assume all regions are of equal functional importance)' [19]. This statement is true of all organs, but perhaps even more relevant for the hollow organs in the gastrointestinal tract that surround the pancreas.

There have been several studies, the majority retrospective, that attempt to link dosimetric parameters to gastrointestinal toxicity in locally-advanced pancreatic cancer but all do so by considering dose-volume data [7, 21, 23, 22]. In all these studies, dose-volume metrics for a few organs at risk are extracted and their correlation with various toxicity endpoints are reported. The heterogeneous patient population with respect to chemotherapy agent across these studies and the lack of dose-response consensus has resulted in a lack of understanding of gastrointestinal toxicity.

The work in this chapter represents an initial attempt to identify a correlation between the spatial distribution of dose on the organ surface and upper gastrointestinal toxicity. To our knowledge, correlation between spatial surface dose distributions in the stomach and duodenum have not been previously studied. The analysis in this paper uses prospectively collected data from two clinical trials.

4.4.1 Duodenum

In this dataset dose-volume, dose-surface, spatial, and pixel-based analysis all had no statistically significant correlation between dose to the duodenum and grade $\geqslant$ 2 UGIT. Only one dose-volume and two spatial dose metrics found a statistically significant correlation between dose to the duodenum and grade $\geqslant$ 3 toxicity.

These three metrics indicate an inverse relationship between dose and toxicity which means that for the dose-volume metric, it is found that an increase in the duodenal volume receiving at least 45 Gy reduces the chance of toxicity. It is also found that as the length of the duodenum over which at least 80% or 90% of the circumference receives less than 45 Gy increases, there is again a reduced risk of

grade $\geqslant$ 3 toxicity. Both these results are counter-intuitive and both occur when predicting grade $\geqslant$ 3 toxicity in the ARCII dataset.

However, only 3 out of the 19 ARCII patients had grade $\geqslant$ 3 toxicity which is too small a sample on which to build a meaningful dose-toxicity model. Taking a closer look at these 3 patients with grade $\geqslant$ 3 toxicity shows that 2 of these patients have very low dose duodenal DSMs (lowest and 3rd lowest mean doses of ARCII). This could mean that other factors apart from radiation could have contributed to their increased toxicity.

4.4.2 Stomach

While most groups have reported correlation between duodenal dose-volume metrics and toxicity, a previous study using endoscopy to identify gastric and duodenal ulcers found that 21% of a cohort of 58 patients (treated for unresectable pancreatic cancer with carbon ion therapy) had gastric ulcers but there were no reported duodenal ulcers [72]. While it is not completely fair to compare the outcome of carbon ion therapy to photon therapy, a second group (treating locally advanced pancreatic cancer with photon therapy) reported 45 cases of grade 0 and 14 cases of grades 1-2 gastroduodenal ulcers in a cohort of 84 patients [83]. These two studies support the results found in this chapter, namely that correlation between stomach dose and toxicity may be of more interest than the correlation with duodenal dose.

In this study a significant correlation between dose and toxicity is found in the stomach. Using stomach dose-volume and dose-surface metrics alone resulted in significant correlation between most of the dose metrics examined and grade $\geqslant$ 2 toxicity

only in ARCII patients. As shown in Table 4.4, the dose-volume metrics had AUCs between 0.78-0.85 and the dose-surface metrics had AUCs between 0.78-0.90. A direct comparison between the mean dose to the whole volume (AUC = 0.82) and to the surface (AUC = 0.90) shows a slight improvement in ability to predict toxicity.

The stomach spatial metrics, which indicate the length of the stomach over which a threshold circumference is spared a threshold dose, offer new metrics which incorporate spatial information and are predictive of grade $\geqslant 2$ toxicity in the ARCII dataset (AUC = 0.77 - 0.91) and of grade $\geqslant 3$ toxicity in the SCALOP dataset (AUC = 0.65 - 0.71). In both cases the best predictors appeared when limiting dose to less than 35 Gy but in the ARCII dataset this needed to be limited over at least 70% of the circumference (Table 4.6) whereas in SCALOP it only needed to be limited over at least 20% or 30% (Table 4.7).

Once again, due to the limited number of patients with grade $\geqslant 3$ toxicity (7/62 in SCALOP), not much weight should be placed on this particular result. For grade $\geqslant 2$ toxicity, the significant stomach spatial metrics in the ARCII dataset (Table 4.6) have comparable AUCs to the significant dose-volume and dose-surface metrics seen in Table 4.2.

4.4.3 Stomach Region-of-interest Metrics

The AUC for the region-of-interest (ROI) metric is higher than volume and surface metrics in both trials and for predicting grade $\geqslant 2$ and grade $\geqslant 3$ toxicity (Figure 4.8). The ROI metric is the only metric that is significant (Wilcoxon rank-sum, $p < 0.05$) in predicting both grade $\geqslant 2$ and grade $\geqslant 3$ toxicity in SCALOP patients.

To rule out the possibility that the better predictive power of ROI metrics in the stomach is a statistical artefact of the small number of pixels, 100 groups of randomly selected pixels (60 pixels for ARCII, and 1 pixel for SCALOP) were also selected as a comparison and shown not to improve the AUC.

Another element which could warrant further investigation is the non-contiguous nature of the region-of-interest in ARCII and whether forcing a contiguous region will improve predictive power.

4.4.4 Statistical Discussion

Even though the improved predictive power was shown not to be random, the AUCs of the ROI metrics are inflated due to overfitting. To remove this overfitting, the p-value map could be created using cross-validation, where some of the data is withheld while the region-of-interest ($p < 0.2$) is calculated. The ROI metric could then be extracted from the withheld data and the predictive power assessed.

Another alternative statistical approach would be to report corrected p-values with a method using a maximally selected test statistic as outlined by Chen et al [84]. However, since the extracted metric from the region-of-interest is tested for statistical significance, the exact significance of each pixel is not of great importance.

4.4.5 Clinical Translation

Since the locations of the region-of-interest found on the two clinical trials are different, it is difficult to translate the improvement in toxicity prediction into more general clinical constraints. Additionally, the definition of a single pixel ROI limits the meaning of the results of the ROI metrics in the SCALOP dataset and means

further work is needed to develop spatial dose-toxicity models that inform clinical decisions.

4.4.6 Further Limitations

The small sample size available and the different types of concomitant chemotherapy are a major limitation in this study. Additionally, while the smaller ARCII cohort had a slightly higher dose than the larger SCALOP cohort, both had relatively low dose to the stomach and duodenum and therefore also low incidence of toxicity. These factors may have contributed to the inability to find significant duodenal metrics or generalisable clinical constraints, and the small significant region in the SCALOP dataset. With higher dose prescriptions and tighter margins in more modern treatments that are becoming a standard of care, this type of analysis may need to be revisited. In addition, incorporating this analysis in cohorts that receive post-treatment endoscopy to identify ulcers could help correlate the location of dose hotspots to mucosal damage.

4.5 Conclusion

In this chapter, the information found in dose-surface maps created in chapters 2 and 3 for the duodenum and stomach respectively was correlated to toxicity using data from two clinical trials in an exploratory study. Spatial metrics extracted from these DSMs were compared to traditional dose-volume and dose-surface metrics and were found to offer comparable predictive power in predicting grade $\geqslant 2$ upper gastrointestinal toxicity in the ARCII dataset. Region-of-interest metrics were defined and extracted from the DSMs and found to offer better predictive power for grade $\geqslant 2$ toxicity in

the ARCII dataset. Strong conclusions cannot be made regarding the prediction of grade $\geqslant 3$ toxicity in either trial to its low incidence.

Chapter 5

Interfraction Duodenal Changes

In this chapter, the interfraction changes in the duodenum are quantified using daily CBCT images in patients treated with and without abdominal compression for motion management. The unwrapping methodology from chapter 2 is used to create dose-surface maps for the CBCT duodenum contours. In order to investigate differences between planned and delivered dose, these DSMs are used to build accumulated dose-surface maps and compared to planning dose-surface maps.

5.1 Introduction

All the toxicity correlation work in this thesis so far has been utilising the dose distribution calculated on the planning CT. However, this may not be an accurate representation of the final dose distribution. As described in Section 1.4, a radiotherapy patient is first scanned on a CT approximately a week before treatment starts and their treatment plan is made using this scan. On the days of treatment delivery, the patient is set up on the treatment couch in the same position as on the planning CT. This is done in order to minimise differences between the planned dose and the delivered dose to the patient.

However, other changes that are harder to control can occur in the patient anatomy between the planning CT and daily treatment. These include (but are not limited to) weight loss, and tumour or organ changes. Physiological motion (respiration, peristalsis, distention) can cause changes to the tumour or healthy organs which is especially important when considering abdominal and thoracic treatment sites. These anatomical differences are considered the main causes of intrafraction changes. Tumour change, weight loss/gain, hollow organ filling, and patient positioning errors also contribute to interfraction changes.

Many studies have shown that the pancreas suffers from interfraction changes (Section 1.9) and that the interfraction changes of the duodenum have a dosimetric impact on the treatment plan [51, 56]. In order to account for interfraction changes, on board imaging can be used to take a cone-beam CT (CBCT) of the patient each day when they are positioned on the couch. While the patient is not replanned using this CBCT, it is possible to register this image onto the planning CT and retrospectively calculate the dose to the daily anatomy. By accumulating the dose on the daily CBCTs, a delivered dose can be calculated and compared to the planned dose.

In recent rectal toxicity studies it has been shown that accumulated rectum dose-surface maps are different to dose-surface maps created from the planning CT [35] and that features from these accumulated-DSMs can better predict toxicity [36]. Now that DSMs of the duodenum have been produced, a similar analysis can be performed. With new advances in technology bringing MR-Linacs to the clinic and the availability of high quality daily imaging for such treatments, work is already under way to use MR imaging information for adaptive planning in pancreatic radiotherapy [55].

In this chapter, we preliminarily quantify the motion and dosimetric impact of interfraction duodenal changes in patients treated with and without the use of abdominal compression as a method of motion management. We also utilise the psuedoregistration created by the methodology described in Chapter 2 to calculate accumulated dose-surface maps for these patients and compare them to the planning dose-surface maps.

5.2 Materials & Methods

5.2.1 Patient Cohort

Eight patients treated for pancreatic cancer were selected for analysis. Five patients were treated with abdominal compression and three without. The three patients treated without abdominal compression were randomly selected from the ARCII dataset [57]. These patients received 59.4 Gy in 33 fractions (including boost) and this dataset is described in more detail in Section 2.2.1. Table 5.1 describes the dose regime for the abdominal compression patients.

Patient	**Prescription [Gy]**	**Number of Fractions**
1	50	10
2	40	10
3	60	30
4	54	30
5	45	5

Table 5.1: Summary of prescription and fractionation schedule for the five abdominal compression patients chosen.

5.2.2 Quantifying Interfraction Changes

The duodenum was contoured by the same physician on each CBCT (five CBCTs for patients with compression, four for non-compression patients). This was done to simulate the number of fractions in a SABR treatment since interfraction motion will have a larger impact in these treatments. CBCTs were rigidly registered using a soft tissue match and contours were copied to the delivered plans which had a biological equivalent dose greater than 50 Gy. All CBCTs were visually assessed to confirm inclusion of entire duodenum.

The difference in volume between the planning CT duodenum contour and the CBCT contour was calculated. The distance between the duodenum on the planning CT and each CBCT was quantified in two ways. First, by the displacement of the centre of mass (COM) of the duodenum and second, by calculating the modified Hausdorff distance (MHD) [85]. The DVHs of each patient was converted to a DVH of an equivalent dose in 2 Gy fractions (EQD2) using an alpha/beta ratio of 10 (as a representative value for acute toxicity in normal tissue). Volumes receiving at least 25, 35, 45, and 50 Gy were recorded for patients from both the compressed and non-compressed cohort. EQD2 rather than absolute dose is only used for the analysis in this section.

5.2.3 Dose Surface Maps for Dose Accumulation

Dose-surface maps were produced from the planning CT contour and each CBCT contour for 8 patients (5 with and 3 without abdominal compression). The unwrapping methodology defined in Chapter 2 was used.

The planning CT dose-surface map was scaled to 5 or 4 fractions to represent a SABR treatment depending on the number of CBCT contours available (5 for compressed, 4 for non-compressed). The dose-surface maps of each CBCT duodenum contour were added together to form an accumulated-DSM. The pseudoregistration of the unwrapping technique (Chapter 2) means that the top of the DSM is defined as the most superior part of the duodenum for every patient and each pixel horizontally on the DSM represents the same fraction of the whole circumference of each duodenum. For this reason, a simple addition of the dose-surface maps was used.

Surface map metrics that follow the same definition as their volume counterparts were extracted from the planned and accumulated dose-surface maps. These were the percentage of surface map pixels that receive at least 10% (SM_{10}), 30%, 50%, 70%, and 90% of the maximum dose of that map. A percentage of maximum dose was chosen because of the different fractionation schedules between patients. Using the same gamma metric that was described in Section 2.2.3.1, the differences between the planned-DSM and accumulated-DSM were quantified.

5.3 Results

5.3.1 Quantifying Interfraction Changes

The volume of the duodenum on the planning CT and the range of duodenal volumes on the CBCTs were 58.3 cm^3 (57.5-76.6), 92.5 cm^3 (88.6-107.7), 139.00 cm^3 (120.3-140.2), 47.2 cm^3 (47.0-59.9), and 52.1 cm^3 (66.9-102.9) for patients with abdominal compression. For the non-compressed patients the volumes and ranges were 87.3 cm^3 (57.9-73.1), 42.6 cm^3 (46.7-80.9), and 94.0 cm^3 (77.9-133.8). These results are shown

in Figure 5.1.

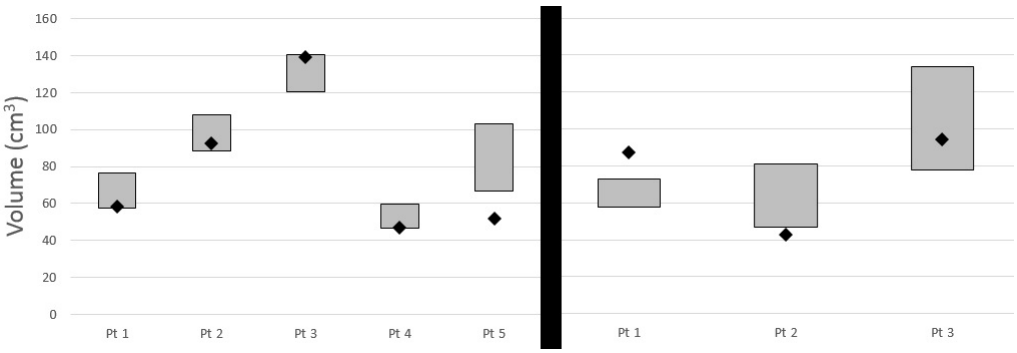


Figure 5.1: Volume of duodenum in cm^3 on planning CT marked in solid black diamond and the range of volumes from CBCTs marked as a box for each abdominal compression (left) and non-compressed (right) patient.

The maximum variation in duodenal volumes on the CBCTs for the four abdominal compression patients were 19.1 cm^3 (32.8%), 19.1 cm^3 (20.6%), 19.9 cm^3 (14.3%), 12.9 cm^3 (27.3%), and 36.0 cm^3 (69.1%) compared to 15.2 cm^3 (17.6%), 34.2 cm^3 (80.3%), and 55.9 cm^3 (59.5%) for non-compression patients. The average maximum variation was 21.4 cm^3 for the abdominal compression patients and 35.1 cm^3 for the non-compressed patients.

In the abdominal compression patients the volume of the duodenum in the planning CT falls within the range of the CBCT duodenal volumes in four of the five patients. However, in one out of 5 abdominal compression patients and two out of the three non-compression patients, the duodenum contoured in the planning CT falls outside the CBCT range. If the volume from the planning CT is included in the volume range, the range increases to 50.8 cm^3 (97.5%) for the abdominal compression patient and 29.4 cm^3 (33.7%) and 38.3 cm^3 (89.9%) for the non-compressed patients.

The average displacement of the centre of mass (COM) between the CBCT duo-

denum and the planning CT duodenum was 0.2 cm, 0.9 cm, 0.6 cm, 1.0 cm, and 0.6 cm for each abdominal compression patient and 1.5 cm, 0.9 cm, and 1.9 cm for each non-compressed patient. This average and the range for each patient is shown in Figure 5.2. The average for the abdominal compression group was 0.7 cm and 1.4 cm for the non compressed group.

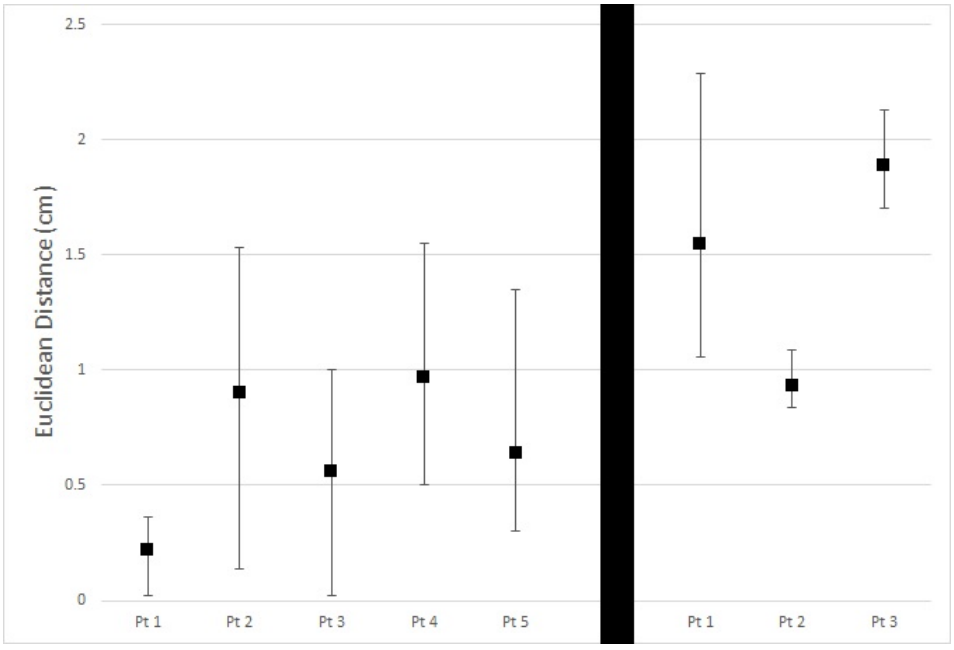


Figure 5.2: Average (and range) of Euclidean distances between the centre-of-mass displacement between the planning CT duodenum and the CBCT duodena for each abdominal compression (left) and non-compressed (right) patient.

The average modified Hausdorff distance between the CBCT duodenum and the planning CT duodenum was 0.1 cm, 0.2 cm, 0.2 cm, 0.3 cm, and 0.3 cm for each abdominal compression patient and 0.6 cm, 0.3 cm, and 0.6 cm for each non-compressed patient. This average and the range for each patient is shown in Figure 5.3. The average for the abdominal compression group was 0.2 cm and 0.5 cm for the non compressed group.

The volume of the duodenum receiving at least 25 (V_{25}), 35, 45, and 50 Gy

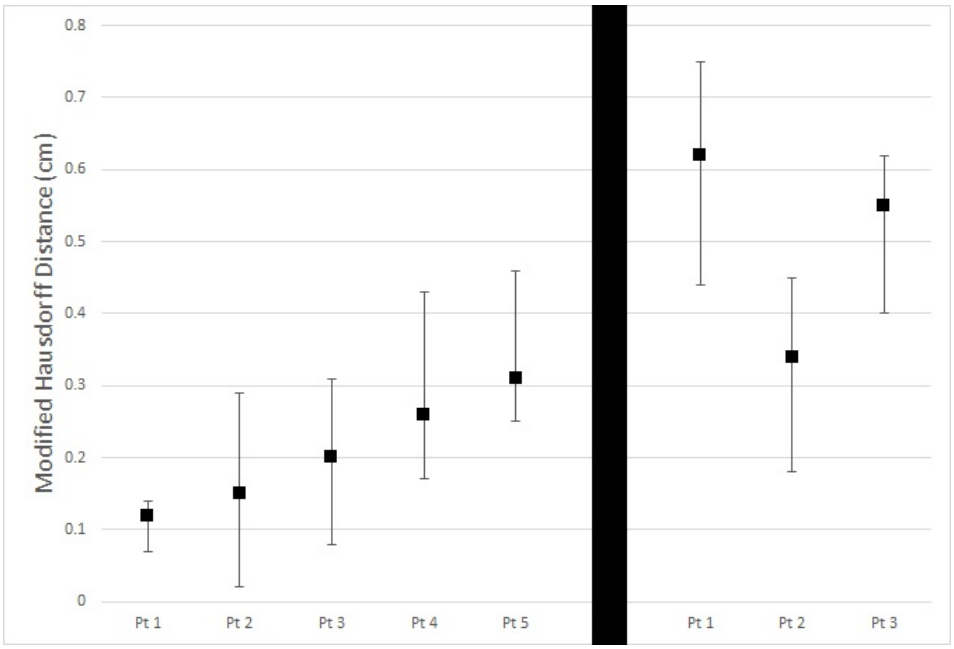


Figure 5.3: Average (and range) of Modified Hausdorff Distances between the planning CT duodenum and the CBCT duodena for each abdominal compression (left) and non-compressed (right) patient.

according to the planning CT for each abdominal compression and non-compressed patient is shown in Table 5.2. It should be noted that this is EQD2, the equivalent dose in 2 Gy fractions.

The largest (and average) difference between the planning CT and CBCTs in volume of duodenum receiving more than 25, 35, 45 and 50 Gy for all abdominal compression patients was 11% (4%), 9% (3%), 9% (2%), and 9% (1%) compared to 6% (1%), 47% (13%), 40% (14%), and 32% (13%). The largest individual patient variation can be seen in Figure 5.4.

5.3.2 Dose Surface Maps for Dose Accumulation

Figure 5.5 shows the planned and accumulated dose-surface maps for the 5 abdominal compression patients. It also shows the dose-difference map between them. The

	Patient	V_{25}	V_{35}	V_{45}	V_{50}
Abdominal Compression	1	9	1	0	0
	2	25	9	0	0
	3	22	17	11	7
	4	11	1	0	0
	5	2	0	0	0
Non-compressed	1	100	100	98	94
	2	100	99	91	81
	3	84	8	5	4

Table 5.2: Volume of duodenum receiving at least 25, 35, 45, and 50 Gy according to the planning CT for both abdominal compression and non-compressed patients. Dose is in gray (EQD2).

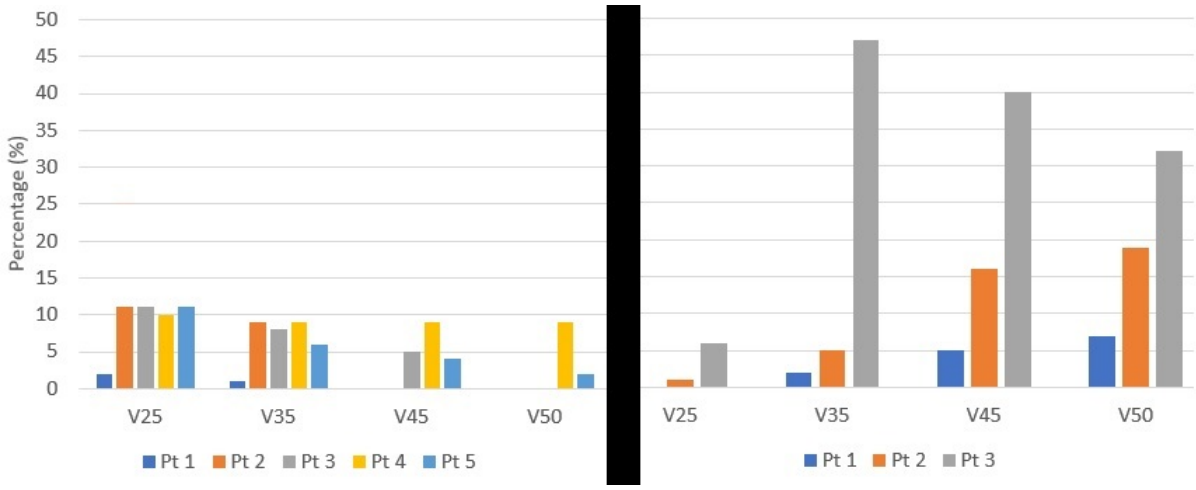


Figure 5.4: Maximum variation in volume receiving at least 25, 35, 45, and 50 Gy between the duodenum contoured on CBCTs compared to the planning CT for each abdominal compression (left) and non-compressed (right) patient.

planned DSM is scaled to 5 fractions and the accumulated DSMs are the addition of the individual CBCT DSMs. Figure 5.6 shows the equivalent for the non-compressed patients with a scaling to 4 fractions due of the availability of contoured CBCTs.

The gamma index between the planned and accumulated dose-surface map was 90%, 88%, 89%, 87%, and 88% for the abdominal compression patients and 77%, 84%, and 53% for the non-compressed patients.

The difference in SM_{10}, 30, 50, 70, and 90 between the planned DSM and accumu-

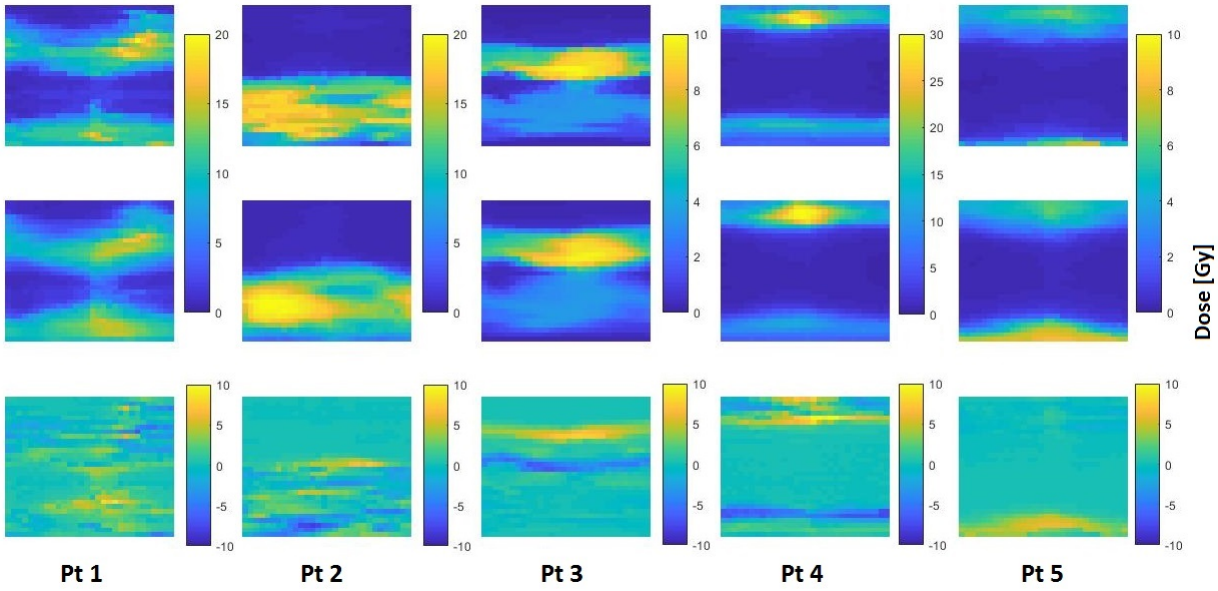


Figure 5.5: For abdominal compression patients: Accumulated dose-surface map by scaling the duodenal dose from the planning CT to 5 fractions (top) and by adding 5 single fraction duodenum doses from the CBCTs (middle). Dose-difference maps for each patient calculated by subtracting the accumulated plan DSM from the accumulated CBCT DSM. Dose shown in gray.

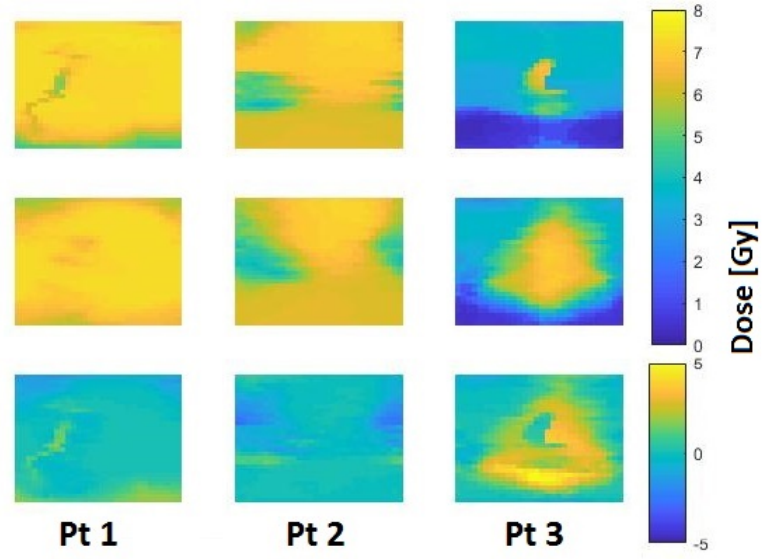


Figure 5.6: For non-compressed patients: Accumulated dose-surface map by scaling the duodenal dose from the planning CT to 4 fractions (top) and by adding 5 single fraction duodenum doses from the CBCTs (middle). Dose-difference maps for each patient calculated by subtracting the accumulated plan DSM from the accumulated CBCT DSM. Dose shown in gray.

Patient	Metric	Plan	Accumulated	Difference
1	SM_{10}	64%	75%	11%
	SM_{30}	45%	50%	5%
	SM_{50}	19%	21%	2%
	SM_{70}	3%	1%	-1%
	SM_{90}	0%	0%	0%
2	SM_{10}	51%	54%	3%
	SM_{30}	47%	48%	1%
	SM_{50}	37%	35%	-1%
	SM_{70}	19%	15%	-4%
	SM_{90}	1%	5%	5%
3	SM_{10}	60%	69%	9%
	SM_{30}	42%	43%	1%
	SM_{50}	18%	21%	3%
	SM_{70}	10%	12%	1%
	SM_{90}	4%	4%	0%
4	SM_{10}	37%	46%	9%
	SM_{30}	26%	32%	7%
	SM_{50}	15%	22%	7%
	SM_{70}	3%	10%	6%
	SM_{90}	0%	4%	4%
5	SM_{10}	42%	43%	1%
	SM_{30}	24%	23%	-1%
	SM_{50}	8%	8%	0%
	SM_{70}	2%	4%	2%
	SM_{90}	1%	2%	1%

Table 5.3: The percent of the plan and accumulated DSM that receives at least 10% (SM_{10}), 30%, 50%, 70%, and 90% of the maximum dose of that DSM and the difference between each metric for the five abdominal compression patients.

lated DSM is shown in Table 5.3 for abdominal compression patients (maximum 11% difference) and Table 5.4 for the non-compressed patients (maximum 30% difference).

5.4 Discussion

Dose to normal tissues in radiotherapy treatment plans are evaluated using a CT of the patient anatomy prior to the start of treatment. Toxicity limiting constraints for these tissues are therefore only guaranteed to be met if the anatomy doesn't

Patient	Metric	Plan	Accumulated	Difference
1	SM_{10}	100%	100%	0%
	SM_{30}	100%	100%	0%
	SM_{50}	100%	100%	0%
	SM_{70}	96%	100%	4%
	SM_{90}	81%	81%	0%
2	SM_{10}	100%	100%	0%
	SM_{30}	100%	100%	0%
	SM_{50}	100%	100%	0%
	SM_{70}	93%	88%	-5%
	SM_{90}	45%	28%	-18%
3	SM_{10}	84%	93%	10%
	SM_{30}	72%	84%	13%
	SM_{50}	44%	66%	22%
	SM_{70}	4%	34%	30%
	SM_{90}	1%	14%	13%

Table 5.4: The percent of the plan and accumulated DSM that receives at least 10% (SM_{10}), 30%, 50%, 70%, and 90% of the maximum dose of that DSM and the difference between each metric for the three non-compressed patients.

change either during or between treatments. For gastrointestinal tumours both inter- and intra-fraction motion are known to impact the position of organs, including the duodenum.

Most studies correlating dose to toxicity, including those on which constraints are based, consider the dose calculated from the planning CT as the delivered dose. This assumption has also been made in the previous chapter (Chapter 4) in this thesis. One method of limiting interfraction motion is the use of abdominal compression. In this chapter we quantified the interfraction changes of the duodenum with and without abdominal compression and studied its effect on duodenal dose-surface maps.

Figure 5.1 shows the range of volumes in the CBCT is generally smaller for patients with abdominal compression, with an average maximal displacement of 24.4 cm^3 compared to 41.2 cm^3 for non-compressed patients. In some studies the planning CT

is considered a baseline and the changes in each CBCT, as compared to the baseline, are recorded. However, since patients followed the same instructions for all imaging, the volume of the duodenum on the planning CT was included when considering the average maximal displacement of volumes during treatment. This methodology essentially treats the planning CT simply as another possible organ position during treatment, rather than an unjustifiable gold standard of anatomy.

While changes in volume provide a quantification of the change in size of the duodenum between fractions, a measure of how much the duodenum has moved is reported by measuring the displacement of the centre of mass (COM) of the duodenum and the modified Hausdorff distance (MHD) between duodena. Both COM displacement (0.7 cm compared to 1.4 cm) and MHD (0.2 cm compared to 0.5 cm) suggest that using abdominal compression reduces the change in position of the duodenum during treatment.

In addition to quantifying anatomical changes, this chapter seeks to investigate the impact of these changes on the amount of dose delivered to the duodenum. The largest and average difference in volume receiving at least 35, 45, and 50 Gy across the CBCTs compared to the planning CT was smaller for abdominal compression patients but the difference in volume receiving at least 25 Gy was smaller in the non-compressed patients. The different trend seen for V_{25} is most likely due to the higher dose DSM of the non-compressed patients. Additionally, the difference between the two groups seen at V_{25} is a lot smaller than the differences seen at V_{35}, V_{45}, and V_{50}.

The smaller dosimetric variations between the abdominal compression patients are due to the smaller changes in volume and position of the duodenum between

fractions as would be expected when using motion management.

A central hypothesis of this thesis is that information from the surface of a hollow organ is more important than volume information. Therefore, in addition to assessing the three dimensional changes in the duodenum, the interfraction variation between dose-surface maps was quantified. Two forms of metrics were used for this analysis: the gamma passing rate, quantifying the similarity of two maps; and dose-surface metrics, quantifying what percentage of a map receives at least a certain dose.

The gamma passing rate comparing the accumulated dose-surface maps to the planning dose-surface maps was higher (87-90% compared to 53-84%) for abdominal compression patients. The comparison of the differences in surface metrics from the accumulated and planning DSMs again shows that the difference was smaller in abdominal compression patients, although still present.

In all attempts to quantify interfraction duodenal changes and differences in the dose-surface map between planned and delivered dose it was found that abdominal compression reduced interfraction variability in our dataset. However, even with abdominal compression it was found that the reduced variability was still large enough to warrant consideration of the use of delivered dose distributions rather than planned dose distributions for toxicity prediction in the duodenum. Additionally, abdominal compression would be particularly useful in high dose per fraction treatments when fewer fractions are delivered.

This study demonstrates the need for, and our ability to create, dose-surface maps from CBCTs that are by definition pseudoregistered with the planning CT so that we can build accumulated dose-surface maps. These accumulated dose-surface maps

present a more accurate record of actual dose delivered to the duodenum. This can be useful in the context of toxicity modelling by using delivered dose to organs, rather than planned dose, in order to build toxicity models in the future. Accumulated dose-surface maps can also be useful in the expanding field of adaptive planning. If an image is taken of the patient anatomy before each treatment, a daily DSM can be produced for hollow organs. This is especially of interest where MR-Linacs are being introduced in the clinic and daily images are being taken of the patient in treatment position.

5.5 Conclusion

In this chapter, the accuracy of the planning CT in representing delivered dose to the duodenum was studied. The ability of abdominal compression to restrict duodenal motion was also assessed. The changes to the duodenum between the planning CT and CBCTs were quantified using the difference in volume, centre of mass displacement, and modified Hausdorff distance and were found to be reduced in abdominal compression patients, although not to a level at which the motion can be ignored. By creating duodenal DSMs from the CBCT images as described in chapter 2, accumulated DSMs were compared to DSMs created from the planning CT. The accumulated DSMs for the abdominal compression patients were found to be more similar to the planning DSMs than for the non-compressed patients, but again there was still a non-negligible difference that should be considered. The work in this chapter points to the fact that the duodenum contour from the planning CT may not accurately represent the delivered dose during treatment. Therefore, this must be considered

when building duodenal toxicity models based on the planning CT alone.

Chapter 6

Summary & Conclusion

6.1 Summary

It has been postulated that dose-volume toxicity models may not be suitable for hollow organs. Single value metrics extracted from dose-volume histograms disregard a large amount of information on the spatial distribution of dose on the organ surface. However, these dose-volume metrics are still used to make clinical decisions worldwide. In the academic community of medical physicists, researchers have been investigating the incorporation of spatial dose information in toxicity prediction models for hollow organs such as the oesophagus, rectum, anal canal, and bladder. In order to extract spatial information, these hollow organs had to be 'unwrapped' and dose-surface maps (DSMs) produced. The methods developed for this were fit-for-purpose but too primitive to unwrap more geometrically complex organs such as the duodenum. Prior to this thesis, the state of the art had been to use a geometric central axis or simply the axial slices to move through the organ and unwrap the surface dose. These methods are insufficient for unwrapping the duodenum.

The starting point in solving this problem was considering the limitations of using

a geometric central axis to unwrap the duodenum. Doing so creates overlapping slices when trying to characterise the surface points. A small study comparing the DSMs of three duodena created from overlapping and non-overlapping slices found the DSMs of one duodenum had a gamma passing rate of 52% (with a 3%/3 pixel criteria). To overcome overlap, the rays would need to be cast from a path that moves close to the areas of curvature. This path is, coincidentally, similar to the path a racecar driver would take through a duodenal-shaped circuit. Chapter 2 presents a novel methodology using a 'racecar' path to define a central axis which is used to unwrap geometrically complex organs, specifically the duodenum. The new central axis is semi-automcatically defined by penalising the length and curvature of a path between two points, namely one point on the top (superior) plane of the duodenum, and one point on the bottom (inferior) plane. Due to this penalty, the path moves close to regions of high curvature. By orientating rays to be cast to the surface on a plane with a normal in the direction of the path, the surface of the duodenum can be meaningfully sampled. An important point to note is that this method of sampling the surface results in each point being a different size. This is acknowledged in the work and a separate lookup table is created storing the absolute size of each DSM pixel. An effort to mitigate this effect is also incorporated into the ray casting stage whereby initially only 8 rays are cast to the surface from the point on the racecar path in order to redefine the point from which the final rays are cast as the centroid of the resulting polygon. This results in a more even distribution of surface points when the final 30 rays are cast compared to if these were cast from the initial point close to the area of high curvature. The dose-surface maps produced using this technique

were the first created for the duodenum and unlocked the potential for further study.

This new methodology extends the capabilities of unwrapping tubular organs. After designing the process to specifically unwrap a geometrically complex organ such as the duodenum, Chapter 3 demonstrates the methods' generalisability by unwrapping other organs and presenting a software prototype with which to do it. An obvious extension within the GI tract that would be useful to the thesis' aim of investigating upper GI toxicity is the unwrapping of the stomach. Even though the stomach is not geometrically complex and could be unwrapped using techniques previously available in the literature, this thesis is still the first to present stomach dose-surface maps. Another hollow organ which could be unwrapped in the GI tract is the small bowel. However, the contouring detail in this organ does not allow for unwrapping using this method. If the level of contouring was improved to result in a single tube defining the small bowel, the methodology described in this thesis would still be valid.

The next test for the new unwrapping methodology was to apply it to other geometrically complex hollow organs. The bronchial tree is hollow, complex (due to the bifurcation), has not been previously unwrapped, and is linked to toxicity in lung cancer treatments. All these made the bronchial tree an appealing organ to unwrap next. A framework built on the same methodology as the duodenum but accounting for the bifurcation of the bronchial tree was also presented in Chapter 3. The key to the bifurcation solution was separating the organ into multiple tubes. Once this is done each tube can be unwrapped individually but some areas of each tube representing on overlapping area of the bronchial tree. By identifying these areas

and removing these pixels from the more superior tube, meaningful dose-surface maps of the bronchial tree were created. Even though dose to the bronchial tree and its proximity to non-small cell lung cancer tumours has been shown to cause severe and sometimes fatal toxicity, this thesis contains the first description of a method to unwrap this organ. It is hoped that this will lead to the inclusion of the spatial distribution of dose as a possible predictor of toxicity in centrally located tumours.

The final part of Chapter 3 addresses the need to translate research into clinic use. This step is often left out when developing new techniques in a research environment. In order to provide access to the spatial information contained in a dose-surface map in the clinic, a graphical user interface (GUI) that can access data directly from commercial treatment planning systems (Eclipse, Varian Medical Systems, Palo Alto, CA, USA and Raystation, RaySearch Laboratories AB, Stockholm, Sweden) is presented. While Section 1.7 discusses the possible correlations found between toxicity and spatial dose metrics in various organs, none of these metrics have been incorporated into the clinical decision making process or even been investigated in additional cohorts. A major roadblock to either of these events occurring is the ability to create dose-surface maps without the additional resources only large academic institutions can provide. Additionally, the only commercial software (VODCA, MSS Medical Software Solutions, Hagendorn, Switzerland) known to create dose-surface maps is unable to handle complex geometries. The GUI presented here, which can interface with commercial treatment planning systems, was created as a tool for other clinics to unwrap hollow organs, validate new spatial metrics that may be found to correlate with toxicity, and utilise spatial metrics in the treatment planning process.

Using the duodenum and stomach dose-surface maps created in previous chapters, Chapter 4 extracts spatial dose information and correlated these to toxicity found in two clinical trials (Section 2.2.1). Once dose-surface maps are created, a number of metrics can be analysed using a variety of techniques. Dose-surface metrics analogous to dose-volume metrics are perhaps the most easily understood as they correspond to current clinical metrics. Here the surface area receiving a threshold dose is quantified, rather than the volume. This is a very simple alternative to dose-volume metrics and gives more relevant information for hollow organs. While dose-surface metrics have not been analysed for toxicity correlation in the duodenum or stomach before, the tools with which to extract them have been built into commercial treatment planning systems without the need for dose-surface maps. In the clinical trials analysed, the stomach dose-surface metrics (AUCs = 0.78 - 0.90) showed a slight improvement in predictive power of grade $\geqslant 2$ upper-GI toxicity over the stomach dose-volume metrics (AUCs = 0.78 - 0.85). Shifting focus from dose to the volume of a hollow organ to dose to the surface is only half the goal of this thesis. The bigger challenge is to incorporate the spatial distribution of the surface dose of the organ.

Spatial metrics such as the length of the organ over which a threshold percentage of the circumference is spared a threshold dose also offered a similar advantage as dose-surface metrics with AUCs = 0.77 - 0.91. Another technique for correlating dose-surface maps with toxicity is a pixel-by-pixel approach. The permutation test performed in Chapter 4 tested individual pixels in the dose-surface map for correlation with toxicity and then extracted the mean dose in the region of interest where $p < 0.2$. This metric resulted in an AUC of 0.97 for predicting $\geqslant 2$ toxicity in the ARCII

trial and an AUC of 0.71 in the SCALOP trial. The AUC of 0.97 is very high for ARCII and is likely inflated due to the lack of cross validation in defining the region of interest. The AUC for SCALOP is also not very meaningful due to the region of interest consisting of a single pixel meaning that even though this was the only metric to have a statistically significant prediction in the SCALOP dataset, it does not translate to a clinically useful metric. This single pixel case is a good example in the predictability vs interpretability debate whereby this single-pixel metric was predictive but no interpretable. Although analysis on grade $\geqslant 3$ toxicity was also completed in this chapter, the incidence of this grade of toxicity was too low in both clinical trials to yield any conclusions. For grade $\geqslant 2$ toxicity, the analysis shows various metrics that can be extracted from dose-surface maps which greatly increases the amount of information available compared to dose-volume metrics. In this particular dataset, both the dose-surface information and spatial information had slightly improved predictive power over dose-volume metrics. However due to the lack of agreement on which metric was the best predictor between both clinical trials, most likely because of the small sample size and the different protocols between them, no clinical recommendations can be made.

It is important to remember that Chapter 4 correlates dosimetric features extracted from the planning CT. Chapter 5 questions whether this dose information is the correct information to use when building dose-toxicity models in the abdomen. Abdominal anatomy suffers from an uncertainty in daily position and therefore the anatomy images on the day of the planning CT may not be the same anatomy as on each treatment day, which in turn may not be the same as each other. A technique

called abdominal compression can be used to limit anatomical changes and Chapter 5 shows a reduction in maximum volume changes during treatment from an average of 35.4 cm^3 to 21.4 cm^3 when using this technique. Other quantifications of change, including centre of mass displacement (for positional changes) and modified Hausdorff distance (to account for peristalsis), were also reduced on average from 1.4 cm to 0.7 cm and from 0.5 cm to 0.2 cm respectively.

It was shown that the pseudoregistration of the unwrapping technique described in Chapter 2 allowed for the accumulation of dose-surface maps using daily images. Accumulated dose-surface maps (a summation of dose-surface maps created from daily imaging) were also compared to the planning dose-surface maps and found to agree with a higher gamma passing rate of 87-90% with abdominal compression compared to just 53-84% without it. Both dose-volume and dose-surface metrics were found in general to have a greater difference without compression, but even those with compression saw differences of up to 11%. It can be largely concluded that abdominal compression reduces duodenal motion throughout treatment but that it does not completely remove the need to consider interfraction changes. This is because part of the motion is due to peristalsis, which the compression does not reduce. The work in Chapter 5 is promising, especially with the introduction of MR-Linacs in the clinc, where the workflow requires daily imaging. This chapter shows that daily dose-surface maps of the duodenum can be created and the dosimetric effect quantified which can be used to aid in adaptive planning.

6.2 Future Directions

Unwrapping the contour of the duodenum from a CT scan into a 2D dose-surface map was always intended to be a virtual process but from the outset the plan was to pathologically validate this virtual technique with a physical specimen. The intention was to physically cut and unwrap a post-radiotherapy resected duodenum. The areas of high dose could have been identified pathologically.

While relatively little is known about the pathophysiology of gastrointestinal radiation injury, the acute symptoms considered in this thesis are typically related to acute mucosal injury causing erosions and ulceration of gastric and duodenal mucosa. Direct radiation injury to the mucosa can also cause epithelial atrophy, and reduced mucosal blood flow [86]. While the correlation of the spatial dose distribution to pathological damage has not been previously attempted, Verma et al. [87] correlated dose-volume metrics with duodenal histopathology damage for patients treated with SABR for pancreatic cancer. This study found that dose-volume metrics did not correlate with clinical toxicities, but did correlate with higher pathological duodenal damage scores. Higher pathological damage scores corresponded to the amount of mucosal damage as defined by the gastrointestinal surgical pathologist.

It was hoped that in this thesis the areas identified by a pathologist as more damaged than others would correspond to the areas of high dose on the dose-surface map. In a similar fashion to Verma et al. [87], the spatial dose metrics found in this thesis could also be correlated to overall pathological damage. Unfortunately, during the span of this project a physical specimen was not accessible.

An alternative geometric validation could be performed by CT scanning a phantom of similar geometry to the duodenum (or even a 3D printed duodenum) with some markers placed on the surface. The predicted location of these markers from the CT scan identified using the virtual unwrapping technique could be compared to the true location. This could also be used to test the geometric limitations of the methodology described in this thesis. The only reason this avenue was not explored is that it had been hoped that the pathological validation would combine a geometric validation with a new spatial dose metric to pathological damage correlation study.

Some groups [72, 83] have performed endoscopy on patients to identify toxicity such as ulceration, bleeding, and perforation. Having access to this data can help both validate the unwrapping technique, and enable the analysis of the spatial distribution of dose for those cases with localised tissue damage. A simple study could hypothesise and association between the location of the dose hotspot and the region of toxicity.

Most of the work in this thesis is based on data from two clinical trials containing 19 (ARCII) and 62 (SCALOP) patients. The incidence of grade $\geqslant 3$ toxicity in both these trials was low. Since both trials had different total prescriptions the data could not be combined. Both these datasets are very small, especially for the statistical tests in Section 4.2.7. While this thesis provides a framework and initial results for dose-surface map analysis, continuation of this work on a larger dataset would yield more conclusive results and perhaps indicate anatomical regions that are more sensitive to radiation.

One reasons that small trial datasets are still found in pancreatic cancer is the large number of treatment options and data collection techniques used in different

treatment centres. To avoid the frustrations of repeated inconclusive analyses, there needs to be a shift to general purpose tools that can be disseminated to major centres. This is especially true in the case of specialised analyses, such as dose-surface maps, where the work in this thesis can generate both prospective and retrospective data for analysis at any centre that has toxicity information for their patients.

The work in this thesis is also applicable to other hollow organs. While some groups have been working on the oesophagus, bladder, anal canal, and rectum, there are still no tools to make hollow organ dose-surface map creation accessible to all. The graphical user interface described in Chapter 3 of this thesis will allow for large dose-surface map datasets to be created, and adding the capability to unwrap the bronchial tree to this application would also be highly desirable for those working on non-small-cell lung cancer.

The use of the application developed would set a good precedent where a methodology developed in an academic centre is packaged into an application that can be distributed as open-source software, or preferably through a professional society so that support can be offered and collaborations started.

When recommending a move from traditional dose-volume to dose-surface metrics it is important to consider the increased complexity in extracting surface dose using new unfamiliar tools and the greater uncertainty that these carry over established methods. Additionally, with dose-surface metrics there is an increased susceptibility to inter-fraction variability. While considering the dose to the organ surface may be more scientifically justifiable for some organs, the dose to the organ volume may be less sensitive. Some of these concerns can be addressed by creating accumulated dose-

surface maps using daily imaging, thereby reducing the inter-fraction uncertainty. This is a more ambitious future direction which includes the use of dose-surface maps for adaptive therapy.

A recent technological advance in the clinical settings is the use of the MR-Linac for radiotherapy treatment. With this machine the patient is imaged every day in the treatment position. If the unwrapping technique described in this thesis is utilised to produce daily dose-surface maps it is hypothesised that, due to interfraction motion, on some days the duodenum and stomach may be in a favourable anatomical position where they are receiving less dose, and on other days they may be in unfavourable positions. This could be identified in the daily DSM and the dose for that particular fraction can be accordingly increased or decreased.

6.3 Conclusion

This thesis has demonstrated the feasibility of creating dose-surface maps for tortuous organs such as the duodenum by creating these maps, for the first time, for the duodenum, stomach, and bronchial tree. It also presents a graphical user interface which can be used to create dose-surface maps for most organs from a commercial treatment planning system. These DSMs provide information on the spatial surface dose distribution from which new spatial metrics were extracted and correlated with upper-gastrointestinal toxicity. The predictive power of these surface and spatial metrics in the stomach were found to be superior to dose-volume metric models. No statistically significant correlation was found in the duodenum. Changes in the duodenum throughout treatment was shown to be non-systematic and therefore can-

not be predicted. Abdominal compression was shown to reduce interfraction changes in the duodenum but was not able to control changes due to peristalsis. Accumulated dose-surface maps made from daily imaging were created as a more accurate description of delivered dose.

Publications & Awards

Peer Reviewed Journal Articles

A Witztum, B George, S Warren, M Partridge, and MA Hawkins. Unwrapping 3D complex hollow organs for spatial dose surface analysis. *Medical Physics*, 43(11): 6009-6016, 2016[II,III]

Peer Reviewed Conference Proceedings

A Witztum, B George, F Van den Heuvel, and MA Hawkins. Pixel-Based Analysis of Stomach Dose-Surface Maps to Improve Toxicity Predictions in Gastrointestinal Radiotherapy *Medical Physics*, 44(6): 2998, 2017[IV]
AAPM 2017 Annual Meeting, Denver, Colorado, USA

A Witztum, B George, M Partridge, F Van den Heuvel, and MA Hawkins. Spatial Dose Surface Map Visualization for Hollow Organ Dose Evaluation *Journal of Applied Clinical Medical Physics*, 18(3): 235, 2017[III]
AAPM 2017 Spring Clinical Meeting, New Orleans, Louisiana, USA

A Witztum, D Holyoake, S Warren, M Partridge, MA Hawkins. Duodenal Interfraction Motion with Abdominal Compression *Medical Physics*, 43(6): 3340, 2016[V]
AAPM 2016 Annual Meeting, Washington DC, USA

[II] Work from this publication is presented in Chapter 2
[III] Work from this publication is presented in Chapter 3
[IV] Work from this publication is presented in Chapter 4
[V] Work from this publication is presented in Chapter 5

A Witztum, S Warren, M Partridge, MA Hawkins. Texture Analysis for Toxicity Prediction From Dose Surface Maps. *Medical Physics*, 43(6): 3486, 2016
AAPM 2016 Annual Meeting, Washington DC, USA

A Witztum, S Warren, M Partridge, MA Hawkins. Feature extraction from duodenal dose surface maps to predict toxicity in pancreatic chemoradiation. *Radiotherapy and Oncology*, 119(S1): S805, 2016 [IV]
ESTRO 2016 Annual Meeting, Turin, Italy

A Witztum, S Warren, M Partridge, MA Hawkins. A Method of Unwrapping 3D Complex Hollow Organs for Spatial Dose Surface Analysis. *Medical Physics*, 42(6): 3706, 2015 [II,III]
AAPM 2015 Annual Meeting, Anaheim, California, USA

A Witztum, S Warren, D Holyoake, M Partridge, S Mukherjee, MA Hawkins. The dosimetric effect of interfraction motion on the duodenum in pancreatic radiotherapy. *Radiotherapy and Oncology*, 115(S1): S800-801, 2015 [V]
ESTRO 2015 Annual Meeting, Barcelona, Spain

Awards

1st Place Young Investigator Award - AAPM Spring Clinical Meeting - April 2017
Spatial Dose Surface Map Visualization for Hollow Organ Dose Evaluation

Santander Academic Travel Award - £750 - December 2015

MRC Supplementary Funding Award - £3,000 - September 2015
Overseas fieldwork and training in new advanced research skills

Bibliography

[1] Office. of National Statistics. Cancer registration statistics, england: first release, 2016. http://www.ons.gov.uk. Retrieved 18 February, 2018.

[2] Cancer Research. UK. Statistics and outlook for pancreatic cancer. http://www.cancerresearchuk.org/health-professional/cancer-statistics/statistics-by-cancer-type/pancreatic-cancer. Retrieved 24 March, 2018.

[3] Cancer Research. UK. One-, five- and ten-year survival for common cancers. http://www.cancerresearchuk.org/health-professional/cancer-statistics/survival/common-cancers-compared. Retrieved 24 March, 2018.

[4] B. Gudjonsson. Cancer of the pancreas: 50 years of surgery. *Cancer*, 60(9):2284–2303, 1987.

[5] H. Gray. *Anatomy of the Human Body.* Lea & Febiger, 20 edition, 1918.

[6] J. D. Murphy, S. Adusumilli, K. A. Griffith, M. E. Ray, M. M. Zalupski, T. S. Lawrence, and E. Ben-Josef. Full-dose gemcitabine and concurrent radiotherapy for unresectable pancreatic cancer. *Int. J. Radiat. Oncol. Biol. Phys.*, 68(3):801–8, 2007.

[7] P. Kelly, P. Das, C. C. Pinnix, S. Beddar, T. Briere, M. Pham, S. Krishnan, M. E. Delclos, and C. H. Crane. Duodenal toxicity after fractionated chemoradiation for unresectable pancreatic cancer. *Int. J. Radiat. Oncol. Biol. Phys.*, 85(3):e143–9, 2013.

[8] S. Krishnan, V. Rana, N. A. Janjan, G. R. Varadhachary, J. L. Abbruzzese, P. Das, M. E. Delclos, M. S. Gould, D. B. Evans, R. A. Wolff, and C. H.

Crane. Induction chemotherapy selects patients with locally advanced, unresectable pancreatic cancer for optimal benefit from consolidative chemoradiation therapy. *Cancer*, 110(1):47–55, 2007.

[9] C. H. Crane, G. R. Varadhachary, J. S. Yordy, G. A. Staerkel, M. M. Javle, H. Safran, W. Haque, B. D. Hobbs, S. Krishnan, J. B. Fleming, P. Das, J. E. Lee, J. L. Abbruzzese, and R. A. Wolff. Phase II trial of cetuximab, gemcitabine, and oxaliplatin followed by chemoradiation with cetuximab for locally advanced (T4) pancreatic adenocarcinoma: correlation of Smad4(Dpc4) immunostaining with pattern of disease progression. *J. Clin. Oncol.*, 29(22):3037–43, 2011.

[10] C. Li, Y. Chao, K.-H. Chi, W.-K. Chan, H.-C. Teng, R.-C. Lee, F.-Y. Chang, S.-D. Lee, and S.-H. Yen. Concurrent chemoradiotherapy treatment of locally advanced pancreatic cancer: Gemcitabine versus 5-fluorouracil, a randomized controlled study. *Int. J. Radiat. Oncol. Biol. Phys.*, 57(1):98–104, 2003.

[11] K. A. Goodman and C. Hajj. Role of radiation therapy in the management of pancreatic cancer. *J. Surg. Oncol.*, 107(1):86–96, 2013.

[12] S. Krishnan, A. S. Chadha, Y. Suh, P. Das, B. D. Minsky, U. Mahmood, M. E. Delclos, G. O. Sawakuchi, S. Beddar, M. H. Katz, J. B. Fleming, M. M. Javle, G. R. Varadhachary, R. A. Wolff, and C. H. Crane. Focal radiotherapy dose escalation improves overall survival in locally advanced pancreatic cancer patients receiving induction chemotherapy and consolidative chemoradiation. *Int. J. Radiat. Oncol. Biol. Phys.*, dec 2015.

[13] C. A. Iacobuzio-Donahue, B. Fu, S. Yachida, M. Luo, H. Abe, C. M. Henderson, F. Vilardell, Z. Wang, J. W. Keller, P. Banerjee, and et al. Dpc4 gene status of the primary carcinoma correlates with patterns of failure in patients with pancreatic cancer. *Journal of Clinical Oncology*, 27(11):18061813, Oct 2009.

[14] H. M. Ceha, G. van Tienhoven, D. J. Gouma, C. H. Veenhof, C. J. Schneider, E. A. Rauws, S. S. Phoa, and D. González González. Feasibility and efficacy of high dose conformal radiotherapy for patients with locally advanced pancreatic carcinoma. *Cancer*, 89(11):2222–9, 2000.

[15] M. W. Brown, H. Ning, B. Arora, P. S. Albert, M. Poggi, K. Camphausen, and D. Citrin. A dosimetric analysis of dose escalation using two intensity-modulated

radiation therapy techniques in locally advanced pancreatic carcinoma. *Int. J. Radiat. Oncol. Biol. Phys.*, 65(1):274283, 2006.

[16] E. Ben-Josef, M. Schipper, I. R. Francis, S. Hadley, R. Ten-Haken, T. Lawrence, D. Normolle, D. M. Simeone, C. Sonnenday, R. Abrams, W. Leslie, G. Khan, and M. M. Zalupski. A phase I/II trial of intensity modulated radiation (IMRT) dose escalation with concurrent fixed-dose rate gemcitabine (FDR-G) in patients with unresectable pancreatic cancer. *Int. J. Radiat. Oncol. Biol. Phys.*, 84(5):1166–71, 2012.

[17] A. C. Spalding, K.-W. Jee, K. Vineberg, M. Jablonowski, B. A. Fraass, C. C. Pan, T. S. Lawrence, R. K. T. Haken, and E. Ben-Josef. Potential for dose-escalation and reduction of risk in pancreatic cancer using imrt optimization with lexicographic ordering and geud-based cost functions. *Med. Phys.*, 34(2):521529, 2007.

[18] B. Emami, J. Lyman, A. Brown, L. Coia, M. Goitein, J. E. Munzenrider, B. Shank, L. J. Solin, and M. Wesson. Tolerance of normal tissue to therapeutic irradiation. *Int. J. Radiat. Oncol. Biol. Phys.*, 21(1):109–22, 1991.

[19] L. B. Marks, E. D. Yorke, A. Jackson, R. K. Ten Haken, L. S. Constine, A. Eisbruch, S. M. Bentzen, J. Nam, and J. O. Deasy. Use of normal tissue complication probability models in the clinic. *Int. J. Radiat. Oncol. Biol. Phys.*, 76(3 Suppl):S10–9, mar 2010.

[20] B. D. Kavanagh, C. C. Pan, L. A. Dawson, S. K. Das, X. A. Li, R. K. T. Haken, and M. Miften. Radiation dosevolume effects in the stomach and small bowel. *Int. J. Radiat. Oncol. Biol. Phys.*, 76(3), 2010.

[21] J. Huang, J. M. Robertson, H. Ye, J. Margolis, L. Nadeau, and D. Yan. DoseVolume Analysis of Predictors for Gastrointestinal Toxicity After Concurrent Full-Dose Gemcitabine and Radiotherapy for Locally Advanced Pancreatic Adenocarcinoma. *Int. J. Radiat. Oncol. Biol. Phys.*, 83(4):1120–1125, 2012.

[22] A. Nakamura, K. Shibuya, Y. Matsuo, M. Nakamura, T. Shiinoki, T. Mizowaki, and M. Hiraoka. Analysis of dosimetric parameters associated with acute gastrointestinal toxicity and upper gastrointestinal bleeding in locally advanced pan-

creatic cancer patients treated with gemcitabine-based concurrent chemoradiotherapy. *Int. J. Radiat. Oncol. Biol. Phys.*, 84(2):369–75, oct 2012.

[23] G. M. Cattaneo, P. Passoni, B. Longobardi, N. Slim, M. Reni, S. Cereda, N. di Muzio, and R. Calandrino. Dosimetric and clinical predictors of toxicity following combined chemotherapy and moderately hypofractionated rotational radiotherapy of locally advanced pancreatic adenocarcinoma. *Radiother. Oncol.*, 108(1):66–71, 2013.

[24] S. Li, A. Boyer, Y. Lu, and G. T. Chen. Analysis of the dose-surface histogram and dose-wall histogram for the rectum and bladder. *Med. Phys.*, 24(7):1107–16, 1997.

[25] R. I. MacKay, J. H. Hendry, C. J. Moore, P. C. Williams, and G. Read. Predicting late rectal complications following prostate conformal radiotherapy using biologically effective doses and normalized dose-surface histograms. *Brit. J. Radiol.*, 70(833):517–26, 1997.

[26] J. D. Fenwick, V. S. Khoo, A. E. Nahum, B. Sanchez-Nieto, and D. P. Dearnaley. Correlations between dose-surface histograms and the incidence of long-term rectal bleeding following conformal or conventional radiotherapy treatment of prostate cancer. *Int. J. Radiat. Oncol. Biol. Phys.*, 49(2):473–80, 2001.

[27] G. J. Meijer, M. van den Brink, M. S. Hoogeman, J. Meinders, and J. V. Lebesque. Dosewall histograms and normalized dosesurface histograms for the rectum: a new method to analyze the dose distribution over the rectum in conformal radiotherapy. *Int. J. Radiat. Oncol. Biol. Phys.*, 45(4):1073–1080, nov 1999.

[28] M. S. Hoogeman, S. T. H. Peeters, J. D. Bois, and J. V. Lebesque. Absolute and relative dosesurface and dosevolume histograms of the bladder: which one is the most representative for the actual treatment? *Phys. Med. Bio.*, 50(15):35893597, 2005.

[29] P. D. Maguire, G. S. Sibley, S.-M. Zhou, T. A. Jamieson, K. L. Light, P. A. Antoine, J. E. Herndon, M. S. Anscher, and L. B. Marks. Clinical and dosimetric predictors of radiation-induced esophageal toxicity. *Int. J. Radiat. Oncol. Biol. Phys.*, 45(1):97–103, 1999.

[30] S. M. Zhou, L. B. Marks, G. S. Tracton, G. S. Sibley, K. L. Light, P. D. Maguire, and M. S. Anscher. A new three-dimensional dose distribution reduction scheme for tubular organs. *Med. Phys.*, 27(8):1727–31, 2000.

[31] R. Munbodh, A. Jackson, J. Bauer, C. R. Schmidtlein, and M. J. Zelefsky. Dosimetric and anatomic indicators of late rectal toxicity after high-dose intensity modulated radiation therapy for prostate cancer. *Med. Phys.*, 35(5):2137–50, 2008.

[32] F. Buettner, S. L. Gulliford, S. Webb, and M. Partridge. Using dose-surface maps to predict radiation-induced rectal bleeding: a neural network approach. *Phys. Med. Biol*, 54:5139–5153, 2009.

[33] F. Buettner, S. L. Gulliford, S. Webb, M. R. Sydes, D. P. Dearnaley, and M. Partridge. Assessing correlations between the spatial distribution of the dose to the rectal wall and late rectal toxicity after prostate radiotherapy: an analysis of data from the MRC RT01 trial (ISRCTN 47772397). *Phys. Med. Biol.*, 54(21):6535–48, 2009.

[34] M. S. Hoogeman, M. van Herk, J. de Bois, P. Muller-Timmermans, P. C. M. Koper, and J. V. Lebesque. Quantification of local rectal wall displacements by virtual rectum unfolding. *Radiother. Oncol.*, 70(1):21–30, 2004.

[35] J. E. Scaife, S. J. Thomas, K. Harrison, M. Romanchikova, M. P. F. Sutcliffe, J. R. Forman, A. M. Bates, R. Jena, M. A. Parker, and N. G. Burnet. Accumulated dose to the rectum, measured using dose-volume histograms and dose-surface maps, is different from planned dose in all patients treated with radiotherapy for prostate cancer. *Brit. J. Radiol.*, 88(1054):20150243, oct 2015.

[36] L. E. A. Shelley, J. E. Scaife, M. Romanchikova, K. Harrison, J. R. Forman, A. M. Bates, D. J. Noble, R. Jena, M. A. Parker, M. P. F. Sutcliffe, S. J. Thomas, and N. G. Burnet. Delivered dose can be a better predictor of rectal toxicity than planned dose in prostate radiotherapy. *Radiother. Oncol.*, 123(3):466–471, 2017.

[37] R. C. Wortel, M. G. Witte, U. A. van der Heide, F. J. Pos, J. V. Lebesque, M. van Herk, L. Incrocci, and W. D. Heemsbergen. Dosesurface maps identifying local doseeffects for acute gastrointestinal toxicity after radiotherapy for prostate cancer. *Radiother. Oncol.*, 117(3):515–520, 2015.

[38] F. Palorini, A. Botti, V. Carillo, S. Gianolini, I. Improta, C. Iotti, T. Rancati, C. Cozzarini, and C. Fiorino. Bladder dosesurface maps and urinary toxicity: Robustness with respect to motion in assessing local dose effects. *Physica Medica*, 32(3):506511, 2016.

[39] F. Palorini, C. Cozzarini, S. Gianolini, A. Botti, V. Carillo, C. Iotti, T. Rancati, R. Valdagni, and C. Fiorino. First application of a pixel-wise analysis on bladder dosesurface maps in prostate cancer radiotherapy. *Radiother. Oncol.*, 119(1):123–128, 2016.

[40] N. Yahya, M. A. Ebert, M. J. House, A. Kennedy, J. Matthews, D. J. Joseph, and J. W. Denham. Modeling Urinary Dysfunction After External Beam Radiation Therapy of the Prostate Using Bladder Dose-Surface Maps: Evidence of Spatially Variable Response of the Bladder Surface. *Int. J. Radiat. Oncol. Biol. Phys.*, 97(2):420–426, 2017.

[41] F. Buettner, S. L. Gulliford, S. Webb, M. R. Sydes, D. P. Dearnaley, and M. Partridge. The doseresponse of the anal sphincter region An analysis of data from the MRC RT01 trial. *Radiother. Oncol.*, 103(3):347–352, 2012.

[42] F. Dankers, R. Wijsman, E. G. C. Troost, R. Monshouwer, J. Bussink, and A. L. Hoffmann. Esophageal wall dose-surface maps do not improve the predictive performance of a multivariable ntcp model for acute esophageal toxicity in advanced stage nsclc patients treated with intensity-modulated (chemo-)radiotherapy. *Phys. Med. Bio.*, 62(9):36683681, May 2017.

[43] S. Haker, S. Angenent, A. Tannenbaum, and R. Kikinis. Nondistorting flattening maps and the 3-D visualization of colon CT images. *IEEE transactions on medical imaging*, 19(7):665–70, jul 2000.

[44] P. J. Bryan, S. Custar, J. R. Haaga, and V. Balsara. Respiratory movement of the pancreas: an ultrasonic study. *J. Ultrasound Med.*, 3(7):317–20, 1984.

[45] I. Suramo, M. Päivänsalo, and V. Myllylä. Cranio-caudal movements of the liver, pancreas and kidneys in respiration. *Acta Radiol. Diagn. (Stockh).*, 25(2):129–31, 1984.

[46] M. Feng, J. M. Balter, D. Normolle, S. Adusumilli, Y. Cao, T. L. Chenevert, and E. Ben-Josef. Characterization of Pancreatic Tumor Motion Using Cine MRI: Surrogates for Tumor Position Should Be Used With Caution. *Int. J. Radiat. Oncol. Biol. Phys.*, 74(3):884–891, 2009.

[47] B. Bussels, L. Goethals, M. Feron, D. Bielen, S. Dymarkowski, P. Suetens, and K. Haustermans. Respiration-induced movement of the upper abdominal organs: a pitfall for the three-dimensional conformal radiation treatment of pancreatic cancer. *Radiother. Oncol.*, 68(1):6974, 2003.

[48] S. D. Goldstein, E. C. Ford, M. Duhon, T. Mcnutt, J. Wong, and J. M. Herman. Use of respiratory-correlated four-dimensional computed tomography tp determine acceptable treatment margins for locally advanced pancreatic adenocarcinoma. *Int. J. Radiat. Oncol. Biol. Phys.*, 76(2):597–602, 2010.

[49] A. Tai, Z. Liang, B. Erickson, and X. A. Li. Management of respiration-induced motion with 4-dimensional computed tomography (4dct) for pancreas irradiation. *Int. J. Radiat. Oncol. Biol. Phys.*, 86(5):908913, 2013.

[50] J. L. Hallman, S. Mori, G. C. Sharp, H.-M. Lu, T. S. Hong, and G. T. Chen. A Four-Dimensional Computed Tomography Analysis of Multiorgan Abdominal Motion. *Int. J. Radiat. Oncol. Biol. Phys.*, 83(1):435–441, 2012.

[51] A. K. Singh, R. M. Tierney, D. A. Low, P. J. Parikh, R. J. Myerson, J. O. Deasy, C. S. Wu, G. C. Pereira, S. H. Wahab, S. Mutic, P. W. Grigsby, and A. J. Hope. A prospective study of differences in duodenum compared to remaining small bowel motion between radiation treatments: implications for radiation dose escalation in carcinoma of the pancreas. *Radiat. Oncol.*, 1(1):33, 2006.

[52] S. Hoon Jung, S. Min Yoon, S. Ho Park, B. Cho, J. Won Park, J. Jung, J.-h. Park, J. Hoon Kim, and S. Do Ahn. Four-dimensional dose evaluation using deformable image registration in radiotherapy for liver cancer. *Med. Phys.*, 40(1):011706, 2012.

[53] T. Hashimoto, H. Shirato, M. Kato, K. Yamazaki, N. Kurauchi, T. Morikawa, S. Shimizu, Y. C. Ahn, Y. Akine, and K. Miyasaka. Real-time monitoring of a digestive tract marker to reduce adverse effects of moving organs at risk (OAR)

in radiotherapy for thoracic and abdominal tumors. *Int. J. Radiat. Oncol. Biol. Phys.*, 61(5):1559–64, 2005.

[54] T. Basu, T. Kataria, D. Gupta, S. Bisht, A. Abhishek, S. Goyal, S. Krishnan, K. Narang, S. Sambasivam, and S. Banerjee. Quantification of Duodenum motion: analysis from respiratory phase guided radiotherapy planning scan. *Radiother. Oncol.*, 119:S423–S424, 2016.

[55] K. Mittauer, S. Rosenberg, M. Geurts, I. Chen, L. Henke, J. Olsen, R. Kashani, A. Wojcieszynski, P. Harari, J. Bayouth, Z. Labby, P. Hill, B. Paliwal, P. Parikh, and M. Bassetti. Multi-Institutional Investigation of Relative Pancreatic Tumor to Duodenal Motion in Magnetic Resonance Imaging Guided Radiation Therapy for Potential Online Adaptive Radiation Therapy. *Int. J. Radiat. Oncol. Biol. Phys.*, 96(2):S212–S213, 2016.

[56] F. Liu, B. Erickson, C. Peng, and X. A. Li. Characterization and management of interfractional anatomic changes for pancreatic cancer radiotherapy. *Int. J. Radiat. Oncol. Biol. Phys.*, 83(3):e423–9, 2012.

[57] EU Clinical Trials Register. A Phase II study in patients with locally advanced pancreatic carcinoma: ARC-II Akt-inhibition by Nelfinavir plus chemoradiation with gemcitabine and cisplatin. https://www.clinicaltrialsregister.eu/ctr-search/trial/2008-006302-42/GB#P. Retrieved 19 August, 2015.

[58] S. Mukherjee, C. N. Hurt, J. Bridgewater, S. Falk, S. Cummins, H. Wasan, T. Crosby, C. Jephcott, R. Roy, G. Radhakrishna, A. McDonald, R. Ray, G. Joseph, J. Staffurth, R. A. Abrams, G. Griffiths, and T. Maughan. Gemcitabine-based or capecitabine-based chemoradiotherapy for locally advanced pancreatic cancer (SCALOP): a multicentre, randomised, phase 2 trial. *Lancet Oncol.*, 14(4):317–26, 2013.

[59] B. Chauffert, F. Mornex, F. Bonnetain, P. Rougier, C. Mariette, O. Bouché, J. F. Bosset, T. Aparicio, L. Mineur, A. Azzedine, P. Hammel, J. Butel, N. Stremsdoerfer, P. Maingon, and L. Bedenne. Phase III trial comparing intensive induction chemoradiotherapy (60 Gy, infusional 5-FU and intermittent cisplatin) followed by maintenance gemcitabine with gemcitabine alone for locally advanced unresectable pancreatic cancer. Definitive results of the 2. *Ann. Oncol.*, 19(9):1592–9, 2008.

[60] C. G. Willett, C. F. Del Castillo, H. A. Shih, S. Goldberg, P. Biggs, J. W. Clark, G. Lauwers, D. P. Ryan, A. X. Zhu, and A. L. Warshaw. Long-term results of intraoperative electron beam irradiation (IOERT) for patients with unresectable pancreatic cancer. *Ann. Surg.*, 241(2):295–9, 2005.

[61] J. D. Murphy, C. Christman-Skieller, J. Kim, S. Dieterich, D. T. Chang, and A. C. Koong. A Dosimetric Model of Duodenal Toxicity After Stereotactic Body Radiotherapy for Pancreatic Cancer. *Int. J. Radiat. Oncol. Biol. Phys.*, 78(5):1420–1426, 2010.

[62] T. B. Brunner, U. Nestle, A.-L. Grosu, and M. Partridge. SBRT in pancreatic cancer: what is the therapeutic window? *Radiother. Oncol.*, 114(1):109–16, 2015.

[63] A. Vilanova Bartroli, R. Wegenkittl, A. Konig, and E. Groller. Nonlinear virtual colon unfolding. In *Proceedings Visualization, 2001. VIS '01.*, pages 411–579. IEEE, 2001.

[64] G. Wang, E. G. McFarland, B. P. Brown, and M. W. Vannier. GI tract unraveling with curved cross sections. *IEEE transactions on medical imaging*, 17(2):318–22, apr 1998.

[65] S. K. Jabbour, S. A. Hashem, W. Bosch, T. K. Kim, S. E. Finkelstein, B. M. Anderson, E. Ben-Josef, C. H. Crane, K. A. Goodman, M. G. Haddock, and et al. Upper abdominal normal organ contouring guidelines and atlas: A radiation therapy oncology group consensus. *Practical Radiation Oncology*, 4(2):8289, 2014.

[66] J. O. Deasy, A. I. Blanco, and V. H. Clark. CERR: a computational environment for radiotherapy research. *Med. Phys,*, 30(5):979–85, may 2003.

[67] H. Edelsbrunner and E. P. Mücke. Three-dimensional alpha shapes. *ACM Trans. Graph.*, 13(1):4372, 1994.

[68] J. D. Hobby. Smooth, easy to compute interpolating splines. *Discrete Comput. Geom.*, 1(1):123–140, 1986.

[69] J. Ulén, P. Strandmark, and F. Kahl. Shortest Paths with Higher-Order Regularization. *IEEE Transactions on Pattern Analysis and Machine Intelligence*, 37(12):2588–2600, 2015.

[70] D. A. Low, W. B. Harms, S. Mutic, and J. A. Purdy. A technique for the quantitative evaluation of dose distributions. *Med. Phys.*, 25(5):656, 1998.

[71] H. Yoon, D. Oh, H. Park, S. Kang, Y. Han, D. Lim, and S. Paik. Predictive factors for gastroduodenal toxicity based on endoscopy following radiotherapy in patients with hepatocellular carcinoma. *Strahlentherapie und Onkol.*, 189(7):541–546, 2013.

[72] M. Shinoto, Y. Shioyama, A. Matsunobu, K. Okamoto, H. Suefuji, S. Toyama, H. Honda, and S. Kudo. Dosimetric analysis of upper gastrointestinal ulcer after carbon-ion radiotherapy for pancreatic cancer. *Radiother. Oncol.*, 120(1):140–144, 2016.

[73] H. Kim, D. H. Lim, S. W. Paik, B. C. Yoo, K. G. Koh, J. H. Lee, M. S. Choi, W. Park, H. C. Park, S. J. Huh, D. H. Choi, and Y. C. Ahn. Predictive factors of gastroduodenal toxicity in cirrhotic patients after three-dimensional conformal radiotherapy for hepatocellular carcinoma. *Radiother. Oncol.*, 93(2):302–306, 2009.

[74] X. Liu, G. Ren, T. Xia, Y. Di, and D. Chang. Dosimetric Predictors for Gastrointestinal Toxicity in Pancreatic Cancer After Hypofractionated Radiation Therapy. *Int. J. Radiat. Oncol. Biol. Phys.*, 93(3):E149, 2015.

[75] P. Baumann, J. Nyman, M. Hoyer, B. Wennberg, G. Gagliardi, I. Lax, N. Drugge, L. Ekberg, S. Friesland, K.-A. Johansson, J.-A. Lund, E. Morhed, K. Nilsson, N. Levin, M. Paludan, C. Sederholm, A. Traberg, L. Wittgren, and R. Lewensohn. Outcome in a Prospective Phase II Trial of Medically Inoperable Stage I Non?Small-Cell Lung Cancer Patients Treated With Stereotactic Body Radiotherapy. *J. Clin. Oncol.*, 27(20):3290–3296, 2009.

[76] R. Timmerman, R. Paulus, J. Galvin, J. Michalski, W. Straube, J. Bradley, A. Fakiris, A. Bezjak, G. Videtic, D. Johnstone, J. Fowler, E. Gore, and H. Choy. Stereotactic body radiation therapy for inoperable early stage lung cancer. *JAMA*, 303(11):1070–6, 2010.

[77] R. Timmerman, R. McGarry, C. Yiannoutsos, L. Papiez, K. Tudor, J. DeLuca, M. Ewing, R. Abdulrahman, C. DesRosiers, M. Williams, and J. Fletcher. Excessive Toxicity When Treating Central Tumors in a Phase II Study of Stereotactic Body Radiation Therapy for Medically Inoperable Early-Stage Lung Cancer. *J. Clin. Oncol.*, 24(30):4833–4839, 2006.

[78] J. M. Haseltine, A. Rimner, D. Y. Gelblum, A. Modh, K. E. Rosenzweig, A. Jackson, E. D. Yorke, and A. J. Wu. Fatal complications after stereotactic body radiation therapy for central lung tumors abutting the proximal bronchial tree HHS Public Access. *Pr. Radiat Oncol*, 6(2):27–33, 2016.

[79] M. N. Corradetti, A. R. Haas, and R. Rengan. Central-Airway Necrosis after Stereotactic Body-Radiation Therapy. *N. Engl. J. Med.*, 366(24):2327–2329, 2012.

[80] J. Y. Chang, Q.-Q. Li, Q.-Y. Xu, P. K. Allen, N. Rebueno, D. R. Gomez, P. Balter, R. Komaki, R. Mehran, S. G. Swisher, and J. A. Roth. Stereotactic ablative radiation therapy for centrally located early stage or isolated parenchymal recurrences of non-small cell lung cancer: how to fly in a "no fly zone". *Int. J. Radiat. Oncol. Biol. Phys.*, 88(5):1120–8, 2014.

[81] S. Adebahr, S. Collette, E. Shash, M. Lambrecht, C. Le Pechoux, C. Faivre-Finn, D. De Ruysscher, H. Peulen, J. Belderbos, R. Dziadziuszko, C. Fink, M. Guckenberger, C. Hurkmans, and U. Nestle. LungTech, an EORTC Phase II trial of stereotactic body radiotherapy for centrally located lung tumours: a clinical perspective. *Br. J. Radiol.*, 88(1051):20150036, 2015.

[82] J. D. Cox, J. Stetz, and T. F. Pajak. Toxicity criteria of the radiation therapy oncology group (rtog) and the european organization for research and treatment of cancer (eortc). *Int. J. Radiat. Oncol. Biol. Phys.*, 31(5):13411346, 1995.

[83] K. J. Lee, H. I. Yoon, J. Chung, J. Y. Park, S. Bang, S.-W. Park, J. S. Seong, and S. Y. Song. A Comparison of Gastrointestinal Toxicities between Intensity-Modulated Radiotherapy and Three-Dimensional Conformal Radiotherapy for Pancreatic Cancer. *Gut Liver*, 10(2):303–309, 2016.

[84] C. Chen, M. Witte, W. Heemsbergen, and M. Herk. Multiple comparisons permutation test for image based data mining in radiotherapy. *Radiat. Oncol.*, 8(1):293, 2013.

[85] M. P. Dubuisson and A. K. Jain. A modified hausdorff distance for object matching. In *Proceedings of 12th International Conference on Pattern Recognition*, volume 1, pages 566–568, 1994.

[86] A. K. Shadad, F. J. Sullivan, J. D. Martin, and L. J. Egan. Gastrointestinal radiation injury: Symptoms, risk factors and mechanisms. *World Journal of Gastroenterology*, 19(2):185, 2013.

[87] V. Verma, A. J. Lazenby, D. Zheng, A. R. Bhirud, Q. P. Ly, C. Are, A. R. Sasson, and C. Lin. Dosimetric parameters correlate with duodenal histopathologic damage after stereotactic body radiotherapy for pancreatic cancer: Secondary analysis of a prospective clinical trial. *Radiother. Oncol.*, 122(3):464469, 2017.